From Venus to Mars: Spectroscopy and Kinetics of Reactive Intermediates in Planetary Atmospheres

Thesis by
Gregory H. Jones

In Partial Fulfillment of the Requirements for the
Degree of
Doctor of Philosophy

CALIFORNIA INSTITUTE OF TECHNOLOGY
Pasadena, California

2024
Defended September 19th, 2023

Gregory H. Jones
ORCID: 0000-0003-3275-1661

ACKNOWLEDGEMENTS

Of all the sections of my thesis, this is the section over which I've agonized most; how could I find the right words to properly express my gratitude to those who have supported me? I write this as the final section just before submission, forced to settle for merely the words I have.

I thank my advisor, Mitchio Okumura, for his invaluable guidance over these years of my Ph.D. Mitchio has not only taught me the techniques of spectroscopy and kinetics, but expertly demonstrated there exists no conflict between unyielding scientific rigor and a compassionate, joyful approach doing science with others. I'm also deeply appreciative of the freedom he gave me to pursue independent projects and his continued support even as my research methods evolved away from experiment toward theory.

In my undergraduate years, I was lucky to have Justin Chalker and later Erin Iski as research mentors. Both got me excited about research (albeit in sharply contrasting subfields), and encouraged me in my application to graduate school.

I thank those who mentored me as I first started in the program, especially Jeff Mendez. Jeff was a great friend and mentor, helping me not only develop as a teacher in Ch3a but also guiding me through the rocky process of advisor selection. After joining Mitchio's group, Matt Smarte, Joseph Messinger, and Elizabeth Lunny showed me how to navigate graduate school. I'm particularly indebted to Matt, who through several ALS experiments helped me develop a keen eye for subtle errors in data analysis and taught me the ingredients for a well-designed experiment. All encouraged me to follow my passion for quantum chemistry; without this change in direction, I doubt I would have had the drive to finish.

I thank two friends and labmates who have been with me throughout the entire process, Doug Ober and Hannah Szentkuti. I treasure the years we have had together. In addition to Hannah and Doug, I'm grateful for all the members of the Okumura group that I've had the privilege to know over my time here. The joy of being a theorist in an experimental group is that I've had the opportunity to work with every member of our group on some project or another, even if only briefly. In the last year or two, I'd really like to highlight our postdoc Charlie Markus, who was always happy to lend an ear or offer advice, and Megan Woods, who has been an invaluable friend helping me navigate the end of my Ph.D.

My Ph.D. has been one of collaborations, and I thank Wen Chao, a graduate student from our group, as well as Fred Winiberg and Carl Percival at JPL for their work on the ClSO projects. I've also enjoyed working with Danica Adams and Yuk Yung here at Caltech on the Mars project.

Outside of research, I thank my friends from choir, Manuel Núñez, Matthew Graham, and Don Thomas. Our regular Thursday night get-togethers after choir served as more than a welcome break from lab; they refreshed my soul.

Closer to home, I thank Makenna Herl for being a constant friend and support throughout my Ph.D. Words cannot express how grateful I am for your friendship, and I don't know how I could have done this without you.

Finally, I thank my family: my parents, Kent and Holly Jones, my grandparents, Ron and Jane Harrison, and my sister, Bethany Vargas. I love you deeply and will always appreciate your love and support.

ABSTRACT

The spectroscopy and kinetics of reactive intermediates in the atmospheres of Venus, Earth, and Mars were investigated through a combination of experimental and theoretical methods. Vibrational progressions in the A- and B-bands of ClSO were assigned, and predicted spectra matched well with experiment. A new unimolecular mechanism for 3-hydroxy-substituted Criegee intermediates was proposed, and predicted to be competitive with known isomerization pathways. The kinetic isotope effect and temperature dependence of the H + HO_2 reaction was calculated using high-level *ab initio* methods, with implications for the understanding of water loss on Mars.

PUBLISHED CONTENT AND CONTRIBUTIONS

Chao, W.; Jones, G. H.; Okumura, M.; Percival, C. J.; Winiberg, F. A. F. A-Band Spectrum of the ClSO Radical: Electronic Structure of the Sulfinyl Group. *The Journal of Physical Chemistry A*. **2023**, *127* (40), 8374-8382. DOI: https://doi.org/10.1021/acs.jpca.3c04977.

G.H.J. did all CASPT2 calculations, advised W.C. on (EOM-)CCSD calculations, determined theoretical cross sections, performed all analysis and interpretation with respect to the conical intersection, and participated in the writing of the manuscript.

Chao, W.; Jones, G. H.; Okumura, M.; Percival, C. J.; Winiberg, F. A. F. Spectroscopic and Kinetic Studies of the ClSO Radical from Cl_2SO Photolysis. *Journal of the American Chemical Society* **2022**, *144* (44), 20323–20331. DOI: 10.1021/jacs.2c07912.

G.H.J. performed all theoretical calculations and participated in the writing of the manuscript.

TABLE OF CONTENTS

Acknowledgements . . . iii
Abstract . . . v
Published Content and Contributions . . . vi
Table of Contents . . . vi
List of Illustrations . . . ix
List of Tables . . . xiii
Chapter I: Introduction . . . 1
Chapter II: Spectroscopic and Kinetic Studies of the ClSO Radical from Cl_2SO Photolysis . . . 3
2.1 Abstract . . . 4
2.2 Introduction . . . 4
2.3 Experimental Methods . . . 7
2.4 Theoretical Methods . . . 9
2.5 Results and Discussion . . . 10
2.6 Conclusions . . . 20
2.7 Acknowledgement . . . 21
2.8 Associated Content . . . 21
Bibliography . . . 22
Chapter III: A-Band Spectrum of the ClSO Radical: Electronic Structure of the Sulfinyl Group . . . 28
3.1 Abstract . . . 29
3.2 Introduction . . . 29
3.3 Experimental Methods . . . 30
3.4 Theoretical Methods . . . 31
3.5 Results . . . 33
3.6 Discussion . . . 39
3.7 Conclusions . . . 43
3.8 Associated Content . . . 44
3.9 Acknowledgement . . . 44
Bibliography . . . 46
Chapter IV: Novel Decomposition Mechanism for Substituted Criegee Intermediates via Multistructural Semiclassical Transition State Theory . . . 51
4.1 Introduction . . . 52
4.2 Theory . . . 53
4.3 Results . . . 55
4.4 Conclusions . . . 60
4.5 Supporting Information . . . 61
Bibliography . . . 77

Chapter V: Ab initio calculations of the H + HO_2 Reaction and its Kinetic Isotope Effect: Impact on Water Loss from Mars 81
5.1 Introduction 82
5.2 Theoretical Methods 84
5.3 Results 85
Bibliography 91
Chapter VI: Photoelectron-Photoion Coincidence Spectroscopy of the ClO Radical 95
6.1 Introduction 96
6.2 Experimental 97
6.3 Results 99
Bibliography 103

LIST OF ILLUSTRATIONS

Number *Page*

2.1 Representative transient absorption spectra of the Cl_2SO/N_2 photolysis system at different delay times (gate width = 70.5 μs) recorded (A) without scavengers, (B) with I_2 and (C) with NO_2 for Exp# I-1, I-2, and N-5 (Tables S1 and S2), respectively. The photolysis laser sets time zero. The negative gray lines show the estimated initial Cl_2SO depletion. 11

2.2 (A) Representative absorption temporal profiles near 303 nm of the Cl_2SO/N_2 photolysis system at different pressures for Exp# 1, 4 and 9 (Table S3). (B) The reciprocal of (A). The gray lines show a linear fit to 0.5-20 ms region only to lessen the impact from potential secondary reactions on the determination of the rate coefficient but good linearity was observed out to 40 ms. The gray lines in (A) are the reciprocal of linear fit in (B). 12

2.3 The black line is the average of all the ClSO spectra shown in gray (Table S3). The dotted line shows the cross-section of Cl_2SO for comparison. The stick diagram downward shows the calculated vibrational progression for the $1^2A"$ excited state. The red and blue bars are the SO stretching series with 0 and 1 quanta excitation of the bending mode and black line profile present the simulated spectrum (FWHM = 3 nm) of these two series (Table S6). Inset: liner fit to the observed peak centers. 13

2.4 The calculated oscillator strength, vertical excitation energies (in eV) and the natural density difference orbitals (top view) for the $1^2A'$, $2^2A'$ and $1^2A"$ excited states calculated at EOMEE-CCSD/ano-pVQZ level and the ground state geometry. 15

2.5 The observed rate coefficient as a function of the total pressure (assuming σ_{ClSO}(303 nm) = 1.0×10^{-18} cm^2 and L = 431.8 cm). The red line shows the fit to all the experimental data on the figure using proposed mechanism in Scheme 1. Black error bars present 2σ of the blue circles distribution. The circle (Exp #1-9 and 23-48) and square (Exp #10-22, Rep. Rate = 1 or 2 Hz, Table S3) symbol presents measurements with distinct gas refresh rates. 20

3.1 (Upper Panel) The recorded spectrum of the Cl_2SO/N_2/248 nm system at 100 μs after pulsed laser (exposure time = 117.5 μs, averaged for 12288 shots) at 40 Torr and 292 K. Cyan, blue, and red lines represent spectra at different grating angles (center wavelengths of 370 nm, 420 nm, and 520 nm), while the gray lines show the background noise without Cl_2SO. The black simulated spectra downward is the sum of contributions from both the 1^2A' (orange) and 2^2A' (olive, stick spectra convoluted with a Gaussian function with FWHM = 100 cm^{-1}) states. The comparison between experimental and theoretical absolute cross sections is shown in Figure S5. (Lower Panel) Linear and quadratic fits to the observed positions of the vibrational peaks, within the marked region. 35

3.2 A closer look at the structure of the weak absorption band in the 360-480 nm range. A few doublet peaks were observed, yielding an average spacing of 76 cm^{-1}. The stick spectrum displays the intensities predicted for excitation to the 2^2A' state, incorporating Franck-Condon factors and thermal population effects at 0 K. The energy of the computed transition origin has been shifted to the red by 870 cm^{-1} for alignment with the vibronic progression of experimental spectrum (green dotted lines), while the red dashed lines indicate predicted doublets. Inset is a magnification of the spectrum between 415 and 445 nm. 37

3.3 The adiabatic potential energy surface of the ground state and two excited ^{2}A' states of the ClSO radical in the 2D branching space (x, y; see Figure 3.4) computed at the XDW-CASPT2(7,5)-3SA level near the MECI geometry (x = 0, y = 0). The meshed line shows the profile of the ground state vibrational wavefunction. The black arrow shows the vertical transition from the MECI to the ground state PES (which is flattened for clarity; the color bar to the right gives the energy scale of the ground state PES contours). 39
3.4 The corresponding vibrational motions of the seam space (the set of geometries where the 1^2A' and 2^2A' states are degenerate) and the branching space (the complement of seam space) near the MECI geometry. 40
3.5 Schematic MO diagram showing the active space orbitals of the ClSO radical (top view) used in the XDW-CASPT2 calculation. Vertical and horizontal arrows indicate transitions to excited states for alpha and beta electrons. The green lines connect orbitals with the out-of-plane orientation. 42

4.1 Traditional decomposition pathway for *syn*-Criegee intermediates. . . 52
4.2 Conformer-specific contributions to the MS-SCTST CRP. 57
4.3 Microcanonical rates for MS-SCTST and other approximations. . . . 58
4.4 OH channel branching fraction as a function of energy. 59
4.5 MS-SCTST rates for thermal decomposition of *syn*-3-hydroxypropanal oxide. 60
4.6 Assignment of MS-T(C) states to energy bins for the scaling of tunneling functions. 62
4.7 Microcanonical decomposition rates of *syn*-3-hydroxypropanal oxide from 8000 cm^{-1} to 25000 cm^{-1}. 72
4.8 Thermal decomposition rates of *syn*-3-hydroxypropanal oxide from 200K to 1000K. 73

5.1 Chemical mechanism for water loss from Mars. 82

5.2 Isotope specific rates as a function of temperature for the H + HO_2 reaction on the triplet surface. (Top) The rate for the unsubstituted reaction on the triplet surface is plotted as black solid line, while the rates for the atomically substituted and molecularly substituted reactions are plotted as red and blue solid lines, respectively. The temperature-independent JPL recommendation is shown as the dashed black line for reference. (Bottom) Kinetic isotope effect for the atomically substituted (red) and molecularly substituted (blue) reactions. The purple dashed line shows the constant $\sqrt{2}$ KIE used in many previous models. 86
5.3 Potential energy diagram for various isotopologues of H + HO_2. Differences in the zero of energy for reactants stem from differences in zero-point vibrational energy and the diagonal Born-Oppenheimer correction. 87
5.4 Potential energy diagram showing stationary points on the singlet surface in the H + HO_2 reaction. 87
5.5 Isotope specific rates as a function of temperature for the H + HO_2 reaction on the singlet surface. 88
5.6 Initial results from the new rates of this work. The ratio of new model concentration divided by old model concentration is given on the x axis, and the altitude is given on the y axis. An ~30% increase in atomic D is observed at the top of the atmosphere. 90

6.1 Diagram of the radical source. 97
6.2 Ratio of signal differences as a function of injector distance 99
6.3 Absolute photoionization cross section of ClO measured at SOLEIL. (*Blue*) Cross section of ClO. (*Red*) Cross section of O_3. Grey shading for both lines indicates random error from ion counting. The spectrum was scaled to the absolute cross section measurement at 13.0 eV (*blue point*) with a value of 6.7 ± 2.0 Mb. 100
6.4 Comparison to previous data measured at ALS. (*Blue, solid*) The cross section measured at SOLEIL, scaled by a factor of 8. (*Green, dotted*) The cross section measured at the ALS. 101
6.5 Slow photoelectron spectrum of ClO. 102

LIST OF TABLES

Number *Page*

2.1 The (EOM-)CCSD and CCSDT calculation of ClSO for geometries, energies relative to the optimized ground state ΔE, harmonic vibrational frequencies, and the 1^2A"$\leftarrow$X^{2}A" transition energies. 17

3.1 Summary of the calculations of ClSO for Geometries, Harmonic Frequencies, Adiabatic Transition Energies ΔE Relative to the Ground State, and the 0-0 Transition Energies. 34
3.2 Summary the geometries and energy difference relative to the ground state, ΔE, calculated at the XDW-CASPT2(7,5) level. 38
3.3 Summary of the UV-Vis absorption band positions of distinct sulfinyl radicals (RSO). 43

4.1 Lowest energy conformers and associated barriers. 56
4.2 Conformer B2PLYP-D3(BJ) electronic energies relative to the lowest energy conformer (kcal/mol). 56
4.3 Thermal decomposition rates of *syn*-3-hydroxypropanal oxide from 200K to 1000K. 73

5.1 Fit of theoretical rates to Equation 5.1. 89

Chapter 1

INTRODUCTION

The heart of chemistry is the study of reactions, the cleavage and formation of chemical bonds. We understand reactions through a number of different models. Perhaps the first such model one encounters in an undergraduate study of chemistry is the so-called "8 electron rule" coupled with Lewis structures to describe possible reactants and products. While not predictive, this gives the budding chemist some tools to evaluate reasonable and unreasonable chemical species. Later refinement might come in a course of organic chemistry with the introduction of some indeterminate hybrid of valence bond and molecular orbital theory, augmented by "arrow-pushing" mechanisms to describe the flow of electrons from one bonding arrangement to another. Many phenomenological models of reactivity are built on such a framework, such as group additivity rules or the standard textbook description of substitution and elimination reactions in solution; however, key to validating and challenging these models is direct observation of reactive intermediates.

An essential tool in probing reactive intermediates is provided by spectroscopy. Not only do spectroscopic methods allow for unique identification of molecular species, application in time-resolved experiments allow for the determination of kinetic parameters needed to model the long term time evolution of a chemical system. This is being done with great success for the chemical reactions controlling Earth's atmospheric composition, as evidenced by the JPL Kinetic Data Evaluation and atmospheric chemical models based on such experimental observations; however, this previous work explores only a narrow range of chemical space, naturally favoring conditions actually present on Earth. Even restricted to the two planets nearest earth, temperatures may range from 120 K on the poles of Mars to 750 K on the surface of Venus. Furthermore, where a reaction may be negligible in Earth's atmosphere due to minimal reactant abundance, it may be pivotal in describing the evolution of a different planetary atmosphere.

While direct measurements of reactive intermediates under conditions relevant to a given planetary atmosphere is the ideal, such conditions are not always readily accessible. Furthermore, even with direct spectroscopic detection, secondary chemistry can confound interpretation of results. In these cases, we can leverage

the tools of quantum chemistry to predict and explain the observations, providing a model to understand the underlying chemistry. This work presents the results of the application of both experimental observation and theoretical prediction to explore important reactive intermediates in the atmospheres of Venus, Earth, and Mars. We present predictions and interpretations of experimental spectra for the ClSO radical on Venus, a new reaction mechanism for Criegee intermediates in Earth's atmosphere, and isotope effects in the loss of water from Mars. The author hopes that this contribution will aid in the further understanding of the evolution of these planetary atmospheres and those beyond our solar system.

Chapter 2

SPECTROSCOPIC AND KINETIC STUDIES OF THE CLSO RADICAL FROM CL_2SO PHOTOLYSIS

Reprinted (adapted) with permission from Chao, W.; Jones, G. H.; Okumura, M.; Percival, C. J.; Winiberg, F. A. F. Spectroscopic and Kinetic Studies of the ClSO Radical from Cl_2SO Photolysis. *Journal of the American Chemical Society* **2022**, *144* (44), 20323–20331. DOI: 10.1021/jacs.2c07912.

2.1 Abstract

Thionyl chloride (Cl_2SO) serves as a common Cl atom source in widespread applications of chlorine chemistry though little is known about the reactivity and spectroscopy of the ClSO radical after a Cl–S bond cleavage. We performed a pulsed laser photolysis experiment to detect ClSO from Cl_2SO photolysis at 248 nm in a gas flow reactor by a time-resolved UV-Vis transient absorption spectroscopy. A few chemical tests, using I_2 and NO_2, suggested the structured absorption band between 260–320 nm belonged to ClSO radical and the termolecular ClSO+Cl+M $\rightarrow$ Cl_2SO association reaction occurred. From EOMIP-CCSD/ano-pVQZ calculations, the ClSO band was assigned to the $1^2A'' \leftarrow X^2A''$ transition involving the $\pi^* \leftarrow \pi$ transition of the SO bond and the vibrational progression to the SO stretching mode of the $1^2A''$ state, with a maximum cross-section = (2.0±0.5)×10^{-18} cm^2 near 286 nm (1σ uncertainty) and an average spacing of vibrational structure of 658 cm^{-1}. The rapid decay of the ClSO signal monitored near 303 nm could be fit to a second-order kinetic model over 10-90 Torr, which yields an effective bimolecular rate coefficient $k_{Cl+ClSO} = (1.48 \pm 0.42) \times 10^{-11}$ cm^3 $molecule^{-1}$ s^{-1} at 292 K and 90 Torr (1σ uncertainty). This fast recombination reaction suggests that Cl-containing SO_x species might act as significant Cl atom reservoirs in sulfur oxide rich environments such as Venus' atmosphere. Moreover, the reported UV spectrum provides a new means for monitoring the ClSO radicals.

2.2 Introduction

Chlorine chemistry plays an important role in both the natural environment and our daily life.[1] Thionyl chloride (Cl_2SO) is not only a common chlorine source but also has direct chemical applications in battery science and organic synthesis. The lithium-thionyl chloride battery worked as a model battery in many applications[2,3] due to its high energy density despite the lack of rechargeability.[2] In organic chemistry, Cl_2SO is used as a standard reagent in converting –OH functional groups into –Cl; however, the exact mechanism is not yet known.[4] Reactive chlorine, in Earth's stratosphere, is most famous for the catalyzed destruction of ozone, which ultimately led to the ozone hole.[5] In Venus' mesosphere, Cl atoms have been proposed to catalyze the conversion of CO into CO^2 to remove oxygen[6] though Cl concentration could be strongly affected by the reactions with sulfur oxide to form Cl_2SO_2 as the ultimate reservoir.[7]

In the laboratory, Cl atoms are widely used to initiate oxidation reactions in atmospheric and combustion chemistry studies.[8] Molecular chlorine (Cl_2) and oxalyl

chloride ($(ClCO)_2$) are common photolytic precursors due to their low reactivity photolysis co-products[9] and Cl atom quantum yields of ~2.[10] The small photolysis cross-sections of Cl_2 and $(ClCO)_2$ (<3×10^{-19} cm^2 at 248 nm)[10,11] would typically lead to 1-2% of precursor depletion being photolyzed, which makes generating high Cl concentrations difficult without high precursor concentrations. However, high precursor concentrations can lead to experimental difficulties; for example, they can induce large background signals that hinder spectroscopic measurements.[12] In contrast, Cl_2SO has a large cross-section (>7×10^{-18} cm^2) below 250 nm,[13] thus making it a high-yield photolytic source of Cl atoms for kinetic studies.[14–17]

The photolysis of Cl_2SO was studied by monitoring the spectroscopic and kinetic properties of sulfur monoxide (SO).[18] Previous studies in a collision-free environment[19,20] have suggested three photodissociation channels, including (1) a three-body dissociation channel, (2) a radical channel and (3) a molecular channel, as shown below:

$$Cl_2SO \rightarrow 2Cl + SO, \quad (1)$$
$$D_0 = 108.5 \pm 0.3 \text{ kcal mol}^{-1} (263.7 \text{ nm})$$
$$Cl_2SO \rightarrow Cl + ClSO, \quad (2)$$
$$D_0 = 57.3 \pm 0.3 \text{ kcal mol}^{-1} (499.2 \text{ nm})$$
$$Cl_2SO \rightarrow Cl_2 + SO, \quad (3)$$
$$D_0 = 51.3 \pm 0.3 \text{ kcal mol}^{-1} (557.6 \text{ nm})$$

where the dissociation energies were calculated by Baum *et al.* using the JANAF Thermochemical Tables.[20] Although all three channels are energetically feasible after absorbing a photon below 250 nm, the dissociation dynamics depend strongly on the photolysis wavelength.[19–25]

At 193 nm, Cl_2SO is mainly excited through the $\sigma^*_{ClS} \leftarrow n_{Cl}$ transition[22] leading to a direct dissociation of two Cl atoms on a time scale faster than rotational motion[23] with the three-body channel (1, ~83%) dominating the radical (2, ~17%) and the molecular (3, <3%) channels.[20] At 235 nm, both $\sigma^*_{ClS} \leftarrow n_{Cl}$ and $\sigma^*_{ClS} \leftarrow n_S$ transitions are excited;[22] the three-body (1) and radical (2) channels yield both ground state $Cl(^2P_{3/2})$ and hot $Cl^*(^2P_{1/2})$ atom and a relative yield of $Cl^* = 0.35\pm0.06$ was reported.[22]

At 248 nm, calculations indicate that a mixture of $\sigma^*_{ClS} \leftarrow n_S$ and $\pi^*_{SO} \leftarrow n_S$ transitions are excited.[22] Previous theoretical work has predicted that the excited state, $\pi^*_{SO} \leftarrow n_S$ transition, is not repulsive[23] and thus, that the radical dissociation pathway (2) dominates the main product channel (~96.8%) while the molecular channel (3) only contributes slightly (~3.2%).[20,21] No evidence of the three-body channel has been reported at 248 nm.[20,21] However, the laser-induced fluorescence spectrum of SO was observed; the SO yield of (13±7)% under 1 Torr He,[21] was contributed to the unimolecular decomposition of the hot ClSO radicals.[21] Photofragment translational spectroscopy showed that, after absorbing a photon, on average roughly half of the available energy (~10^4 cm^{-1}) stayed in the ClSO fragments[22] with a wide distribution, such that a small portion exceeded the dissociation threshold of Cl-SO (D_0 = 17900±150 cm^{-1}).[22,26] These calculations were validated by experimental data showing that the yield of SO was reduced at higher pressures.[18] The Cl^* relative yield = 0.52±0.03 at 248 nm was reported,[24] indicating that less than half of the ClSO radicals possess enough internal energy to dissociate.[22]

Although the product branching ratio and dynamics of Cl_2SO photolysis have been studied for decades, the main weak point of Cl_2SO as a Cl atom source is the unknown reactivity of ClSO radicals due to the lack of suitable methods for kinetic measurements. In the condensed phase, the ClSO solid-phase EPR spectrum has been investigated.[27] In the gas phase, the far-IR spectrum has been reported, but no analysis was done.[28] The microwave spectrum was mentioned in the literature without available data.[29] Chu et al.[30] has measured the IR spectrum of the nascent products from Cl_2SO photolysis at 248 nm and the ClSO radicals were identified by matching the simulation of the rotational resolved SO stretching band to experimental observations.[30] Only one kinetic measurement of the ClSO radical has been performed; using mass spectroscopy,[31] Blitz et al. reported a ClSO + NO_2 reaction rate coefficient of (8.0±1.2)×10^{-12} cm^3 $molecule^{-1}$ s^{-1} at 1 Torr He, but no products were found in the mass spectrum.[31]

Transient UV-Vis absorption spectroscopy is well suited for exploring the reactivity of ClSO under a wide range of conditions,[32] e.g., solving the debate of Cl_2SO photolysis behavior in tetrahydrofuran.[33,34] However, the UV-Vis spectrum of the ClSO radical is still unknown. Li performed the QCISD calculation on the lowest excited state of the ClSO radicals and predicted an adiabatic transition energy close to 2.4 eV.[35] This work aimed to obtain the gas phase UV-Vis spectrum of ClSO radicals generated from Cl_2SO photolysis at 248 nm and to explore the kinetics of

its subsequent reactions by performing Pulsed-Laser-Photolysis (PLP) experiments with a time-resolved broad-band UV-Vis transient absorption spectroscopy coupled with a flow reactor.

2.3 Experimental Methods

Chemical Preparation

Schematics of the experimental system are shown in Figures S1 and S2. The ClSO radicals were generated in a glass reactor (L = 50.8 cm, ID = 3.8 cm) with UV anti-reflection fused silica windows (Edmund, 36948), where the inner sides were purged by a small stream of the buffer gas to prevent contamination. The Cl_2SO/buffer mixture flowed into the reactor from the middle and was pumped out at the two ends, resulting in an effective gas length of 43.2 cm (Fig. S2). Mass-flow controllers (MKS, GM50A and 1179A) metered the total flow, ensuring fully gas sample replacement between photolysis laser shots (repetition rate = 4 Hz for all experiments except where stated otherwise). A small stream of buffer gas carried Cl_2SO vapor (Sigma-Aldrich, >99%) out of a bubbler, immersed in a temperature-controlled water bath (Fisherbrand, Isotemp 4100). A glass/Teflon needle valve (Gilmont instruments, GM-7100), controlled the bubbler pressure. A similar bubbler setup introduced iodine into the reactor; however no needle valve was used due to the low vapor pressure of iodine (0.2 Torr at 20 °C).

A gas mixture of 0.66% NO_2 was prepared by premixing NO and O_2 (Matheson, 99.5%, and Airgas, 99.994% respectively) in a 1:12 ratio, balance N_2 (5300 Torr total pressure) in a stainless cylinder and left overnight for fully mixing. The excess O_2 was added to ensure conversion of NO to NO_2.[36] All pressures in the reactor and bubblers were measured with diaphragm gauges (Baratron 127AA-01000A, 122AA-01000CB and MKS 127AA-00100A) A throttle valve (MKS, type 153) controlled the pressure of the reactor. The Cl_2SO concentrations were directly measured in the reactor with the UV spectrometer. Typical concentrations in the reactor were: $[Cl_2SO] = (0.5\text{-}2.4)\times10^{14}$ molecule cm^{-3}, $[I_2] = (0\text{-}7.3)\times10^{14}$ molecule cm^{-3}, $[NO_2] = (0\text{-}1.7\times10^{14}$ molecule cm^{-3} and N_2 (LN_2 evaporation), He (Airgas, 99.999%) or Ar (Matheson, 99.9995%) balanced (10-90 Torr). All the experiments were conducted at 292 K.

Optical setup

The UV light from a Laser Driven Light Source (LDLS, Energetiq, EQ-99) was aligned through a multi-pass UV enhanced White cell (D = 25.4 cm, R = 140 cm,

Acton Optics). After the White cell, the probed beam was focused into a spectrometer (Acton, SpectraPro 300i) with a gated image-intensified CCD array (Princeton Instruments, PI-MAX4, 1024×256) and a photomultiplier tube (PMT, Hamamatsu, R928). After the grating, a rectangular mirror reflected the bottom portion of the probe beam into the PMT, monitoring the absorbance change near the center wavelength (resolution ~1 nm), enabling simultaneous PMT and ICCD light collection. The spectrometer wavelength and resolution (~0.4 nm) were characterized using a mercury pen-ray lamp (Hg-Ar).

The excimer (Coherent, COMPex 205F, KrF) photolysis laser beam was aligned between the two White cell objective mirrors, spaced 15 mm apart, and directed towards the field mirror. A long-pass filter (Semrock, LP02-257RU-30×40) in front of the field mirror discriminated the 248 nm photolysis light from the probed beam path. The photolysis beam was focused horizontally at the gap between the two White cell objective mirrors so that the photolysis beam filled the entire volume of the reactor, maximizing the overlap with the probe beam path. As the photolysis beam was diverging slightly (θ_{div} ~ 6°) across the reactor, the divergence effect was tested by focusing the photolysis beam at distinct positions and monitoring the kinetics of the simplest Criegee intermediate.

Data Acquisition

The experiments were controlled by Labview 2018 and all pressure and flow values were recorded through a DAQ card (NI, cDAQ-9174). The excimer laser and DAQ cycle were synchronized by two delay generators (Stanford research DG535 and BNC Model 565), with the DG535 used as the primary controller, while ICCD was stepped controlled (Gate Width = 47, 70.5, 94, or 164.5 μs) via the program. The PMT output passed through a homemade transimpedance amplifier and was collected with a DAQ card (Gage, CS144002U, Sampling Rate = 200 kS s^{-1}). Typically, spectra were averaged over 256, 384 or 512 laser shots for a given delay time, while the PMT profile was averaged over all laser shots throughout the whole experiment. A small absorption background (<0.3% at 303 nm depending on laser fluence) was observed after time zero (Excimer laser on). This background was observed with the reactor removed from the beam path and could be discriminated by mis-aligning the photolysis and probe beams, however this would have caused the photolysis beam to not pass through the reactor cleanly. As such, the background was suspected to be caused by the photolysis and probe beam overlap at the long-pass filter. The photolysis laser power (Coherent, J-50MUV-248) was measured either

at the reactor's exit or after the long-pass filter. All the presented data here were background subtracted.

2.4 Theoretical Methods

ClSO is an open-shell molecule with 22 core electrons and 19 valence electrons, which permits the use of coupled cluster methods for highly accurate determinations of structural and energetic parameters. All quantum chemical calculations were performed using the CFOUR program suite,[37] with the exception of unrestricted LR-CCSDT[38] calculations (equivalent to EOMEE-CCSDT for energies),[39] which were performed using the MRCC package.[40] Atomic natural orbital (ANO) type basis sets have been shown to perform well for the prediction of harmonic frequencies,[41] prompting the use of the ano-pVXZ series of basis sets by Neese et al.,[42] which are one of the few non-relativistic ANO-type basis sets which cover the third period. As these basis sets are not optimized for the calculation of core correlation, computational cost was greatly reduced by invocation of the frozen-core approximation. Geometries and energies were calculated using two distinct references, as detailed below.

Unrestricted Reference

The ground state was optimized using CCSD/ano-pVQZ on an unrestricted Hartree-Fock (UHF) reference, while the 1^2A" excited state was optimized using EOMEE-CCSD/ano-pVQZ, also on a UHF reference. Vibrational frequencies were calculated at each geometry by finite difference of analytic gradients.[43–46] Excitation energies and oscillator strengths for the 1^2A", 1^2A', and 2^2A' states were calculated at both geometries. Energies of the X and 1^2A" states were refined by a term loosely analogous to the ΔE_{HLC} term of the HEAT method,[47–49] using the difference between LR-CCSDT[38] and EOMEE-CCSD energies in a smaller basis (ano-pVDZ) to correct for the effect of connected triple excitations.

Restricted Reference

Both the ground state and 1^2A" excited state were optimized with the EOMIP-CCSD/ano-pVQZ method using the $ClSO^-$ anion as a closed-shell reference. Use of this reference allowed both states to be treated on equal footing at the same level of excitation. Frequencies for both states were calculated at the same level of theory by finite difference of analytic gradients.[50] Energies of the minima were refined by EOMIP-CCSDT/ano-pVQZ calculations, where the use of the large basis was made

affordable by the use of the restricted Hartree-Fock (RHF) reference.

Spectral Simulation

A displaced harmonic oscillator stick spectrum, including overtone and combination bands as well as corrections for temperature, was simulated using the ezSpectrum package. Parameters for the simulation were taken from the restricted reference calculations.

2.5 Results and Discussion

Figure 2.1A shows the difference absorption spectra of the Cl_2SO/N_2 photolysis system. Negative absorption below 280 nm was observed and attributed to the Cl_2SO depletion. A structured absorption features was observed below 320 nm; the temporal profiles (Figure 2.2) near 303 nm showed an instantaneous ($< 5\mu$s) formation following Cl_2SO photolysis, indicating the structured absorption was due to the primary photolysis products. As shown in Figure 2.1, the 303 nm wavelength was chosen for kinetic traces of the structured absorption to avoid interference from the Cl_2SO depletion.

Interestingly, the Cl_2SO depletion was observed to disappear after time zero (Figure 2.1A), on a timescale which was faster than the gas residence time (Figure S7-S8). We observed an isosbestic point near 275 nm (Figure S21), suggesting that Cl_2SO reformed through a chemical reaction from the origin of the structured spectrum (Figure S26-S27). Literature has shown that the primarily photolysis product channel of Cl_2SO at 248 nm is the radical channel (2), with the Cl atom and ClSO radical quantum yields close to unity.[20,21]

We proposed that the origin of the structured absorption spectrum is the ClSO radical and that recombination between the Cl atom and ClSO radical regenerates Cl_2SO, giving rise to the observed decay of ClSO and regeneration of Cl_2SO.

To test this hypothesis, first, we added iodine (I_2) as a Cl atom scavenger (k_{I2+Cl} = 2.5×10^{-10} cm^3 $molecule^{-1}$ s^{-1}).[51] Figure 2.1B shows that the lifetime of Cl_2SO depletion and the structured absorption was extended in the presence of I_2, i.e. in the absence of the Cl atoms. Second, we added NO_2 as a ClSO scavenger.[31] In the presence of NO_2 (Figure 2.1C), the structured absorption disappeared within 5 ms, while the Cl_2SO depletion survived. The negative absorption near 360 nm was attributed to NO_2 depletion through reaction with the origin of the structured spectrum. The same effect was observed by varying [I_2] (Figure S7-S9 and S18),

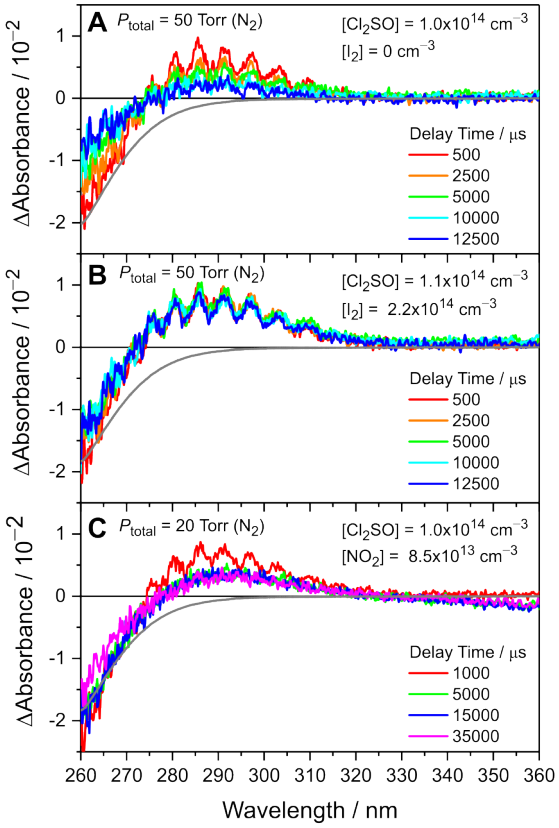

Figure 2.1: Representative transient absorption spectra of the Cl_2SO/N_2 photolysis system at different delay times (gate width = 70.5 μs) recorded (A) without scavengers, (B) with I_2 and (C) with NO_2 for Exp# I-1, I-2, and N-5 (Tables S1 and S2), respectively. The photolysis laser sets time zero. The negative gray lines show the estimated initial Cl_2SO depletion.

[NO2] (Figure S10-12 and S19), [Cl_2SO] and the total pressure (Table S1-S2). Although a broad product absorption feature was observed below 320 nm, both tests implied that the Cl_2SO reformation requires the presence of the origin of the structured spectrum.

Additionally, Figure 2.2A shows that the decay rate of the structured absorption increased at higher pressures (Figure S13-17 and Table S3), implicating a possible recombination reaction or complex formation. Figure 2.2B shows the reciprocal of the temporal profiles; a linear regression was used to describe the data between 0.5-20 ms, suggesting the decay follows a second-order reaction. Figure S28 shows that similar slopes are observed for different initial intensity. This observation could be rationalized by noting that [Cl]:[ClSO] = ~1. The reaction rates of Cl

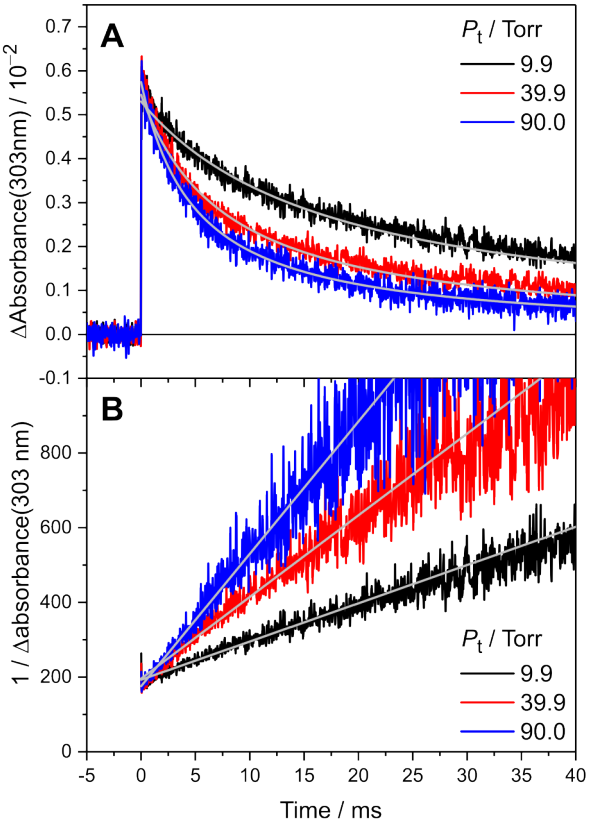

Figure 2.2: (A) Representative absorption temporal profiles near 303 nm of the Cl_2SO/N_2 photolysis system at different pressures for Exp# 1, 4 and 9 (Table S3). (B) The reciprocal of (A). The gray lines show a linear fit to 0.5-20 ms region only to lessen the impact from potential secondary reactions on the determination of the rate coefficient but good linearity was observed out to 40 ms. The gray lines in (A) are the reciprocal of linear fit in (B).

atoms with NO_2, NO and O_2 depend on the total pressure[52] and are slow under our experimental conditions. This simple model describes most of the temporal profile but small amount of hot ClSO decomposition at short time and slight residual of ClSO at long time due to distinct loss rate of Cl and ClSO could cause deviations from the simple model.

The $Cl + Cl_2SO \rightarrow Cl_2 + ClSO$ reaction potentially breaks our hypothesis. However, we ruled out this possibility since the reaction rate coefficient of $Cl + Cl_2SO$ reaction is $k_{Cl+Cl2SO} = (6\pm4)\times10^{-14}$ cm^3 $molecule^{-1}$ s^{-1},[24] which is significantly slower than the decay rate of the structured absorption. We can neglect reactions of hot Cl^*, which mainly undergo rapid deactivation to form ground state Cl atom by colliding

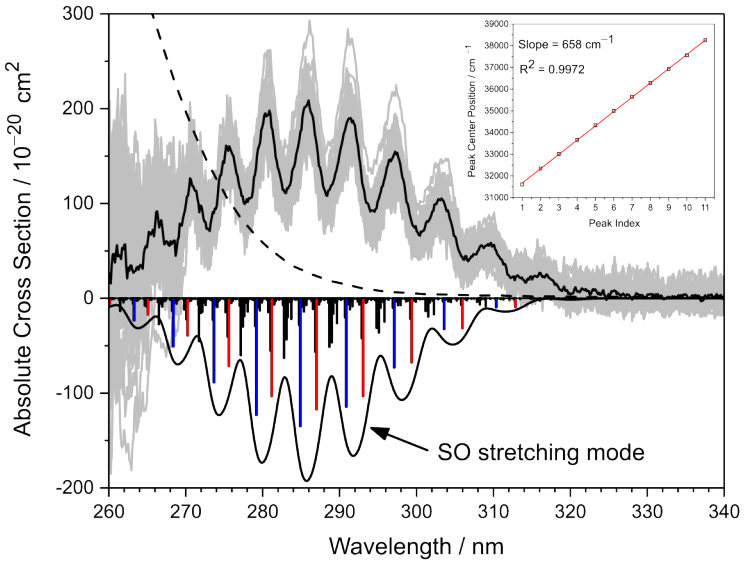

Figure 2.3: The black line is the average of all the ClSO spectra shown in gray (Table S3). The dotted line shows the cross-section of Cl_2SO for comparison. The stick diagram downward shows the calculated vibrational progression for the $1^2A"$ excited state. The red and blue bars are the SO stretching series with 0 and 1 quanta excitation of the bending mode and black line profile present the simulated spectrum (FWHM = 3 nm) of these two series (Table S6). Inset: liner fit to the observed peak centers.

with Cl_2SO.[24]

Finally, we consider the possibility that the structured absorption was due to the formation of another photolysis/reaction product or impurity. Though they are not expected to form directly in this system, no evidence of SO_2, S_2O and OClO was observed based on their distinct vibronic structures. SO can be produced directly from the photolysis of Cl_2SO, but the lowest transition energy of SO = 37940 cm^{-1} (263.6 nm),[53] below our detection window. Molecular chlorine has an absorption maximum near 330 nm, close to structured spectrum; based on the small yield of the molecule channel, (3) from the Cl_2SO photolysis,[20,21] the small absolute cross-section of Cl_2, σ_{Cl2} (330 nm) = 2.5×10^{-19} cm^2,[11] and the slow Cl self-recombination at < 100 Torr (<1.7×10^{-13} cm^3 molecule^{-1} s^{-1}),[54] we estimated an upper limit absorbance of Cl_2 < 0.05% near 330 nm. Considering that the ClSO radicals have been identified in the MIR-spectrum from Cl_2SO photolysis at 248 nm[30] and the Cl_2SO reformation was observed, we assigned the structured absorption to ClSO radicals.

Extraction of the ClSO Spectrum

The extraction of the ClSO spectrum relied on estimating the initial Cl_2SO depletion. We directly measured the Cl_2SO concentration in the reactor by monitoring its UV absorption; then, the Cl_2SO depletion was calculated from the absolute cross-section[13] and the photolysis laser fluence. Estimating radical concentration based on photolysis laser fluence alone has been challenging.[55] Therefore, this procedure was calibrated by conducting measurements on the photolytic depletion of CH_2I_2 and the formation of the simplest Criegee intermediate in the presence of O_2 under the same experimental setup (Figure S3). The laser power measured after the reactor systematically underestimated the Cl_2SO depletion. (See SI for details of estimating the $\Delta[Cl_2SO]$, initial [ClSO] and the error analysis).

As shown in Figure2.1, the negative gray lines represent the estimated initial Cl_2SO depletion. The ClSO spectra, collected under distinct conditions, were obtained by subtracting the recorded data from the Cl_2SO depletion. While hot ClSO radicals were expected from the photolysis of Cl_2SO, the IR measurements at 22 Torr Argon showed that the rotational distribution of the SO vibrational band fit well to the simulation at a rotational temperature of 350 K in the spectrum recorded within 10-40 μs.[30] Therefore, we believed that the ClSO radicals were thermalized after 0.1 ms in our experiments, which was validated by the experimental ClSO spectra recorded within 0.1-1 ms, showing no significant difference under 10-90 Torr.

Figure 2.3 shows the ClSO spectrum collected across all pressure (gray lines); only the spectra, recorded within the first millisecond, were processed to minimize the influence of the Cl_2SO reformation (Figure S20-S25). The absolute cross-section was estimated by using the radical channel yield of 96% at 248 nm.[20,21] Because a small portion (<13%)[21] of the ClSO radicals may dissociate under our experimental conditions, this estimation may be treated as a lower bound of the ClSO absolute cross-section. Recall that the isosbestic point was observed near 275 nm; the Cl_2SO depletion dominated in the absorption change below 275 nm. The gray area in Figure 2.3 roughly shows the relative uncertainty.

The average ClSO spectrum (Figure 2.3, solid black line) was fitted using multiple Gaussian peaks and was analyzed using first derivative to obtain the peak positions of the observed structure (Figure S6). As shown in the Figure 2.3 inset, the structured absorption has an average spacing of 658 cm^{-1}. To get more insights into the observed band, we performed high-level ab initio calculations to estimate the transition energies and the corresponding harmonic vibrational frequencies of ClSO

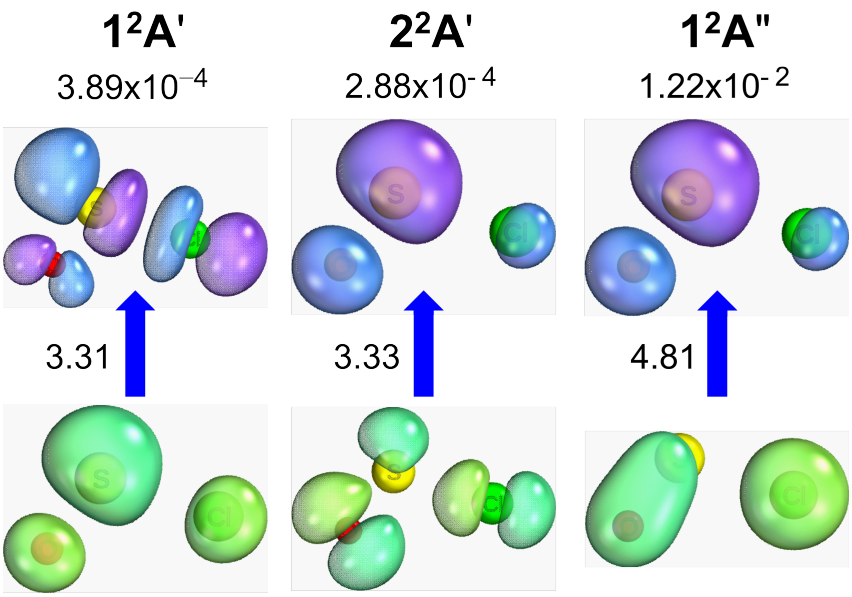

Figure 2.4: The calculated oscillator strength, vertical excitation energies (in eV) and the natural density difference orbitals (top view) for the 1^2A', 2^2A' and 1^2A" excited states calculated at EOMEE-CCSD/ano-pVQZ level and the ground state geometry.

radical.

Comparison with Theoretical Calculations

Table 2.1 summarizes all the calculation results. The electronic configuration of the X state has A" symmetry with the unpaired electron occupying the π^*orbital, as suggested by the EPR spectrum.[27] Three low lying excited states were identified, two with A' symmetry and one with A" symmetry in the C_s point group, which roughly corresponds to the alpha HOMO to LUMO (1^2A'), beta HOMO-2 to HOMO (2^2A') and beta HOMO-1 to HOMO transition (1^2A"), respectively. Figure 2.4 shows the natural density difference orbitals for these transitions. We noted that the predicted transition oscillator strengths to the two A' excited states are very small, where in contrast, the A" excited state has a stronger oscillator strength. Furthermore, the vertical transition energies to the two A excited states are close to 3.3 eV; Li et al.[35] have predicted an adiabatic transition energy to the 2^2A' excited state ~2.3 eV, which is significantly smaller than the observed band position. Considering the predicted vertical transition energy is lower than the experimental observation and the small predicted oscillator strengths, we did not further consider the two A' states in this work.

The diabatic transition energy of the 1^2A" state is 4.17 eV at EOMEE-CCSD/ano-pVQZ level. Further correction connected triples in a smaller basis set lowers the adiabatic transition energy to 3.90 eV (317.8 nm). The zero point energy correction (ZPE) yields a 0-0 transition energy of 320.1 nm. We compare this result to the adiabatic transition energy calculated at the EOMIP-CCSDT/ano-pVQZ//EOMIP-CCSD/ano-pVQZ level, which agrees within 100 cm^{-1}, with a final 0-0 transition energy agreeing within 10 cm^{-1} due to fortuitous cancellation between differences in predicted adiabatic transition energies and ZPE corrections. Nevertheless, the close agreement in adiabatic transition energies reinforces confidence in the accuracy of both calculations.

The excitation to the 1^2A" state is attributed to the $\pi^* \leftarrow \pi$ transition along the SO bond (Figure 2.4). EOMIP-CCSD predicts that the equilibrium SO bond length increases from 1.463 Å to 1.676 Å in the 1^2A" excited state while the bond angle becomes slightly smaller, with no significant change in the ClS bond length. Moreover, we found the vibrational frequency changes from 321 cm^{-1}, 542 cm^{-1}, and 1190 cm^{-1} to 259 cm^{-1}, 480 cm^{-1} and 720 cm^{-1} for the bending, ClS stretching and SO stretching modes, respectively. Notably, the SO stretching mode at the 1^2A" excited state is slightly larger than the observed average spacing.

The Franck-Condon factors are calculated by assuming a displaced harmonic oscillator model and 300 K Boltzmann weighting for hot bands to compare the observed vibrational structures (Figure 2.3). For the SO stretching (red bar), the strongest peak occurs at the $\nu_{SO} = 5 \leftarrow 0$ transition (Table S6), and a similar result was observed for the SO series with one quantum bending excitation (blue bars). The adiabatic 0-0 transition is computed to be 320.1 nm but is predicted to have no Franck-Condon overlap. From the predicted spectrum, we extrapolate the experimental progression suggests an origin between 316 and 324 nm.

By assuming Gaussian for each transition, the simulation spectrum (Figure S29) indicates that the broad feature originates from the combination bands and hot bands. Note that the simulation does not include the rotational structures, which could make the overlap region more diffuse and make the strong SO stretching series (red bar and blue bar) overlap.

We assign the observed band to the 1^2A" $\leftarrow$ X ^{2}A" transition, and the vibronic structure to the SO stretching mode. This assignment is similar to the C $\leftarrow$ X transition in S_2O where a similar vibronic structure has been observed and mainly attributed to the SS stretching mode.[56] For ClSO, due to the low resolution of the ex-

Table 2.1: The (EOM-)CCSD and CCSDT calculation of ClSO for geometries, energies relative to the optimized ground state ΔE, harmonic vibrational frequencies, and the 1^2A"←X^2A" transition energies.

SCF Reference		UHF/EOMEE		RHF/EOMIP (Anion)	
Geometry Optimized		X^2A" state	1^2A" state	X ^{2}A" state	1^2A" state
Geometry[a]	r(Cl-S) / Å	2.046	2.011	2.034	2.009
	r(S-O) / Å	1.461	1.662	1.463	1.676
	∠(ClSO) / degree	109.25	102.91	109.42	100.89
ΔE / cm^{-1}	1^2A"	38795	33596 (31465)[b]	36833[c]	31536[c]
	2^2A’	26892	-		
	1^2A’	26701	-		
	X^2A"	0	6037	0	-
Frequencies / cm^{-1}	ClSO bending	316	254	321	259
	ClS stretching	516	503	542	480
	SO stretching	1200	831	1190	720
Adiabatic transition energy / cm^{-1}		31465 (317.8 nm)[d]		31536 (317.1 nm)[d]	
0-0 transition energy / cm^{-1}		31244 (320.1 nm)[d]		31239 (320.1 nm)[d]	

[a] Optimization at the CCSD/ano-pVQZ level.
[b] After correction ΔE_{HLC} = CCSDT/ano-pVDZ – CCSD/ano-pVDZ
[c] At EOMIP-CCSDT/ano-pVQZ level
[d] The corresponding wavelength is shown in the parentheses.

perimental spectra, the contributions from rotational structure and combination/hot bands are unresolved and we could not determine the anharmonic parameter. We expect anharmonicity in the 1^2A" state to be insignificant, given that both SO and SS stretching modes in the analogous C state of S_2O exhibit small anharmonicities.[56]

The Pressure Dependence of the Cl + ClSO reaction

By assuming, the initial concentrations of the Cl atoms and ClSO radicals were similar and their loss rates through other pathways were slow compared to the recombination reaction; as a result, the rate equation of a simple second-order reaction was obtained. The integration form yields the time behavior of the absorbance change in this second-order model (2.1).

$$\Delta Abs = \frac{A_0}{1 + A_0 \frac{k_{Cl+ClSO}}{\sigma L} t} \tag{2.1}$$

where ΔAbs denotes the absorption change, A_0 denotes the peak absorption, σ denotes the ClSO absorption cross section, and L denotes the effective path length. By substituting the concentration to absorbance, the recombination rate coefficient was obtained once L and σ are known.

The second-order model (2.1) well described the observed temporal profiles measured at 303 nm to long times even though the fitting was performed within 0.5-20 ms (Figure S13-S17). The good linear behavior of the reciprocal absorption indicated that the perturbations from other reactions were small in our time window. Figure 2.5 shows the recombination rate coefficients, $k_{\mathrm{Cl+ClSO}}$, measured at different pressures using three buffer gases (He, N_2 and Ar). The recombination rate coefficients seem to reach the high-pressure limit near 90 Torr. In addition, no clear difference was observed for He, Ar and N_2 though it may be due to the data scattering.

Scheme 2.1: Proposed mechanism of Cl + ClSO $\rightarrow$ Cl_2SO reaction

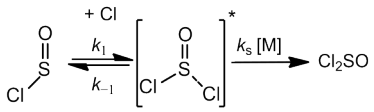

We proposed (Scheme 2.1) that Cl and ClSO may form a hot [Cl---ClSO]* complex, k_1, which could dissociate back to the reactants, k_{-1}, or collide with a third body, and be stabilized into a well to eventually form Cl_2SO, $k_s[M]$. Applying the steady-state approximation to the hot Cl_2SO^* leads to equation (2.2) for the recombination rate coefficients.

$$k_{Cl+ClSO} = \frac{k_1[M]}{\frac{k_{-1}}{k_s} + [M]} \tag{2.2}$$

This model reasonably described our data in Figure 2.5 (red line) The extrapolation of equation (2.2) yields rate coefficients for the high-pressure limit k_{inf} = (2.58±0.72)× 10^{-11} cm^3 $molecule^{-1}$ s^{-1} and for the low-pressure limit k_0 = (1.21±0.44)×10^{-29} cm^6 $molecule^{-2}$ s^{-1} (1σ uncertainty). These parameters are valid over 10-90 Torr only. Measurements over a wider pressure range are needed to give better estimations.

Due to the relative high uncertainty (1σ = 23.9%) at 10 Torr, we may consider that other bi-molecular reactions dominates under low pressure, similar to the case of the hydroperoxyl radical self-reaction, to cause a non-zero intercept at low pressure limit.[57] Possible candidates includes Cl + ClSO $\rightarrow$ Cl2 + SO ($\Delta H_0(0)$ = -6.0 kcal mol^{-1}), 2ClSO $\rightarrow$ Cl_2 + 2SO ($\Delta H_0(0)$ = -45.2 kcal mol^{-1}) and 2ClSO $\rightarrow$ Cl_2SO + SO ($\Delta H_0(0)$ = -6.1 kcal mol^{-1}). Because $k_{\mathrm{Cl+ClSO}}$ increased by a factor of three from 10 Torr to 90 Torr, the isosbestic point in the spectrum should change significantly without Cl_2SO formation; however, the spectra showed no clear changes in the isosbestic point (Fig. S20). In addition, we found that the ClSO decay rate

was roughly four times slower in the presence of I_2 (Table S1 and Figure S7-S8), indicating the ClSO self-reaction and loss rates are negligible. Possible contributions from the mixing of gases, as they enter in and pump out from the reactor, were also excluded by performing measurements at refresh rates = 4 Hz, 2 Hz and 1 Hz. Considering the reaction energy change, calculated from bond dissociation energies, the Cl + ClSO reaction has the strongest exothermicity forming Cl_2SO, supporting that it is the main decay pathway.

Although we excluded some potential effects that influence measurements from directly monitoring the decay of ClSO radicals at low pressure, it is hard to figure out all possibilities. For example, large deviation has been reported in the studies of the CH_3 recombination reaction and the secondary reactions in different photolysis system were suspected.[58]

Note that the rate coefficient $k_{Cl+ClSO}$ at 90 Torr is ~400 times faster than recombination of the Cl atoms, but a small amount of Cl_2SO depletion residual was observed when the ClSO radicals disappeared (Figure S24-S25), implying other reactions involving the Cl atom and ClSO radical occurred. The hot Cl^* atom was quickly (lifetime = ~100 μs under 90 Torr N_2)[59] quenched by buffer gas to form the ground state Cl atom and the lifetime of Cl atom could be long without the co-reactants.[24] Thus, other reactions between the ClSO radicals and unknown impurities might have contributions.

The solid angle analysis yielded an estimation of the higher-pressure limit k_{inf} = 7×10^{-11} cm^3 $molecule^{-1}$ s^{-1} by considering the ClSO ground state geometry (360°-109.25° = 250.75°) and a gas collision rate of 10^{-10} cm^3 $molecule^{-1}$ s^{-1}. The recombination rate coefficient at low pressure was expected to be faster than similar reactions, such as the Cl + NO_2 reactions, because Cl_2SO has more low frequency modes and smaller rotational constants than either ClONO or $ClNO_2$,[60] indicating a higher energy transfer efficiency and suggesting $k_{Cl+ClSO}$ is significantly larger than 3×10^{-13} cm^3 $molecule^{-1}$ s^{-1} at 10 Torr.[52] Indeed, our measurements fall between these two limits.

Potential Implications. As shown previously, a broad product absorption feature was observed in the presence of NO_2 (Figure 2.1C) and decayed slowly, indicating the origin of this broad feature is different from ClSO. While we were not certain about the identity of the origin of spectrum, we found that it is not similar to possible side products (e.g. Cl_2, NO_2, N_2O_5) and so we speculate this could be due to the adduct of ClSO and NO_2 (Figure S10-S12). Besides, the far-infrared

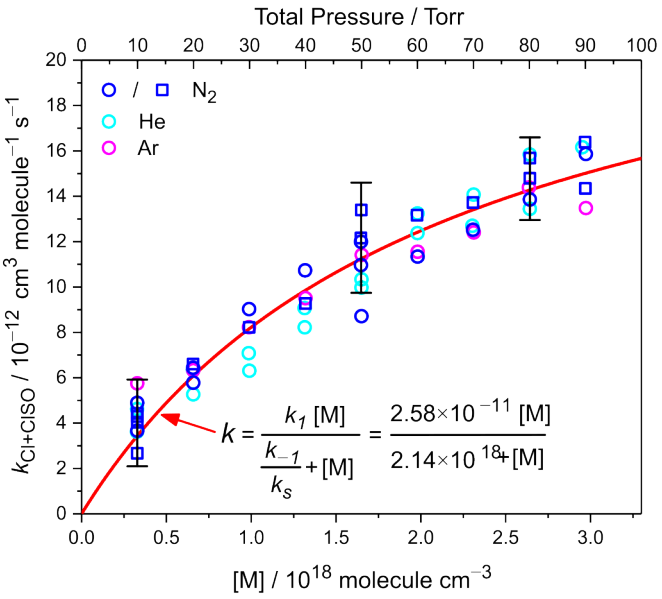

Figure 2.5: The observed rate coefficient as a function of the total pressure (assuming σ_{ClSO}(303 nm) = 1.0×10^{-18} cm^2 and L = 431.8 cm). The red line shows the fit to all the experimental data on the figure using proposed mechanism in Scheme 1. Black error bars present 2σ of the blue circles distribution. The circle (Exp #1-9 and 23-48) and square (Exp #10-22, Rep. Rate = 1 or 2 Hz, Table S3) symbol presents measurements with distinct gas refresh rates.

and rotational spectra were assigned to the ClSO radicals based on several chemical tests, including formation from the Cl + SO reaction.[28,29] It seems that SO and ClSO have the potential to be the Cl atom reservoirs by forming Cl_2SO, which was not mentioned in Venus' atmospheric models.[61,62] Furthermore, the ClSO radicals may be a general radical reservoir through recombination reactions under high pressure, which is worth further studying. This work also suggested that the Cl atom yield from Cl_2SO photolysis in the solution phase or solid phase could be even smaller than in the gas phase due to the cage effect and the high energy transfer efficiency to the environment due to the rapid Cl + ClSO $\rightarrow$ Cl_2SO reaction.

2.6 Conclusions

In this work, the UV spectrum of the ClSO radical was identified from the Cl_2SO photolysis at 248 nm using a time-resolved broadband UV-Vis transient absorption spectroscopy coupled with a Pulsed-Laser-Photolysis flow reactor. The ClSO absorption band showed clear vibronic structures with an average vibrational spacing of 658 cm^{-1}. The band maximum was observed near 286 nm with a cross-section of

(2.0±0.5) ×10^{-18} cm^2 (1σ uncertainty). In addition, high-level ab initio calculations were performed for the excited states of ClSO at EOMEE-CCSD/ano-pVQZ level. Three low-lying excited states with two A' and one A" symmetry were identified. The predicted vertical transition energies of the two A' (3.3 eV) are significantly smaller than the ClSO band position and the predicted oscillator strengths are small; in contrast, the A" has a large oscillator strength. The 1^2A" ← X ^{2}A" transition was described by the π^* ← π transition of the SO bond, resulting in longer SO bond length and a SO stretching frequency of 720 cm^{-1}. The 0-0 transition energy at EOMIP-CCSDT/ano-pVQZ//EOMIP-CCSD/ano-pVQZ level agrees well with the experiments. The Franck-Condon factors were calculated, which is similar to the overall profile of the experimental observation.

Additionally, the Cl + ClSO → Cl_2SO reaction was investigated by using the observed spectrum between 10-90 Torr (N_2, He and Ar). This recombination reaction showed a strong pressure dependence, $k_{Cl+ClSO}$ =(2.58±0.72)×10^{-11} cm^3 $molecule^{-1}$ s^{-1})[M] / (2.14×10^{18} molecule cm^{-3} + [M]) at 292 K (1σ uncertainty), which was not strongly affected by the buffer gases. This observation, combined with other literature data implies that ClSO might be a Cl atom reservoir in Venus' atmosphere. It also provided necessary data for designing a chemical system by using Cl_2SO photolysis as a Cl atom precursor. Most importantly, the observed UV spectrum offers a new approach to studying the reactivity of the ClSO radicals under a wide range of experimental conditions, including at high pressure or in the solution phase.

2.7 Acknowledgement

The experimental research herein was carried out at the Jet Propulsion Laboratory, California Institute of Technology, under contract with the National Aeronautics and Space Administration (NASA, 80NM0018D0004). Financial support was provided by the NASA Solar System Workings program and the J. Yang & Family Foundation. The authors thank Dr. Stanley Sander for discussion.

2.8 Associated Content

Supplementary texts of experimental detail and analyses, including all recorded spectra and temporal profiles

This material is available free of charge via the Internet at http://pubs.acs.org.

References

[1] Finlayson-Pitts, B. J. Chlorine chronicles. *Nature Chemistry* **2013**, *5*, 724–724.

[2] Zhu, G. et al. Rechargeable Na/Cl2 and Li/Cl2 batteries. *Nature* **2021**, *596*, 525–530.

[3] Gangadharan, R.; Namboodiri, P. N. N.; Prasad, K. V.; Viswanathan, R. THE LITHIUM-THIONYL CHLORIDE BAlTERY - A REVIEW. *Journal of Power Source* **1979**, 1–9.

[4] El-Sakka, I. A.; Hassan, N. A. Synthetic uses of thionyl chloride. *Journal of Sulfur Chemistry* **2005**, *26*, 33–97.

[5] Board, S. S.; on Engineering, D.; Sciences, P.; of Sciences Engineering, N. A.; Medicine *Thriving on Our Changing Planet: A Decadal Strategy for Earth Observation from Space: An Overview for Decision Makers and the Public*; National Academies Press: Washington, D.C., 2019; page: 25437 DOI: 10.17226/25437.

[6] Pernice, H.; Garcia, P.; Willner, H.; Francisco, J. S.; Mills, F. P.; Allen, M.; Yung, Y. L. Laboratory evidence for a key intermediate in the Venus atmosphere: Peroxychloroformyl radical. *Proceedings of the National Academy of Sciences* **2004**, *101*, 14007–14010.

[7] Mills, F. P.; Allen, M. A review of selected issues concerning the chemistry in Venus' middle atmosphere. *Planetary and Space Science* **2007**, *55*, 1729–1740.

[8] Osborn, D. L. Reaction Mechanisms on Multiwell Potential Energy Surfaces in Combustion (and Atmospheric) Chemistry. *Annual Review of Physical Chemistry* **2017**, *68*, 233–260.

[9] Baklanov, A. V.; Krasnoperov, L. N. Oxalyl ChlorideA Clean Source of Chlorine Atoms for Kinetic Studies. *The Journal of Physical Chemistry A* **2001**, *105*, 97–103.

[10] Ghosh, B.; Papanastasiou, D. K.; Burkholder, J. B. Oxalyl chloride, ClC(O)C(O)Cl: UV/vis spectrum and Cl atom photolysis quantum yields at 193, 248, and 351 nm. *The Journal of Chemical Physics* **2012**, *137*, 164315.

[11] Gibson, G. E.; Bayliss, N. S. Variation with Temperature of the Continuous Absorption Spectrum of Diatomic Molecules: Part I. Experimental, The Absorption Spectrum of Chlorine. *Physical Review* **1933**, *44*, 188–192.

[12] Pope, F. D.; Hansen, J. C.; Bayes, K. D.; Friedl, R. R.; Sander, S. P. Ultraviolet Absorption Spectrum of Chlorine Peroxide, ClOOCl. *The Journal of Physical Chemistry A* **2007**, *111*, 4322–4332.

[13] Uthman, A. P.; Demlein, P. J.; Allston, T. D.; Withiam, M. C.; McClements, M. J.; Takacs, G. A. Photoabsorption spectra of gaseous methyl bromide, ethylene dibromide, nitrosyl bromide, thionyl chloride, and sulfuryl chloride. *The Journal of Physical Chemistry* **1978**, *82*, 2252–2257.

[14] Langer, S.; McGovney, B. T.; Finlayson-Pitts, B. J.; Moore, R. M. The dimethyl sulfide reaction with atomic chlorine and its implications for the budget of methyl chloride. *Geophysical Research Letters* **1996**, *23*, 1661–1664.

[15] Cabanas, B.; Villanueva, F.; Martin, P.; Baeza, M.; Salgado, S.; Jimenez, E. Study of reaction processes of furan and some furan derivatives initiated by Cl atoms. *Atmospheric Environment* **2005**, *39*, 1935–1944.

[16] Villanueva, F.; Barnes, I.; Monedero, E.; Salgado, S.; Gómez, M. V.; Martin, P. Primary product distribution from the Cl-atom initiated atmospheric degradation of furan: Environmental implications. *Atmospheric Environment* **2007**, *41*, 8796–8810.

[17] Szori, M.; Csizmadia, I. G.; Fittschen, C.; Viskolcz, B. Theoretical Study on Reactions of HO $_2$ Radical with Photodissociation Products of Cl $_2$ SO (ClSO and SO). *The Journal of Physical Chemistry A* **2009**, *113*, 9981–9987.

[18] Donovan, R. J.; Husain, D.; Jackson, P. T. Spectroscopic and kinetic studies of the SO radical and the photolysis of thionyl chloride. *Transactions of the Faraday Society* **1969**, *65*, 2930.

[19] Kawasaki, M.; Kasatani, K.; Sato, H.; Shinohara, H.; Nishi, N.; Ohtoshi, H.; Tanaka, I. Photodissociation of Cl2SO at 248 and 193 nm in a molecular beam. *Chemical Physics* **1984**, 285–291.

[20] Baum, G.; Effenhauser, C. S.; Felder, P.; Huber, J. R. Photofragmentation of thionyl chloride: competition between radical, molecular, and three-body dissociations. *The Journal of Physical Chemistry* **1992**, *96*, 756–764.

[21] Wang, H.; Chen, X.; Weiner, B. R. Laser photodissociation dynamics of thionyl chloride: concerted and stepwise cleavage of S-Cl bonds. *The Journal of Physical Chemistry* **1993**, *97*, 12260–12268.

[22] Roth, M.; Maul, C.; Gericke, K.-H. Competitive channels in the photodissociation of thionyl chloride. *Physical Chemistry Chemical Physics* **2002**, *4*, 2932–2940.

[23] Chichinin, A.; Einfeld, T. S.; Gericke, K.-H.; Grunenberg, J.; Maul, C.; Schäfer, L. V. Photodissociation dynamics of SOCl $_2$. *Phys. Chem. Chem. Phys.* **2005**, *7*, 301–309.

[24] Rakhymzhan, A.; Chichinin, A. Excited Cl(^{2} P $_{1/2}$) Atoms: Yield from the Photodissociation of SOCl $_2$ and Collisional Deactivation by NO $_2$, CCl $_3$ H,

C_2H_4, C_3H_6, and $SOCl_2$. *The Journal of Physical Chemistry A* **2010**, *114*, 6586–6593.

[25] Abulimiti, B.; Hao, Q.-l.; Qin, C.; Xiang, M.; Zhang, B. Three-Body photodissociation of thionyl chloride. *Chinese Journal of Chemical Physics* **2018**, *31*, 257–262.

[26] Lindquist, B. A.; Dunning, T. H. The nature of the SO bond of chlorinated sulfur–oxygen compounds. *Theoretical Chemistry Accounts* **2014**, *133*, 1443.

[27] Williams, F.; Nishikida, K. Electron SpinResonanceSpectraof OSeCI, OSCl, and OSBr. *Journal of Magnetic Resonance* **1974**, *14*, 348–357.

[28] Radford, H. E.; Wayne, F. D.; Brown, J. M. Far Infrared Laser Magnetic Resonance Spectra of the ClSO and FSO Radicals in the Gas Phase. *Journal of Molecular Spectroscopy* **1983**, *99*, 209–220.

[29] Hirota, E.; Saito, S. Spectroscopy and structures of free radicals and molecular ions. *Reviews of Chemical Intermediates* **1987**, *7*, 353–388.

[30] Chu, L.-K.; Lee, Y.-P.; Jiang, E. Y. Detection of ClSO with time-resolved Fourier-transform infrared absorption spectroscopy. *The Journal of Chemical Physics* **2004**, *120*, 3179–3184.

[31] Blitz, M. A.; Goddard, A.; Ingham, T.; Pilling, M. J. Time-of-flight mass spectrometry for time-resolved measurements. *Review of Scientific Instruments* **2007**, *78*, 034103.

[32] Jr-Min Lin, J.; Chao, W. Structure-dependent reactivity of Criegee intermediates studied with spectroscopic methods. *Chemical Society Reviews* **2017**, *46*, 7483–7497.

[33] Shih, M.-C.; Chu, L.-K. Does Tetrahydrofuran (THF) Behave like a Solvent or a Reactant in the Photolysis of Thionyl Chloride (Cl_2SO) in Cyclohexane? A Transient Infrared Difference Study. *The Journal of Physical Chemistry A* **2018**, *122*, 5401–5408.

[34] Korth, H.-G. Comment on "Does Tetrahydrofuran (THF) Behave like a Solvent or a Reactant in the Photolysis of Thionyl Chloride (Cl_2SO) in Cyclohexane? A Transient Infrared Difference Study". *The Journal of Physical Chemistry A* **2019**, *123*, 7892–7894.

[35] Li, Z. Ab Initio Study of the Electronic Structure of XSO and XSO_2 (X = F, Cl) Radicals. *The Journal of Physical Chemistry A* **1997**, *101*, 9545–9550.

[36] Winiberg, F. A. F.; Zuraski, K.; Liu, Y.; Sander, S. P.; Percival, C. J. Pressure and Temperature Dependencies of Rate Coefficients for the Reaction OH + NO_2 + M $\rightarrow$ Products. *The Journal of Physical Chemistry A* **2020**, *124*, 10121–10131.

[37] Matthews, D. A.; Cheng, L.; Harding, M. E.; Lipparini, F.; Stopkowicz, S.; Jagau, T.-C.; Szalay, P. G.; Gauss, J.; Stanton, J. F. Coupled-cluster techniques for computational chemistry: The CFOUR program package. *The Journal of Chemical Physics* **2020**, *152*, 214108.

[38] Kállay, M.; Gauss, J. Calculation of excited-state properties using general coupled-cluster and configuration-interaction models. *The Journal of Chemical Physics* **2004**, *121*, 9257–9269.

[39] Stanton, J. F.; Bartlett, R. J. The equation of motion coupled-cluster method. A systematic biorthogonal approach to molecular excitation energies, transition probabilities, and excited state properties. *The Journal of Chemical Physics* **1993**, *98*, 7029–7039.

[40] Kállay, M. et al. The MRCC program system: Accurate quantum chemistry from water to proteins. *The Journal of Chemical Physics* **2020**, *152*, 074107.

[41] McCaslin, L.; Stanton, J. Calculation of fundamental frequencies for small polyatomic molecules: a comparison between correlation consistent and atomic natural orbital basis sets. *Molecular Physics* **2013**, *111*, 1492–1496.

[42] Neese, F.; Valeev, E. F. Revisiting the Atomic Natural Orbital Approach for Basis Sets: Robust Systematic Basis Sets for Explicitly Correlated and Conventional Correlated *ab initio* Methods? *Journal of Chemical Theory and Computation* **2011**, *7*, 33–43.

[43] Gauss, J.; Stanton, J. F.; Bartlett, R. J. Coupled-cluster open-shell analytic gradients: Implementation of the direct product decomposition approach in energy gradient calculations. *The Journal of Chemical Physics* **1991**, *95*, 2623–2638.

[44] Stanton, J. F. Many-body methods for excited state potential energy surfaces. I. General theory of energy gradients for the equation-of-motion coupled-cluster method. *The Journal of Chemical Physics* **1993**, *99*, 8840–8847.

[45] Stanton, J. F.; Gauss, J. Analytic energy gradients for the equation-of-motion coupled-cluster method: Implementation and application to the HCN/HNC system. *The Journal of Chemical Physics* **1994**, *100*, 4695–4698.

[46] Stanton, J. F.; Gauss, J. Analytic energy derivatives for the equation-of-motion coupled-cluster method: Algebraic expressions, implementation and application to theS 1 state of HFCO. *Theoretica Chimica Acta* **1995**, *91*, 267–289.

[47] Tajti, A.; Szalay, P. G.; Császár, A. G.; Kállay, M.; Gauss, J.; Valeev, E. F.; Flowers, B. A.; Vázquez, J.; Stanton, J. F. HEAT: High accuracy extrapolated *ab initio* thermochemistry. *The Journal of Chemical Physics* **2004**, *121*, 11599–11613.

[48] Bomble, Y. J.; Vázquez, J.; Kállay, M.; Michauk, C.; Szalay, P. G.; Császár, A. G.; Gauss, J.; Stanton, J. F. High-accuracy extrapolated *ab initio* thermochemistry. II. Minor improvements to the protocol and a vital simplification. *The Journal of Chemical Physics* **2006**, *125*, 064108.

[49] Harding, M. E.; Vázquez, J.; Ruscic, B.; Wilson, A. K.; Gauss, J.; Stanton, J. F. High-accuracy extrapolated *ab initio* thermochemistry. III. Additional improvements and overview. *The Journal of Chemical Physics* **2008**, *128*, 114111.

[50] Stanton, J. F.; Gauss, J. Analytic energy derivatives for ionized states described by the equation-of-motion coupled cluster method. *The Journal of Chemical Physics* **1994**, *101*, 8938–8944.

[51] Baklanov, A. V.; Chesnokov, E. N.; Chichinin, A. I. Rate constants for the reactions of molecular iodine with Cl, SiCl3, and SiH3 at 298 K. *International Journal of Chemical Kinetics* **1997**, *29*, 25–33.

[52] Burkholder, J. B.; Abbatt, J. P. D.; Cappa, C.; Dibble, T. S.; Kolb, C. E.; Orkin, V. L.; Wilmouth, D. M.; Sander, S. P.; Barker, J. R.; Crounse, J. D.; Huie, R. E.; Kurylo, M. J.; Percival, C. J.; Wine, P. H. JPL Publication 19-5. Chemical Kinetics and Photochemical Data for Use in Atmospheric Studies. *JPL Publication* **2020**, *19-5*, 2–7.

[53] Sarka, K.; Nanbu, S. Total Absorption Cross Section for UV Excitation of Sulfur Monoxide. *The Journal of Physical Chemistry A* **2019**, *123*, 3697–3702.

[54] Baulch, D.; Duxbury, J.; Grant, S.; Montague, D. Evaluated kinetic data for high temperature reactions. Volume 4 Homogeneous gas phase reactions of halogen- and cyanide- containing species. *J. Phys. Chem. Ref. Data* **1981**, *10*, 1–129.

[55] Groß, C. B. M.; Dillon, T. J.; Schuster, G.; Lelieveld, J.; Crowley, J. N. Direct Kinetic Study of OH and O $_3$ Formation in the Reaction of CH $_3$ C(O)O $_2$ with HO $_2$. *The Journal of Physical Chemistry A* **2014**, *118*, 974–985.

[56] Müller, T.; Vaccaro, P. H.; Pérez-Bernal, F.; Iachello, F. The vibronically-resolved emission spectrum of disulfur monoxide (S2O): An algebraic calculation and quantitative interpretation of Franck–Condon transition intensities. *The Journal of Chemical Physics* **1999**, *111*, 5038–5055.

[57] Sander, S. P.; Peterson, M.; Watson, R. T.; Patrick, R. Kinetics studies of the hydrogen dioxide + hydrogen dioxide and deuterium dioxide + deuterium dioxide reactions at 298 K. *The Journal of Physical Chemistry* **1982**, *86*, 1236–1240.

[58] Wang, B.; Hou, H.; Yoder, L. M.; Muckerman, J. T.; Fockenberg, C. Experimental and Theoretical Investigations on the Methyl-Methyl Recombination Reaction. *The Journal of Physical Chemistry A* **2003**, *107*, 11414–11426.

[59] Tyndall, G. S.; Orlando, J. J.; Kegley-Owen, C. S. Rate Coefficients for Quenching of Cl(2P1/2) by Various Atmospheric Gases. *J. Chem. Soc. Faraday Trans.* **1995**, *91*, 3055–3061.

[60] Golden, D. M. The Reaction Cl + $NO_2 \rightarrow$ ClONO and $ClNO_2$. *The Journal of Physical Chemistry A* **2007**, *111*, 6772–6780.

[61] Krasnopolsky, V. Chemical kinetic model for the lower atmosphere of Venus. *Icarus* **2007**, *191*, 25–37.

[62] Zhang, X.; Liang, M. C.; Mills, F. P.; Belyaev, D. A.; Yung, Y. L. Sulfur chemistry in the middle atmosphere of Venus. *Icarus* **2012**, *217*, 714–739.

Chapter 3

A-BAND SPECTRUM OF THE CLSO RADICAL: ELECTRONIC STRUCTURE OF THE SULFINYL GROUP

3.1 Abstract

Sulfinyl radicals (RSO) play a critical role in fields ranging from biology to atmospheric chemistry; particularly in aerosol formation. We utilized gas-phase transient-absorption spectroscopy to record the UV-Vis absorption spectrum of the ClSO radical generated from the pulsed-laser photolysis of thionyl chloride at 248 nm (40 Torr and 292 K). We detected a weak absorption spectrum from 350-480 nm with a peak at 385 nm, partially resolved vibronic bands with a spacing of 226 cm^{-1}, and a peak cross section $\sigma(385\text{nm}) = (7.6 \pm 1.9) \times 10^{-20}\text{cm}^2$. From *ab initio* calculations at the EOMEE-CCSD/ano-pVQZ level, we assigned this band to both the $1^2\text{A}' \leftarrow \text{X}^2\text{A}''$ and $2^2\text{A}' \leftarrow \text{X}^2\text{A}''$ transitions. We modeled the spectrum as a sum of a bound-to-free transition to the $1^2\text{A}'$ state a bound-to-bound transition to the $2^2\text{A}'$ state, with similar oscillator strengths; the prediction agreed well with the observed spectrum. We attributed the vibronic structure to a progression in the bending vibration of the $2^2\text{A}'$ state. Further calculations at the XDW-CASPT2 level predicted a conical intersection between the excited $1^2\text{A}'$ and $2^2\text{A}'$ potential energy surfaces near the Franck-Condon region. The geometry of the minimum energy conical intersection was similar to the ground state geometry. The lack of structure on blue side could be evidence of a short excited state lifetime arising from the strong vibronic coupling. From simplified molecular orbital analysis, we attributed the ClSO spectrum to transitions involving the out-of-plane π/π^* orbitals along the SO bond and the in-plane orbital possessing σ/σ^* character along the SCl bond. We hypothesized that these orbitals are common to other sulfinyl radicals RSO, which would share a combination of a strong and a weak transition in the UV (near 300 nm) and visible (400-600 nm) regions.

3.2 Introduction

The oxidation of sulfur-containing species (RSO_x), generated through reactions between oxygen and sulfinyl radicals (RSO), holds significant importance in various fields, including biology,[1,2] organic synthesis,[3,4] and atmospheric chemistry.[5] For instance, an important source of sulfate aerosols in the Earth's atmosphere is believed to be regulated by RSO_x oxidation, with HSO[6] and SO_2[7,8] as intermediates in the formation of sulfates.[9] Additionally, condensed sulfuric acid clouds have been observed in the middle atmosphere of Venus.[10] Strong oxidation is not expected in Venus' atmosphere due to its extremely low oxygen levels and, sulfate aerosol formation is attributed to the catalytic role of chlorine, which has been postulated to catalyze the oxidation of CO and SO to form CO_2 and SO_2.[11] To comprehend

the mechanism of sulfinyl radical oxidation and the role of chlorine atoms, direct kinetic measurements of sulfur species in the laboratory need to be conducted along with theoretical calculations to provide chemical insights.

The sulfinyl chloride radical, ClSO, is the smallest sulfinyl radical containing a chlorine atom and represents an ideal system for high-level ab initio calculations.[12] Although the ClSO radical can be easily generated through the photolysis of thionyl chloride (Cl_2SO),[13,14] available spectroscopic measurements are limited to ground-state properties such as infrared (IR),[15] far-IR,[16] and electron paramagnetic resonance[17] spectra. Furthermore, relevant theoretical studies are scarce.[18] In the absence of suitable detection methods, kinetic investigations were limited to mass spectrometric detection.[19]

Recently, we observed a strong ultraviolet spectrum of the ClSO radical near 300 nm range, which we assigned to the $1^2A'' \leftarrow X^2A''$ transition of the ClSO radical. We used the strong UV absorption to monitor ClSO and study the kinetics of the ClSO + Cl $\rightarrow$ Cl_2SO reaction at pressures ranging from 10 to 90 Torr at 292 K.[12]

Previous studies in cryogenic matrices[20–24] have shown that a few sulfinyl radicals exhibit both strong UV absorption near 300 nm and weak features near 400 nm, indicating that analogous weak features might also exist for ClSO. The goal of this work was to detect longer wavelength absorption spectrum of ClSO. We employed a White-cell-based transient UV-Vis spectrometer coupled into a flow reactor.[12] Radicals were generated by pulsed-laser-photolysis and the absorption was recorded in the 300-580 nm window. Low-lying excited electronic states were computed using Coupled Cluster and Complete Active Space Perturbation Theory (CASPT2) methods. The observed spectra were then assigned by comparison with the results from the *ab initio* calculations. Additionally, a molecular orbital (MO) based analysis was performed to provide chemical insight into the role of the Cl atom and the sulfinyl electronic structure in the ClSO radical.

3.3 Experimental Methods

The experimental instrument and the theoretical methods have been previously reported.[12] In short, a small stream of nitrogen (evaporated from liquid nitrogen) flowed through a bubbler containing Cl_2SO (Sigma-Aldrich >99%) held in a temperature-controlled bath at 292 K (Fisherbrand, Isotemp 4100). This mixture was then introduced into a flow reactor, whose pressure was monitored by a capacitance gauge (MKS 127AA-00100A) and controlled by a throttle valve (MKS type

153). The gas refreshing rate (MKS GM50A and 1179A) was slightly faster than the repetition rate of the photolysis laser (Coherent COMPex 205F, KrF). A broadband Xe plasma light source (LDLS, Energetiq EQ-99) was directed into a White cell (R = 140 cm, Acton Optics, 10 passes, $L_{\text{eff}} \approx 450$ cm). The light was then projected into a two-exit grating spectrometer (Acton SpectraPro 300i), which allowed both an image intensified CCD (Princeton Instruments PI-MAX4, 1024×256) and a photomultiplier tube (Hamamatsu R928) to collect transmitted light simultaneously. A long-pass filter (Semrock LP02-257RU-30×40) was used to separate the photolysis beam, hitting on the coated side of the filter to reduce background absorbance, from the probed beam. For measurements longer than 520 nm, a long-pass filter (Thorlabs FEL0450) was placed in front of the entrance slit of the spectrometer to remove the second-order diffraction. The concentrations of Cl_2SO ranged from (0.4-3)×10^{15} cm^{-3} and were balanced with N_2 for a total pressure of 40 Torr at a temperature of 292 K.

3.4 Theoretical Methods

All equation of motion coupled cluster (EOM-CCSD) calculations were performed using the CFOUR program suite,[25] with the exception of the unrestricted reference LR-CCSDT,[26] which was performed using the MRCC package.[27] All calculations made use of the ano-pVQZ basis set[28] which has coverage from H-Ar, as the use of atomic natural orbital (ANO) basis sets have been found to be exceptionally effective for calculating harmonic frequencies.[29] The frozen-core approximation was applied to all calculations since the ano-pVXZ basis sets were not optimized for core correlation. The ground state was optimized using CCSD with an unrestricted Hartree-Fock (UHF) reference, while the $1^2A'$ and $2^2A'$ excited states were optimized using EOMEE-CCSD. To explore the possible effects of spin contamination, we also employed restricted Hartree-Fock (RHF) references to optimize the $1^2A'$ and $2^2A'$ excited states using the EOMEA ($ClSO^+$ cation reference) and EOMIP ($ClSO^-$ anion reference) approaches, respectively. The ground state was also optimized using these two methods for calculations of the adiabatic transition energies.

Although the combination of EOM-CCSD and EOM-CCSDT provide a highly accurate treatment of dynamic correlation in the excited state, they fail to describe the behavior of the adiabatic states in a very small region about the conical intersection, yielding complex-valued energies due to the non-Hermitian character of the effective Hamiltonian.[30] To characterize the splitting of the adiabatic states in the vicinity of the conical intersection, we turned to multireference perturbation theory, in

particular XDW-CASPT2.[31] While CASPT2 is ultimately a perturbation theory and describes dynamic correlation less accurately than coupled cluster-based methods, its extended multistate variants (*e.g.* XDW-CASPT2 and XMS-CASPT2) correctly describe the topology of conical intersections. XDW-CASPT2 is especially suited for this purpose, as it interpolates between a state-specific and state-averaged Fock operators as the adiabatic states approach each other and mix. The minimum energy conical intersection (MECI) between the 1^2A' and the 2^2A' states was located via XDW-CASPT2 calculations based on a CASSCF(7,5) reference averaged over the three lowest electronic states as implemented in OpenMolcas.[32–34] [32–34] The conical intersection was located using the projected constrained optimization approach,[35,36] in which the average energy of the two states is minimized subject to the constraints[37] that the adiabatic energy difference is zero and a dummy constraint which prevents motion along the analytically computed[38] derivative coupling vector. An imaginary shift of 0.05 eV was applied for all calculations to avoid intruder states. The weighting factor used for the dynamically weighted Fock matrix was as described in Ref.[39], corresponding to the OpenMolcas keywords of DWType = 3 and DWMS = 1.0. The conical intersection was characterized in the branching plane by displaced geometries in the plane defined by the $\boldsymbol{x}$ and $\boldsymbol{y}$ vectors, which span the same plane as the $\boldsymbol{g}$ and $\boldsymbol{h}$ vectors and are related to them by rotation.[37] The displacements formed a grid in polar coordinates, with a spacing of 0.05 Å in $\boldsymbol{R}$ and 20° in θ. Parallel computations were aided by the use of GNU parallel.[40]

The absolute cross section as a function of wavelength was simulated in a rough approximation neglecting coupling between the 1^2A' and 2^2A' states as the sum of two independent spectral contributions. Franck-Condon factors for the 2^2A' $\leftarrow$ X^{2}A" transition at 0 K including Duschinsky rotation effects were calculated using the ezFCF package,[41] using vibrational frequencies and 0-0 transition energies taken from the EOMEE-CCSD/ano-pVQZ calculations. The absolute contribution to the cross section is given by

$$\sigma_{2^2A'}(\overline{\upsilon}) = \frac{2\pi^2}{3hc\epsilon_0 n_r \overline{\nu}} \left|\mu_{i,f}\right|^2 \sum_k \overline{\nu}_k^2 \left|\langle\chi_0|\chi_k\rangle\right|^2 \frac{1}{\sigma\sqrt{2\pi}} e^{\frac{-(\overline{\nu}-\overline{\nu}_k)^2}{2\sigma^2}} \qquad (3.1)$$

where σ is an empirical broadening parameter chosen to correspond to a full-width half-maximum of 100 cm^{-1}. The 1^2A' contribution to the spectrum was estimated using a multidimensional extension of the reflection principle,[42] and is given by

$$\sigma_{1^2A'}(\overline{\upsilon}) = \frac{2\pi^2}{3hc\epsilon_0 n_r}\left|\mu_{i,f}\right|^2 \sqrt{\frac{\beta}{\pi}}\,\overline{\nu}\,\exp\left(-\beta\left(\Delta E_{\text{vertical}} - \frac{\sum_i \overline{\nu}_i}{4} - \overline{\nu}\right)^2\right) \tag{3.2}$$

where β^{-1} is the norm of the gradient of the upper state in cm^{-1} (see Ref 42), and the $\overline{\nu}_i$ are the ground state vibrational frequencies (expressed in cm^{-1}). EOMEE-CCSD was used for the vertical excitation energy, excited state gradient, and transition dipole moment. The ground state CCSD vibrational frequencies were used for the $\overline{\nu}_i$.

Orbitals were visualized with the IBOView package,[43] while vibrational arrow diagrams were generated with the PyVibMS plugin[44] to pymol.[45]

3.5 Results

Experimental ClSO A-Band Spectrum

Figure 3.1 shows the recorded spectrum of the Cl_2SO/N_2 photolysis system at 40 Torr, recorded at a delay time of 100 μs. We have previously reported the strong absorption below 320 nm, which has a maximum at 303 nm and assigned it to the $1^2A'' \leftarrow X^2A''$ transition, the B-Band of the ClSO radical.[12]

We found another weak absorption, with a maximum peak position near 385 nm and exhibiting a series of vibronic bands. The apparent threshold of this weak absorption feature is around 480 nm. The slightly non-flat baseline above 500 nm shows the uncertainty in baseline under high [Cl_2SO]. The precursor may also have a small absorption (Fig. S1). A fit to the partially resolved vibrational progression observed in the experiment yielded an average spacing of 226 cm^{-1}. The progression was linear over the range observed; as shown in Figure 3.1, fitting to a quadratic function was not a statistically significant improvement.

The weak absorption band centered near 385 nm has a decay behavior identical to the absorption near 303 nm to within the experimental uncertainty (Fig. S2). The intensity was found to be proportional to the concentration of Cl_2SO in the reactor (Fig. S3-S4) when [Cl_2SO] < 1.3×10^{15} molecule cm^{-3}. The concentrations of Cl_2SO used in this experiment were quite high ([Cl_2SO] $\approx 3\times10^{15}$ molecules cm^{-3}) to ensure a large enough transient signal. However, this high concentration also resulted in strong absorption of the photolysis laser (σ(248nm) = 7.05×10^{-18} cm^2,[46] L = 45 cm, T = 37.7%), leading to inhomogeneous radical formation throughout the flow reactor along the excimer path (Fig. S4). As a result, no detailed kinetic analysis

Table 3.1: Summary of the calculations of ClSO for Geometries, Harmonic Frequencies, Adiabatic Transition Energies ΔE Relative to the Ground State, and the 0-0 Transition Energies.

SCF Reference		UHF/EOMEE			RHF/EOMIP		RHF/EOMEA	
Geometry Optimized		X^2A''	$2^2A'$	$1^2A'$	X^2A''	$2^2A'$	$X\,^2A''$	$1^2A'$
Geometry[a]	r(S-O) / Å	1.461	1.672	1.459	1.464	1.643	1.453	1.460
	r(Cl-S) / Å	2.046	2.013	2.276	2.034	2.012	2.035	2.259
	∠(ClSO) / degree	109.25	91.50	152.69	109.42	90.19	109.57	149.78
Frequency[a] / cm^{-1}	ClSO bending	316.3	226.5	214.3	320.6	221.0	323.1	232.9
	ClS stretching	515.5	550.7	333.3	541.8	544.6	533.8	345.1
	SO stretching	1199.5	735.4	1197.7	1190.3	802.8	1248.3	1195.4
ΔE / cm^{-1}	CCSD/ano-pVQZ	0	20697 (20742)[b]	18517 (16759)[b]	0	21027 (20463)[c]	0	17558 (16122)[c]
0-0 transition energy/cm^{-1} [nm]		-	20482 [488.2]	16616 [601.8]	-	20221 [494.5]	-	15956 [626.7]

[a] Optimization and frequency at the CCSD/ano-pVQZ level.
[b] Correction for the triples by ΔE_{HLC} = CCSDT/ano-pVDZ – CCSD/ano-pVDZ similar to Ref. 47
[c] At CCSDT/ano-pVQZ level.

was performed under these conditions. Based on the concentration dependence and temporal behavior at distinct wavelengths, we tentatively assigned the origin of the weak band to ClSO radicals.

We calibrated the absolute cross section of the weak band near 385 nm from the absorbance of the $1^2A'' \leftarrow X^2A''$ transition in the 310-320 nm range, which has a peak cross section, σ(303 nm) = (2.0±0.5)×10^{-18} cm^{-2}.[12] Figure S5 demonstrates that the weak band has a maximum absorption cross section σ(385 nm) = (7.6 ± 1.9)×10^{-20} cm^2 near 385 nm (1 standard deviation).

EOM-CCSD Calculations

Table 3.1 summarizes the results of coupled cluster point calculations for the X^2A'' ground state and the two lowest lying $^2A'$ excited states. The $1^2A'$ state arises from the alpha SOMO-LUMO transition, and the $2^2A'$ state from the beta SOMO-1 to SOMO transition. All three states have bound minima. The adiabatic transition energy of the $2^2A'$ state was found to be 20463 cm^{-1}, higher than that of the $1^2A'$ state (16122 cm^{-1}); there was thus no change in the energy ordering of the $^2A'$ excited states. The minimum energy of the $2^2A'$ state is predicted to be higher than the bond dissociation energy D_0(Cl-SO) = 19048 cm^{-1} using the HEAT-345(Q) method[47–50] (see Table S1), while the minimum of the $1^2A'$ state is predicted to be below D_0(Cl-SO). The observed absorption band lies well above dissociation.

The $1^2A'$ excited state is characterized by a large ClSO angle and a longer ClS bond length than those of the X^2A'' state. The $2^2A'$ excited state has an almost 90° ClSO

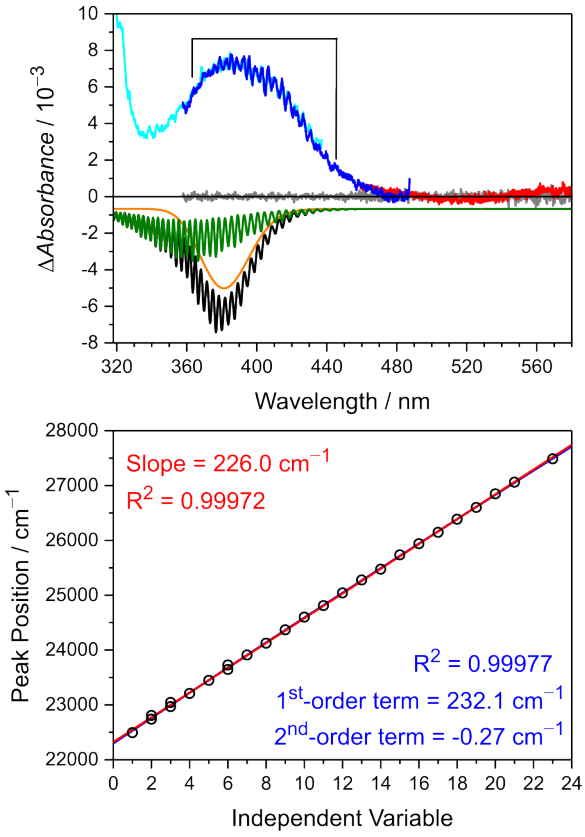

Figure 3.1: (Upper Panel) The recorded spectrum of the Cl_2SO/N_2/248 nm system at 100 μs after pulsed laser (exposure time = 117.5 μs, averaged for 12288 shots) at 40 Torr and 292 K. Cyan, blue, and red lines represent spectra at different grating angles (center wavelengths of 370 nm, 420 nm, and 520 nm), while the gray lines show the background noise without Cl_2SO. The black simulated spectra downward is the sum of contributions from both the $1^2A'$ (orange) and $2^2A'$ (olive, stick spectra convoluted with a Gaussian function with FWHM = 100 cm^{-1}) states. The comparison between experimental and theoretical absolute cross sections is shown in Figure S5. (Lower Panel) Linear and quadratic fits to the observed positions of the vibrational peaks, within the marked region.

angle and a longer SO bond length and is closer to the geometry of the ground state. Both ^{2}A' excited states have lower bending frequencies (214 cm^{-1} and 227 cm^{-1}) than the ground state (316 cm^{-1}). The 1^2A' state has a lower ClS stretching frequency (333 cm^{-1}) than the ground state, while 2^2A' has a lower SO stretching frequency (735 cm^{-1}); both results are consistent with the respective bond length changes. Further calculations utilizing closed shell references produced results that were similar to the EOMEE calculations, suggesting minimal spin contamination effects.

Assignment of 385 nm Spectrum

Both low-lying A' excited states are predicted to have similar vertical excitation energies consistent with the observed band at 385 nm.[12] The transition to the 1^2A' state is dissociative, while the transition to the 2^2A' is bound. The observed cross section is within a factor of two of the theoretical absolute cross section maximum, σ_{the}(377 nm) = 1.8 ×10^{-19} cm^2 . The cross-section relative to that of the strong B-Band is consistent with the oscillator strengths that we previously predicted. We found $f(1^2\text{A}') = 3.89\times10^{-4}$, $f(2^2\text{A}') = 2.88\times10^{-4}$ and $f(1^2\text{A}'') = 1.22\times10^{-2}$ for transition to the higher excited states.[12] The ratio of the predicted oscillator strengths is $(f(1^2\text{A}'')/(f(1^2\text{A}') + f(2^2\text{A}'))= 18.0$, consistent with the ratio of the observed absolute cross sections at the peaks, $\sigma(305\text{nm})/\sigma(385\text{nm}) = 2.0 \times 10^{-18}\text{cm}^{-2}/7.6 \times 10^{-20}\text{cm}^{-2} = 26.3$.

The bending frequencies predicted for both ^{2}A' states agree well with the experimentally observed vibrational progression of 266 cm^{-1} (see Fig. 1). In addition, Figure 3.2 shows doublet peaks at 422 nm, 435 nm, and 439 nm, which may be attributed to the difference between the SO stretching frequency and three times the bending frequency of 2^2A' state. For instance, the doublet peak at 435 nm could correspond to the (4,2,0) ← (0,0,0) and (3,5,0) ← (0,0,0) transitions, leading to an estimated frequency for the SO stretching mode of 755 cm^{-1}. From the calculated Franck-Condon contour, we extrapolated the origin to be roughly near 490 nm (20400 cm^{-1}), which is consistent with the 0-0 transition energy of the 2^2A' state shown in Table 3.1.

The observed vibrational structure disappears on the blue side, while the simulated spectrum exhibits a clear vibrational progression of 2^2A' state across the whole band. The peak broadening on the blue side might be due to congestion and anharmonicity, or decreases in the lifetime of the 2^2A' excited state caused by internal conversion (*vide infra*, see "Influence of the Conical Intersection").

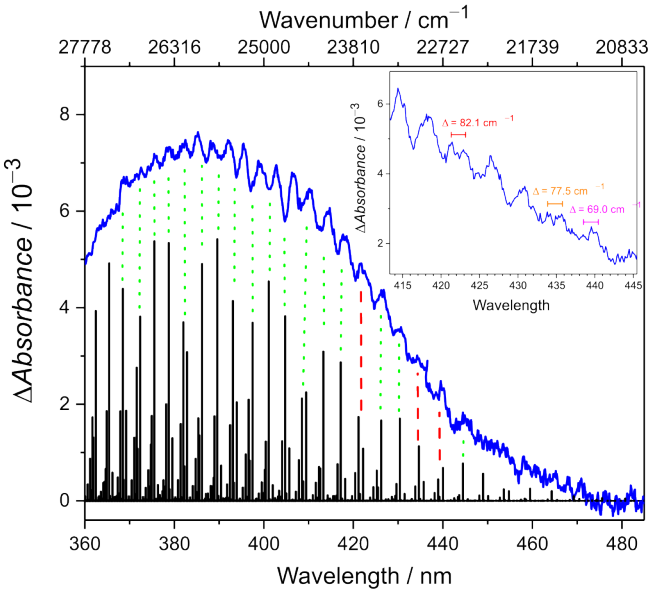

Figure 3.2: A closer look at the structure of the weak absorption band in the 360-480 nm range. A few doublet peaks were observed, yielding an average spacing of 76 cm^{-1}. The stick spectrum displays the intensities predicted for excitation to the 2^2A' state, incorporating Franck-Condon factors and thermal population effects at 0 K. The energy of the computed transition origin has been shifted to the red by 870 cm^{-1} for alignment with the vibronic progression of experimental spectrum (green dotted lines), while the red dashed lines indicate predicted doublets. Inset is a magnification of the spectrum between 415 and 445 nm.

A few peaks within the 320-360 nm range (Fig. S6) were also observed, which have a small spacing of approximately 367 cm^{-1} and large spacing of 1060 cm^{-1}. These energy differences are close to the calculated ClS stretching and SO stretching frequencies of the 1^2A' state and may warrant further theoretical investigation.

As a first order approximation, we modeled the spectrum with the EOMEE-CCSD/ano-pVQZ results, assuming that the spectrum was the incoherent sum of the 1^2A' $\leftarrow$ X^{2}A" and 2^2A' $\leftarrow$ X^{2}A" transitions weighted by the computed oscillator strengths (See Figure 3.1). We treated the bound-to-bound transition to the 2^2A' state as two independent displaced harmonic oscillator models based on the minimum energy geometries of the X^{2}A" and 2^2A' states adopted from the EOMEE-CCSD/ano-pVQZ calculations including Duschinsky rotation and thermal effects at 0 K (Fig. S7). We simulated the 1^2A' $\leftarrow$ X^{2}A" transition using a multidimensional extension of the reflection principle. The two states had roughly equal contributions.

Prediction of a Conical Intersection between the 1^2A' and 2^2A' States

Table 3.2: Summary the geometries and energy difference relative to the ground state, ΔE, calculated at the XDW-CASPT2(7,5) level.

Optimized Geometry	X^2A''	$1^2A'$	$2^2A'$	MECI
r(S–O) / Å	1.446	1.480	1.688	1.593
r(Cl–S) / Å	2.007	2.259	1.997	2.010
∠(ClSO) / degree	111.8	156.1	93.0	119.2
x (Branching Space) / Å	-0.0283	-0.4444	+0.2473	0
y (Branching Space) / Å	-0.0549	+0.1769	-0.1508	0
z (Seam Space) / Å	+0.1611	-0.4138	+0.3517	0
ΔE / cm^{-1}	0	14431	23198	26414

Our previous calculations found that the vertical excitation energies of the two ^{2}A'states were very close in energy. This result suggested that a conical intersection between **$1^2A'$ and $2^2A'$ states might** exist near the ground state geometry. To investigate this phenomenon, we generated a cut of the bending potential energy curve by linearly connecting the geometries of the X^2A'', $1^2A'$ and $2^2A'$ states (Fig. S8). We employed the EOMIP and EOMEA approaches to treat the $1^2A'$ and $2^2A'$ independently (Fig. S9). In addition, the EOMEE/ano-pVTZ calculation failed to converge at the upper state (Fig. S10).

To locate the conical intersection, we explored the lowest three potential energy surfaces (PES) of the ClSO radical using XDW-CASPT2[31,39] with a 7 electrons in 5 orbitals CASSCF reference. The active orbitals at the ground state equilibrium geometry are pictured in Figure 3.5. The resulting equilibrium geometries and relative energies are summarized in Table 3.2.

We found a sloped-type conical intersection of the $1^2A'$ and $2^2A'$ states, as depicted in Figure 3.3, with a minimum energy conical intersection at 26414 cm^{-1}, close to the peak of the absorption. The geometries of the MECI and the ground state are similar with the SO bond slightly longer the MECI. Indeed, we found the change between the X^2A'' and MECI in the branching space is small (0.06 Å, Table 3.2) with a larger change in seam space, indicating that the two ^{2}A' excited state PES do cross near the Franck-Condon region, although the MECI is slightly far away from the ground state geometry.

The corresponding motions of the ***x*** and ***y*** vectors[37] in the branching space as well as the motions in seam space are also illustrated in Figure 3.4. Motion along the **x** vector (large contribution from the anti-symmetric stretch) on the lower surface

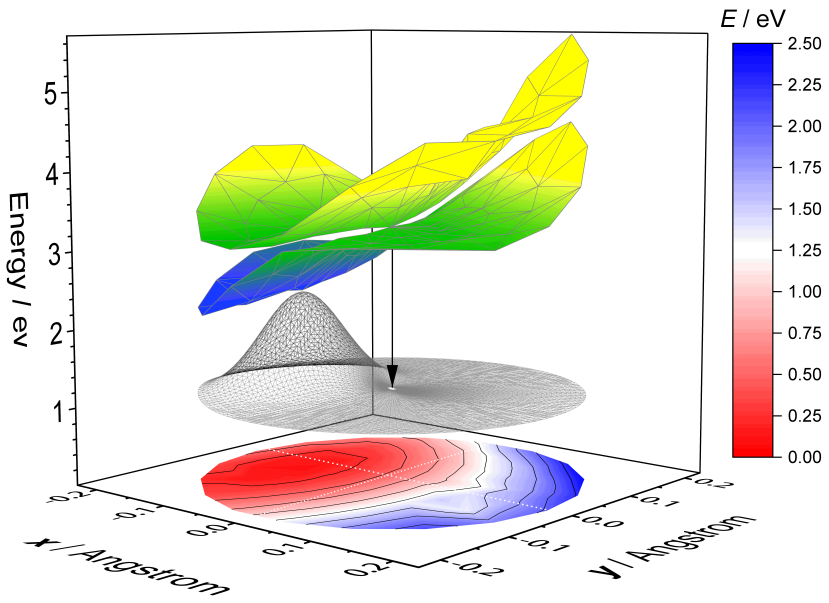

Figure 3.3: The adiabatic potential energy surface of the ground state and two excited ^{2}A' states of the ClSO radical in the 2D branching space (x, y; see Figure 3.4) computed at the XDW-CASPT2(7,5)-3SA level near the MECI geometry (x = 0, y = 0). The meshed line shows the profile of the ground state vibrational wavefunction. The black arrow shows the vertical transition from the MECI to the ground state PES (which is flattened for clarity; the color bar to the right gives the energy scale of the ground state PES contours).

lowers the energy, presumably leading to the 1A' well (contracting the SO bond and elongating the SCl bond). Motion along the **y** vector mainly consisted of the symmetric stretching.

The bending mode is the primary motion along the seam space (Fig. 4), *i.e.* the degeneracy of the conical intersection is preserved as the molecule bends. The bending motion thus has the weakest vibronic coupling among the three vibrational modes. As a result, we expect the lifetimes of the bending vibronic excited states to be longer than other modes, consistent with the observation of the bending motion as the most prominent structural feature in the experimental spectrum.

3.6 Discussion

Influence of the Conical Intersection

Our current time-independent, low-resolution absorption spectrum does not provide more information about the interactions between both A' states near the conical intersection. We attributed the observed structure to the 2^2A' $\leftarrow$ X^2A" state, but

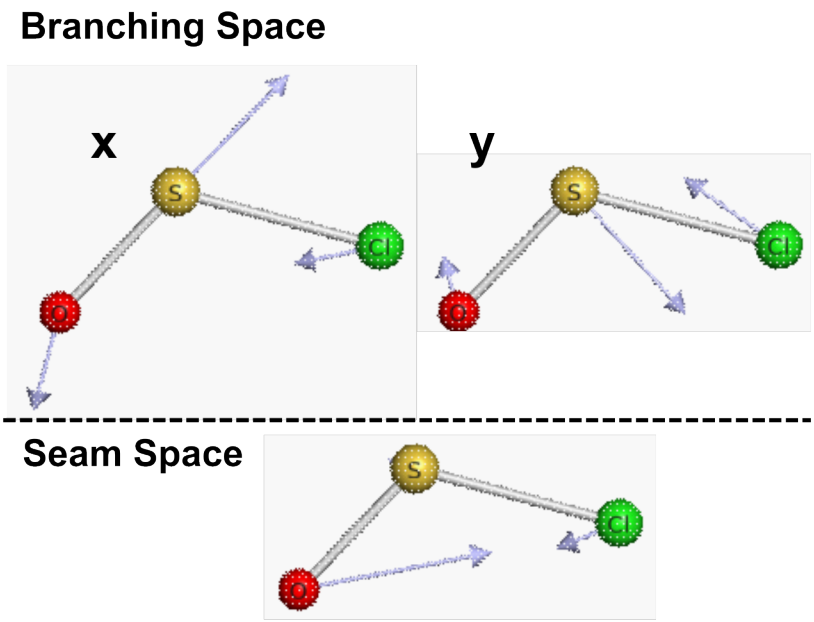

Figure 3.4: The corresponding vibrational motions of the seam space (the set of geometries where the 1^2A' and 2^2A' states are degenerate) and the branching space (the complement of seam space) near the MECI geometry.

both the 1^2A' and 2^2A' states contribute to the observed band. While we simulated the spectrum as an incoherent excitation of the two adiabatic states, the true excitation process produces a superposition of the two states, and the coefficients of each state vary with energy, in part due to changing vibronic coupling across the band. Additionally, the excited wavepacket would undergo nonadiabatic dynamics on the coupled 1^2A' and 2^2A' states, especially near conical intersection, resulting in a shorter lifetime and account for the loss of vibrational structure toward the blue side of the band. The predominant Franck-Condon active mode in the vibrational progression of the observed spectrum is the ClSO bending, consistent with the prediction of the bending mode as the motion along the seam space. However, broadening on the blue side and observation of the bending progression can result from other effects, and can provide only circumstantial evidence for the presence of a conical intersection.

The fate of the excited state is unclear. The molecule excited to the 2^2A' state could relax to the lower 1^2A' state via the conical intersection along the **x** branch; subsequent collisions could further relax the molecule below the dissociation limit into the bound 1^2A' well, at which point the molecule could reach the ground state by internal conversion, collisional quenching or fluorescence.

To quantitatively predict the effects from the conical intersection on the observed spectrum is a challenging question and goes beyond the scope of this study. Use of a single-shot vibronic coupling model based on EOM-CCSD in the spirit of Ichino *et al.*[51] is complicated by the lack of a single, closed-shell, non-interacting reference state. Furthermore, the two electronic states share the same irreducible representation, leading to orbital mixing at the SCF level resulting in diabats which hold little chemical significance.

Molecular Orbital Diagram of ClSO Radical

Figure 3.5 summarizes the valence electronic structure of the ClSO radical. To construct this MO diagram, we used the ionization energies of the SO molecule (10.3 eV)[52] and Cl atom (13.0 eV)[53] to establish the relative energy positions.

Figure S11 depicts the nine molecular orbitals resulting from the combination of 6σ, 2π, $2\pi^*$, and 7σ orbitals of SO, along with the *3p* orbitals of the Cl atom under C_s symmetry. These orbitals can be broadly classified as bonding, anti-bonding, and non-bonding. The term non-bonding here is used loosely, referring to orbitals which exhibit both bonding and anti-bonding characteristics simultaneously along distinct chemical bonds.

For instance, the second occupied molecular orbital (SOMO-1) is a combination of an in-plane π^* orbital along the SO bond and a σ orbital along the ClS bond. This can be interpreted as the SO moiety being stabilized by donating electrons from a π^* orbital into the *3p* orbital of the Cl atom. We may expect that the reactivity does not change significantly respect to the SO molecule, supported by the nearly identical SO bond length compared to free SO molecules (r_{SO} = 1.48 Å).[54] Since the ClSO + Cl $\rightarrow$ Cl_2SO reaction has been reported,[12] we expect that the association reaction of SO + Cl $\rightarrow$ ClSO also occurs.

This MO analysis of the ClSO radical provides insights into the electronic structure of other sulfinyl radicals. This is because the ionization energy of the *3p* orbitals of the Cl atom is similar to the ionization energies of H, C, N, and O atoms;[55] also, a radical species usually possesses seven electrons around the radical center, occupying three perpendicular orbitals similar to those of the Cl atom.

We predict that transitions from the SOMO-1 to the SOMO orbital are likely to occur commonly in other sulfinyl radicals and will resemble the 2^2A' $\leftarrow$ X^2A" transition observed in ClSO radicals. Furthermore, a strong $\pi^*_{SO} \leftarrow \pi_{SO}$ transition will also be present, similar to the ClSO 1^2A" $\leftarrow$ X^2A" transition. Indeed, the literature has

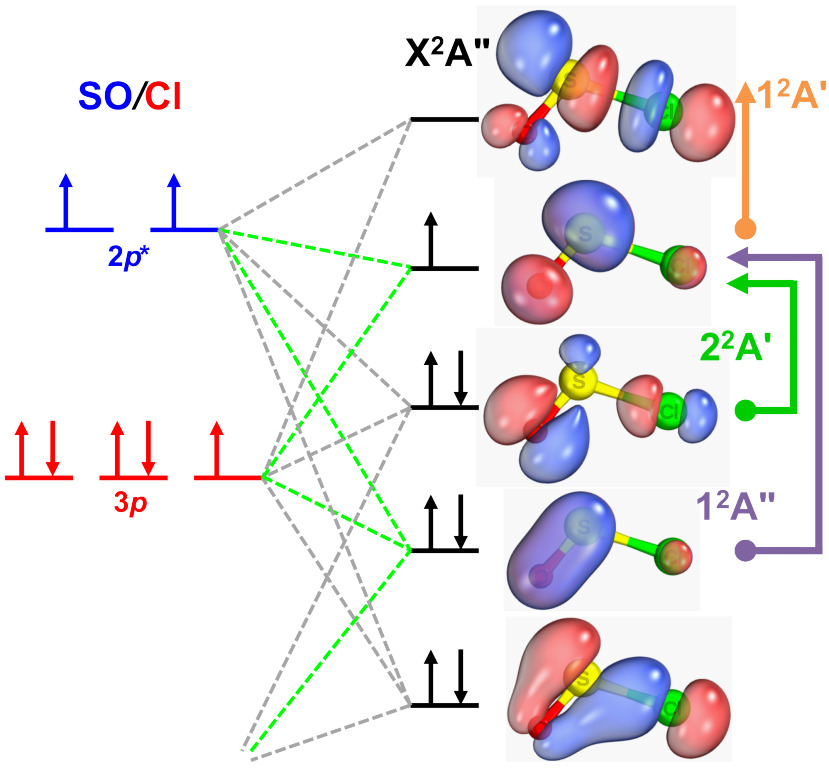

Figure 3.5: Schematic MO diagram showing the active space orbitals of the ClSO radical (top view) used in the XDW-CASPT2 calculation. Vertical and horizontal arrows indicate transitions to excited states for alpha and beta electrons. The green lines connect orbitals with the out-of-plane orientation.

reported the presence of these two distinct transitions in certain sulfinyl radicals, as summarized in Table 3.3.

Peroxyl radicals (RO_2) are approximately isoelectronic molecules of sulfinyl radicals. Experiments have shown that two transitions within the near-IR and UV-Vis regions are commonly observed in peroxyl radicals. Weisman and Head-Gordon[59] have successfully explained the observed trend in band positions using a MO picture.

Building upon similar concepts, we have concluded that the $\pi^*_{SO} \leftarrow \pi_{SO}$ transition in sulfinyl radicals occurs at a similar band position due to the minimal mixing of orbital character from the substitution group. Conversely, the band positions of SOMO $\leftarrow$ SOMO-1 transitions cover a wide range of wavelengths because the energy of the SOMO-1 orbital dependents on the characteristics of the substitution groups.

It is noteworthy that the chemiluminescence spectrum of HSO has been detected[57] in the visible range for the SOMO $\leftarrow$ SOMO-1 transition,[60] which suggests that

Table 3.3: Summary of the UV-Vis absorption band positions of distinct sulfinyl radicals (RSO).

Unit / nm	$\pi^*_{SO} \leftarrow \pi_{SO}$	SOMO ← SOMO-1	Sample Phase
SO	190 – 240	-	Gas[56]
H–SO		520 – 960[a]	Gas[57]
HO–SO	~270	300 – 500	Ne-matrix[21]
H_3C–SO	260 – 300	450 – 635	Ar-matrix[20]
F_3C–SO	250 – 300	490 – 610	Ar-matrix[23]
C_6H_5–SO	260 – 350	410 – 470	Ar-matrix[22]
	~300	~450	Solution(C_6H_{12})[58]
$H_2CC(H)$–SO	240 – 310	350 – 490	N_2-matrix[24]
Cl–SO	260 – 320	350 – 460	Gas

[a] Chemiluminescence Emission Spectrum

ClSO radical might fluoresce after excitation to the A-band and could work as a better tool to study the chemical reactivity and kinetics.

3.7 Conclusions

In this work, we recorded the UV-Vis absorption spectrum of the ClSO radical in the gas phase, in the 320-500 nm range at 40 Torr and 292K, denoted the A-Band. We observed a new, weak band having a partially resolved vibrational progression with an average spacing of 226 cm-^{1}. We determined the peak cross section by calibrating with the cross section of the much stronger B-Band at 303 nm.

We assigned the band as an excitation to the continuum of the 1^2A' excited state and the bound 1^2A' excited state. Using the EOM-CCSD/ano-pVQZ method, we calculated the properties of the two doublet excited states in this region, both with A' symmetry in the C_s point group. Both states could contribute to the absorption intensity since they have similar vertical excitation oscillator strengths. The 1^2A' excited state had a minimum below the dissociation limit and possessed a larger bond angle and longer ClS bond length, while the 2^2A' excited state lying above the dissociation limit exhibited a nearly 90° bond angle and a longer SO bond length. We simulated the spectrum as a sum of the bound-free 1^2A' $\leftarrow$ X^2A" transition and the bound-bound 2^2A' $\leftarrow$ X^2A" transition. By comparing the calculated harmonic frequency and predicted 0-0 transition energy, we assigned the observed vibronic progression to the bending mode of the 2^2A' $\leftarrow$ X^2A" transition.

We conducted XDW-CASPT2 calculations and identified a conical intersection between the 1^2A' and 2^2A' excited states. The geometry of the minimum energy

conical intersection was found to be similar to the ground state geometry, indicating that the conical intersection was near the Franck-Condon region of the A-Band transition, suggesting that the two ^{2}A' excited states will mix due to strong vibronic coupling; a short lifetime of the 2^2A' state is expected and could account for the unresolved vibrational progression on the blue side of the band.

The observed spectrum provides only indirect evidence for the presence of this conical intersection. A complete theoretical understanding of the spectroscopic effects of this phenomenon will require accurate descriptions of the potential energy surfaces, vibronic couplings, and dynamical effects. Experimentally, the existence of the conical intersection could be demonstrated by high-resolution spectra, fluorescence spectra, and probes of possible photodissociation dynamics (e.g. molecular-beam photofragment-translational spectroscopy or stimulated Raman spectroscopy).

Finally, we have constructed a simplified MO diagram to illustrate our understanding of the electronic structure of the ClSO radical, which also highlights similarities to other sulfinyl radicals. This diagram serves as a useful tool in understanding the trends of the observed band positions, considering the effects of substitution groups on the orbital characteristics. In general, species containing the sulfinyl group can be anticipated to display strong absorption around 300 nm, while weaker bands with distinct features are expected within the range of 400–600 nm.

3.8 Associated Content

Supplementary Information

SI contains supplementary figures for experimental details and analyses. This material is available free of charge via the Internet at http://pubs.acs.org.

The reported experimental and theoretical absorption cross sections are available via the Caltech Research Data Repository.

Funding Sources

National Aeronautics and Space Administration (NASA) and J. Yang and Family Foundation

3.9 Acknowledgement

The experimental research herein was carried out at the Jet Propulsion Laboratory, California Institute of Technology, under contract with the National Aeronautics and Space Administration (NASA). Financial support was provided by the NASA Solar

System Workings program, grant 80NM0018F0612, and partial fellowship support for WC from the J. Yang and Family Foundation.

References

[1] Bonini, M. G.; Augusto, O. Carbon Dioxide Stimulates the Production of Thiyl, Sulfinyl, and Disulfide Radical Anion from Thiol Oxidation by Peroxynitrite. *Journal of Biological Chemistry* **2001**, *276*, 9749–9754.

[2] Schöneich, C. Sulfur Radical-Induced Redox Modifications in Proteins: Analysis and Mechanistic Aspects. *Antioxidants & Redox Signaling* **2017**, *26*, 388–405.

[3] El-Sakka, I. A.; Hassan, N. A. Synthetic uses of thionyl chloride. *Journal of Sulfur Chemistry* **2005**, *26*, 33–97.

[4] Zhang, Z.; Wang, X.; Sivaguru, P.; Wang, Z. Exploring the synthetic application of sulfinyl radicals. *Organic Chemistry Frontiers* **2022**, *9*, 6063–6076.

[5] Mardyukov, A.; Schreiner, P. R. Atmospherically Relevant Radicals Derived from the Oxidation of Dimethyl Sulfide. *Accounts of Chemical Research* **2018**, *51*, 475–483.

[6] Iraqi, M.; Goldberg, N.; Schwarz, H. Structural Characterization of the Atmospherically Important Sulfur Compounds HSO.bul. and SOH.bul. by Charge Reversal and Neutralization-Reionization Mass Spectrometry. *The Journal of Physical Chemistry* **1994**, *98*, 2015–2017.

[7] Wallace, P. J.; Edmonds, M. The Sulfur Budget in Magmas: Evidence from Melt Inclusions, Submarine Glasses, and Volcanic Gas Emissions. *Reviews in Mineralogy and Geochemistry* **2011**, *73*, 215–246.

[8] Visioni, D.; Pitari, G.; Aquila, V. Sulfate geoengineering: a review of the factors controlling the needed injection of sulfur dioxide. *Atmospheric Chemistry and Physics* **2017**, *17*, 3879–3889.

[9] Saxena, P.; Seigneur, C. On the oxidation of SO2 to sulfate in atmospheric aerosols. *Atmospheric Environment (1967)* **1987**, *21*, 807–812.

[10] Zhang, X.; Liang, M. C.; Mills, F. P.; Belyaev, D. A.; Yung, Y. L. Sulfur chemistry in the middle atmosphere of Venus. *Icarus* **2012**, *217*, 714–739.

[11] DeMore, W. B.; Yung, Y. L. Catalytic Processes in the Atmospheres of Earth and Venus. *Science* **1982**, *217*, 1209–1213.

[12] Chao, W.; Jones, G. H.; Okumura, M.; Percival, C. J.; Winiberg, F. A. F. Spectroscopic and Kinetic Studies of the ClSO Radical from Cl $_2$ SO Photolysis. *Journal of the American Chemical Society* **2022**, *144*, 20323–20331.

[13] Baum, G.; Effenhauser, C. S.; Felder, P.; Huber, J. R. Photofragmentation of thionyl chloride: competition between radical, molecular, and three-body dissociations. *The Journal of Physical Chemistry* **1992**, *96*, 756–764.

[14] Wang, H.; Chen, X.; Weiner, B. R. Laser photodissociation dynamics of thionyl chloride: concerted and stepwise cleavage of S-Cl bonds. *The Journal of Physical Chemistry* **1993**, *97*, 12260–12268.

[15] Chu, L.-K.; Lee, Y.-P.; Jiang, E. Y. Detection of ClSO with time-resolved Fourier-transform infrared absorption spectroscopy. *The Journal of Chemical Physics* **2004**, *120*, 3179–3184.

[16] Radford, H. E.; Wayne, F. D.; Brown, J. M. Far Infrared Laser Magnetic Resonance Spectra of the ClSO and FSO Radicals in the Gas Phase. *Journal of Molecular Spectroscopy* **1983**, *99*, 209–220.

[17] Williams, F.; Nishikida, K. Electron SpinResonanceSpectraof OSeCI, OSCl, and OSBr. *Journal of Magnetic Resonance* **1974**, *14*, 348–357.

[18] Li, Z. Ab Initio Study of the Electronic Structure of XSO and XSO $_2$ (X = F, Cl) Radicals. *The Journal of Physical Chemistry A* **1997**, *101*, 9545–9550.

[19] Blitz, M. A.; Goddard, A.; Ingham, T.; Pilling, M. J. Time-of-flight mass spectrometry for time-resolved measurements. *Review of Scientific Instruments* **2007**, *78*, 034103.

[20] Reisenauer, H. P.; Romański, J.; Mlostoń, G.; Schreiner, P. R. Matrix isolation and spectroscopic properties of the methylsulfinyl radical CH3(O)S˙. *Chemical Communications* **2013**, *49*, 9467.

[21] Lu, B.; Trabelsi, T.; Esposito, V. J.; Fortenberry, R. C.; Francisco, J. S.; Zeng, X. Spectroscopic Characterization of HSO $_2$ $^\bullet$ and HOSO $^\bullet$ Intermediates Involved in SO $_2$ Geoengineering. *The Journal of Physical Chemistry A* **2021**, *125*, 10615–10621.

[22] Xu, J.; Wu, Z.; Wan, H.; Deng, G.; Lu, B.; Eckhardt, A. K.; Schreiner, P. R.; Trabelsi, T.; Francisco, J. S.; Zeng, X. Phenylsulfinyl Radical: Gas-Phase Generation, Photoisomerization, and Oxidation. *Journal of the American Chemical Society* **2018**, *140*, 9972–9978.

[23] Wu, Z.; Xu, J.; Deng, G.; Chu, X.; Sokolenko, L.; Trabelsi, T.; Francisco, J. S.; Eckhardt, A. K.; Schreiner, P. R.; Zeng, X. The Trifluoromethyl Sulfinyl and Oxathiyl Radicals. *Chemistry - A European Journal* **2018**, *24*, 1505–1508.

[24] Wu, Z.; Wang, L.; Lu, B.; Eckhardt, A. K.; Schreiner, P. R.; Zeng, X. Spectroscopic characterization and photochemistry of the vinylsulfinyl radical. *Physical Chemistry Chemical Physics* **2021**, *23*, 16307–16315.

[25] Matthews, D. A.; Cheng, L.; Harding, M. E.; Lipparini, F.; Stopkowicz, S.; Jagau, T.-C.; Szalay, P. G.; Gauss, J.; Stanton, J. F. Coupled-cluster techniques for computational chemistry: The CFOUR program package. *The Journal of Chemical Physics* **2020**, *152*, 214108.

[26] Kállay, M.; Gauss, J. Calculation of excited-state properties using general coupled-cluster and configuration-interaction models. *The Journal of Chemical Physics* **2004**, *121*, 9257–9269.

[27] Kállay, M. et al. The MRCC program system: Accurate quantum chemistry from water to proteins. *The Journal of Chemical Physics* **2020**, *152*, 074107.

[28] Neese, F.; Valeev, E. F. Revisiting the Atomic Natural Orbital Approach for Basis Sets: Robust Systematic Basis Sets for Explicitly Correlated and Conventional Correlated *ab initio* Methods? *Journal of Chemical Theory and Computation* **2011**, *7*, 33–43.

[29] McCaslin, L.; Stanton, J. Calculation of fundamental frequencies for small polyatomic molecules: a comparison between correlation consistent and atomic natural orbital basis sets. *Molecular Physics* **2013**, *111*, 1492–1496.

[30] Köhn, A.; Tajti, A. Can coupled-cluster theory treat conical intersections? *The Journal of Chemical Physics* **2007**, *127*, 044105.

[31] Battaglia, S.; Lindh, R. Extended Dynamically Weighted CASPT2: The Best of Two Worlds. *Journal of Chemical Theory and Computation* **2020**, *16*, 1555–1567.

[32] Fdez. Galván, I. et al. OpenMolcas: From Source Code to Insight. *Journal of Chemical Theory and Computation* **2019**, *15*, 5925–5964.

[33] Li Manni, G. et al. The OpenMolcas *Web* : A Community-Driven Approach to Advancing Computational Chemistry. *Journal of Chemical Theory and Computation* **2023**, acs.jctc.3c00182.

[34] Aquilante, F. et al. Modern quantum chemistry with [Open]Molcas. *The Journal of Chemical Physics* **2020**, *152*, 214117.

[35] Anglada, J. M.; Bofill, J. M. A reduced-restricted-quasi-Newton–Raphson method for locating and optimizing energy crossing points between two potential energy surfaces. *Journal of Computational Chemistry* **1997**, *18*, 992–1003.

[36] De Vico, L.; Olivucci, M.; Lindh, R. New General Tools for Constrained Geometry Optimizations. *Journal of Chemical Theory and Computation* **2005**, *1*, 1029–1037, publisher: American Chemical Society.

[37] Fdez. Galván, I.; Delcey, M. G.; Pedersen, T. B.; Aquilante, F.; Lindh, R. Analytical State-Average Complete-Active-Space Self-Consistent Field Nonadiabatic Coupling Vectors: Implementation with Density-Fitted Two-Electron Integrals and Application to Conical Intersections. *Journal of Chemical Theory and Computation* **2016**, *12*, 3636–3653.

[38] Nishimoto, Y.; Battaglia, S.; Lindh, R. Analytic First-Order Derivatives of (X)MS, XDW, and RMS Variants of the CASPT2 and RASPT2 Methods. *Journal of Chemical Theory and Computation* **2022**, *18*, 4269–4281.

[39] Battaglia, S.; Lindh, R. On the role of symmetry in XDW-CASPT2. *The Journal of Chemical Physics* **2021**, *154*, 034102.

[40] Tange, O. GNU Parallel 20230422 ('Grand Jury') released. 2023; `https://doi.org/10.5281/zenodo.7855617`, DOI: 10.5281/zenodo.7855617.

[41] Gozem, S.; Krylov, A. I. The *ezSpectra* suite: An easy-to-use toolkit for spectroscopy modeling. *WIREs Computational Molecular Science* **2022**, *12*, [Online; accessed 2023-06-24].

[42] Lee, S. Y.; Brown, R. C.; Heller, E. J. Multidimensional reflection approximation: application to the photodissociation of polyatomics. *The Journal of Physical Chemistry* **1983**, *87*, 2045–2053.

[43] Knizia, G.; Klein, J. E. M. N. Electron Flow in Reaction Mechanisms-Revealed from First Principles. *Angewandte Chemie International Edition* **2015**, *54*, 5518–5522.

[44] Tao, Y. PyVibMS: a PyMOL plugin for visualizing vibrations in molecules and solids. *J Mol Model* **2020**,

[45] The PyMOL Molecular Graphics System, Version 2.5.0 Schrödinger, LLC.

[46] Uthman, A. P.; Demlein, P. J.; Allston, T. D.; Withiam, M. C.; McClements, M. J.; Takacs, G. A. Photoabsorption spectra of gaseous methyl bromide, ethylene dibromide, nitrosyl bromide, thionyl chloride, and sulfuryl chloride. *The Journal of Physical Chemistry* **1978**, *82*, 2252–2257.

[47] Bomble, Y. J.; Vázquez, J.; Kállay, M.; Michauk, C.; Szalay, P. G.; Császár, A. G.; Gauss, J.; Stanton, J. F. High-accuracy extrapolated *ab initio* thermochemistry. II. Minor improvements to the protocol and a vital simplification. *The Journal of Chemical Physics* **2006**, *125*, 064108.

[48] Tajti, A.; Szalay, P. G.; Császár, A. G.; Kállay, M.; Gauss, J.; Valeev, E. F.; Flowers, B. A.; Vázquez, J.; Stanton, J. F. HEAT: High accuracy extrapolated *ab initio* thermochemistry. *The Journal of Chemical Physics* **2004**, *121*, 11599–11613.

[49] Harding, M. E.; Vázquez, J.; Ruscic, B.; Wilson, A. K.; Gauss, J.; Stanton, J. F. High-accuracy extrapolated *ab initio* thermochemistry. III. Additional improvements and overview. *The Journal of Chemical Physics* **2008**, *128*, 114111.

[50] Thorpe, J. H.; Lopez, C. A.; Nguyen, T. L.; Baraban, J. H.; Bross, D. H.; Ruscic, B.; Stanton, J. F. High-accuracy extrapolated *ab initio* thermochemistry. IV. A modified recipe for computational efficiency. *The Journal of Chemical Physics* **2019**, *150*, 224102.

[51] Ichino, T.; Gauss, J.; Stanton, J. F. Quasidiabatic states described by coupled-cluster theory. *The Journal of Chemical Physics* **2009**, *130*, 174105.

[52] Norwood, K.; Ng, C. Photoion-photoelectron coincidence spectroscopy of the transient molecules SO and S2O. *Chemical Physics Letters* **1989**, *156*, 145–150.

[53] Radziemski, L. J.; Kaufman, V. Wavelengths, Energy Levels, and Analysis of Neutral Atomic Chlorine (Cl i). *Journal of the Optical Society of America* **1969**, *59*, 424.

[54] Powell, F. X.; Lide, D. R. Microwave Spectrum of the SO Radical. *The Journal of Chemical Physics* **1964**, *41*, 1413–1419.

[55] Politzer, P.; Murray, J. S.; Grice, M. E.; Brinck, T.; Ranganathan, S. Radial behavior of the average local ionization energies of atoms. *The Journal of Chemical Physics* **1991**, *95*, 6699–6704.

[56] Sarka, K.; Nanbu, S. Total Absorption Cross Section for UV Excitation of Sulfur Monoxide. *The Journal of Physical Chemistry A* **2019**, *123*, 3697–3702.

[57] Schurath, U.; Weber, M.; Becker, K. H. Electronic spectrum and structure of the HSO radical. *The Journal of Chemical Physics* **1977**, *67*, 110–119.

[58] Darmanyan, A. P.; Gregory, D. D.; Guo, Y.; Jenks, W. S. Generation and Decay of Aryl Sulfinyl and Sulfenyl Radicals: A Transient Absorption and Computational Study. *The Journal of Physical Chemistry A* **1997**, *101*, 6855–6863.

[59] Weisman, J. L.; Head-Gordon, M. Origin of Substituent Effects in the Absorption Spectra of Peroxy Radicals: Time Dependent Density Functional Theory Calculations. *Journal of the American Chemical Society* **2001**, *123*, 11686–11694.

[60] Yoshikawa, T.; Watanabe, A.; Sumiyoshi, Y.; Endo, Y. Laser spectroscopy of the 2A'–2A" system for the HSO radical. *Journal of Molecular Spectroscopy* **2009**, *254*, 119–125.

Chapter 4

NOVEL DECOMPOSITION MECHANISM FOR SUBSTITUTED CRIEGEE INTERMEDIATES VIA MULTISTRUCTURAL SEMICLASSICAL TRANSITION STATE THEORY

4.1 Introduction

In the past two decades, the reactions of carbonyl oxides, also known as Criegee intermediates (CIs), have become a topic of intense interest in the atmospheric chemistry community. The existence of CIs was postulated as early as the 1950s [1] but were only directly observed in the gas phase in 2008 [2]. CIs are formed in the process of ozonolysis of alkenes. The ozone first adds to the alkene, forming an ozonide. The ozonide quickly decomposes, leaving a carbonyl and carbonyl oxide/CI product. A CI, once formed, can either undergo unimolecular decomposition through a 1,4-hydrogen abstraction to form a vinyl hydroperoxide which can promptly dissociate to OH and a vinoxy radical, or be collisionally quenched to form a stabilized Criegee intermediate.

$$R{-}CH_2{-}CHOO \longrightarrow R{-}CH{=}CHOOH \longrightarrow R{-}CH{=}CHO^{\cdot} + OH$$

Figure 4.1: Traditional decomposition pathway for *syn*-Criegee intermediates.

Unimolecular isomerization to a dioxirane species is also possible, but tends to be slow [3]. Stabilized CIs can also undergo unimolecular decomposition, albeit at a slower rate, or react bimolecularly with a multitude of reaction partners, including water and water dimer [4], SO_2 [5,6], organic acids [7], and other CIs. We direct readers to any of the multiple reviews available on the reactions of Criegee intermediates for a more comprehensive treatment [3,8–10]. While there have been many studies of small and atmospherically relevant CIs [11,12,12], there has been much less focus on CIs derived from oxygenated volatile organic compounds (OVOCs). OVOCs are often emitted in response to plant stress in the form of green leaf volatiles (GLVs) [13]; however, due to the complexities of modeling varying stress factors and species-dependent responses, GLVs as a function of stress are only recently being incorporated into biogenic emissions models such as MEGAN3 [14]. One such compound which has been observed is leaf alcohol (cis 3-hexenol). This compound has been shown to be emitted in significant amounts by both agricultural and native plants [15–18]. In the case of the agricultural plants, 15 of the 20 plants studied had detectable leaf alcohol emissions [15]. Given its high emission rate, the reactions of this compound in the atmosphere are worthy of close study, in particular, its oxidation by OH and ozone. There are product studies of ozonolysis of leaf alcohol looking at long time scale product distributions (on the order of hours); however, the literature is inconsistent on product identities and distributions. For example, while both Grosjean et al. [19] and Chen et al. [20] found high propanal yields relative to

3-hydroxypropanal suggesting preferential formation of the alcohol-substituted CI, only Chen et al.[20] found significant quantities of formaldehyde. The Chen et al.[20] result is exceptionally interesting, as under their mechanism, formaldehyde is only formed through the branch favoring the unsubstituted Criegee, while they observe almost double the amount than what would be predicted by its 1:1 stoichiometric coproduct 3-hydroxypropanal. This indicates that there may be some unrecognized mechanism by which formaldehyde is produced. In this work, we propose a new mechanism for the reaction of the OH-substituted Criegee intermediate, *syn*-3-hydroxypropanal oxide, whereby the CI decomposes via H-abstraction from the OH group, yielding two fragments: formaldehyde and ethylene hydroperoxide. This stands in contrast to the traditional mechanism where the CI undergoes H-abstraction from the vicinal C atom, yielding a 3-carbon vinyl hydroperoxide.

4.2 Theory

Quantum Chemistry

Geometry optimizations, harmonic frequencies, and anharmonic frequencies were calculated with the dispersion-corrected double-hybrid functional B2PLYP-D3(BJ)[21,22] in combination with the def2-TZVPP[23] basis set using Gaussian '16[24]. B2PLYP-D3(BJ) was selected for its excellent performance with geometries, oftentimes yielding better minimum structures than CCSD(T)[25] for triple-zeta basis sets[26]. Single point energies for the lowest energy stationary points were refined with explicitly correlated CCSD(T)-F12[27] in the frozen core approximation and the cc-pVTZ-F12 basis set[28] (and corresponding CABS basis)[29] using the ORCA software package (version 4.2.0)[30,31].

MS-SCTST

As both competing mechanisms outlined in the introduction involve proton transfer, quantitative consideration of tunneling becomes important to determine the relative importance of these channels. While several treatments of tunneling have been proposed, semiclassical transition-state theory (SCTST) has emerged as one of the leading treatments of tunneling. SCTST uses a VPT2 expansion of the potential energy surface combined with a semiclassical expression for the tunneling probability, $P_{\{n^{\ddagger}\}}(E_v)$.

$$k(T) = \frac{1}{h}\frac{Q^{\ddagger'}(T)}{Q^{R}_{anh}(T)}\int_{E_{thresh}}^{\infty}\sum_{\{n^{\ddagger}\}}P_{\{n^{\ddagger}\}}(E_v)\times\exp\left(-\beta E_v\right)dE_v \tag{4.1}$$

While the semiclassical approximation for tunneling is quite robust (and is credited for the success of RPMD in the treatment of reaction rates, it inherits the weaknesses of VPT2, in particular, the poor description of large amplitude motions and hindered rotors. Furthermore, SCTST as presented in the literature is a single conformer theory, accounting for a single reactant and a single transition state. Extending this method to handle multiple conformers in analogy with multiconformer TST is non-obvious. In contrast, the multistructural method with torsional anharmonicity (MS-T) directly includes both multiconformer effects along with torsional anharmonicity. It accomplishes this in a near-black-box manner via an interpolative scaling of the harmonic oscillator partition function between the low temperature, harmonic limit and the high temperature, classical rotor limit. While this temperature-dependent scaling is physically motivated in the canonical picture, it does not have a simple interpretation in the microcanonical picture; however, a microcanonical density of states (DOS) consistent with this scaled partition function is readily obtained via the inverse Laplace transform (ILT):

$$\rho(E) = \frac{1}{2\pi i}\int_{c-i\infty}^{c+i\infty} Q(s)e^{sE}ds \tag{4.2}$$

In this work, we use this derived density of states to correct the VPT2-derived state-counting deficiencies for hindered rotors/torsions. The machinery necessary for the separation of state counting was previously developed[32] in the context of an efficient implementation of SCTST in the Multiwell package . Energy above reactants (products for endothermic reactions) was discretized into energy grains, Wang-Landau sampling was used to determine the approximate number of VPT2 states within each grain and a corresponding average tunneling function for the grain. The final cumulative reaction probability (CRP) $N(E)$ as a function of energy is given by a sum of the averaged tunneling functions, each multiplied by the number of corresponding VPT2 states. In this work we determine the CRP as a function of energy for each transition state conformer separately, with the zero of energy set to the zero-point energy of the lowest energy reactant conformer. The barrier height for the i-th conformer is given by:

$$E_{barrier,i} = E_{TS,0}^{CCSD(T)} + ZPE_{TS,0}^{B2PLYP} + (E_i^{B2PLYP} - E_0^{B2PLYP}) - E_{R,0}^{CCSD(T)} - ZPE_{R,0}^{B2PLYP} \tag{4.3}$$

The average tunneling function for each energy grain is obtained as previously described[32], but is instead scaled by the MS-T DOS (not including external rotations) obtained via the ILT, implemented numerically via second-order steepest descent.

Each conformer CRP was convolved with a conformer-specific classical 1-D rotor, corresponding to an active K-rotor. For details on the algorithm and the necessary derivatives of the partition function, see the SI. The densities of states for the reactant conformers were determined analogously to the transition state conformers, again convolved with a conformer-specific classical K-rotor. The microcanonical rates are given by the RRKM relation[33,34]

$$k_{MS-SCTST}(E) = \frac{1}{h}\frac{N(E)}{\rho_{r,tot}(E)} \tag{4.4}$$

where total CRP is given by the sum of the conformer CRPs, and the total DOS is the sum of the (appropriately energy shifted) reactant DOS. Thermal rates are given by a Boltzmann average of the microcanonical rate

$$k_{MS-SCTST}(T) = \frac{1}{Q_r(T)}\int_{E_{thresh}}^{\infty}\rho_{r,tot}(E)\ k(E)\ e^{-\beta E}dE = \frac{1}{h}\frac{\int_{E_{thresh}}^{\infty} CRP_{tot}(E)\ e^{-\beta E}dE}{\int_0^{\infty}\rho_{r,tot}(E)\ e^{-\beta E}dE} \tag{4.5}$$

4.3 Results

A surface understanding of this reaction can be obtained looking at the lowest energy conformers, as presented in Table 4.1. The total energy for each species is obtained as the sum of the CCSD(T)-F12 electronic energy and the B2PLYP-D3(BJ) anharmonic ZPE. We note that while B2PLYP predicts a 2.5 kcal/mol lower zero-point-exclusive barrier for the OH transition state, the gap is narrowed in the case of CCSD(T) to 1.0 kcal/mol. As expected, the ZPE decrease of the OH transition state is more significant than in the CH transition state, due to the loss of the higher frequency OH stretch. These effects combine to yield an OH pathway with a barrier of 15.2 kcal/mol, and a CH pathway with barrier of 17.3 kcal/mol.

Were these the only two reactive pathways, it is likely that the OH pathway would be significantly favored for thermal reaction; however, in the case of the CH reaction, there are six more transition state conformers that can contribute to the reactive flux. These conformers exist due to the freely rotating CH_2OH group which is not free to rotate in the OH transition state, which only has one conformer. We note that for all structures presented in this work, there are associated mirror image conformers that are accessible via internal rotation. Given the additive nature of the MS-T(C) partition function/density of states, this leads to a doubling of both the density and sum of states in the RRKM expression, allowing us to consider only a single structure in each mirrored pair with no change to the resulting rate. The electronic

Table 4.1: Lowest energy conformers and associated barriers.

	B2PLYP-D3(BJ) Electronic Energy	CCSD(T)-F12 Electronic Energy	B2PLYP-D3(BJ) Anharmonic ZPE	Total
		Lowest Energy Conformers / E_h		
Reactant	-343.340397140	-343.077687949	0.093320471	-342.984367478
OH TS	-343.313809026	-343.046657561	0.086523197	-342.960134364
CH TS	-343.309765147	-343.045054102	0.088186926	-342.956867176
		Lowest Conformer Barriers / (kcal/mol)		
OH	16.7	19.5	-4.3	15.2
CH	19.2	20.5	-3.2	17.3

Table 4.2: Conformer B2PLYP-D3(BJ) electronic energies relative to the lowest energy conformer (kcal/mol).

Reactant Conformers		CH Transition State Conformers	
1	0.00	1	0.00
2	2.01	2	0.51
3	3.30	3	1.24
4	5.08	4	0.18
5	4.16	5	0.35
6	0.31	6	2.63
7	3.52	7	1.58
8	2.27		
9	1.96		
10	4.41		

energies of the other reactant and CH transition state conformers are presented in Table 4.2 (structures available in the SI).

With one exception, the other reactant conformers are significantly (>1 kcal/mol) higher in energy than the lowest energy conformer, due to the loss of the hydrogen bond between the OH group and the carbonyl oxide. Conformer 6 preserves this hydrogen bond, leading to a minimal energy difference. Trends in the CH transition state conformers, however, are not obvious from immediate inspection. These conformer energetics do manifest themselves in the conformer specific CRPs, as pictured in Figure 4.2. As one would expect from their relative energies, transition state conformers 1, 2, 4, and 5 are the main contributors to the CRP. That being said, the other conformers in sum comprise a significant proportion of the CRP at higher energies (up to 15% at 12000 cm^{-1} above the lowest reactant conformer energy). This is more easily seen in Figure 4.3, which compares the microcanonical reaction

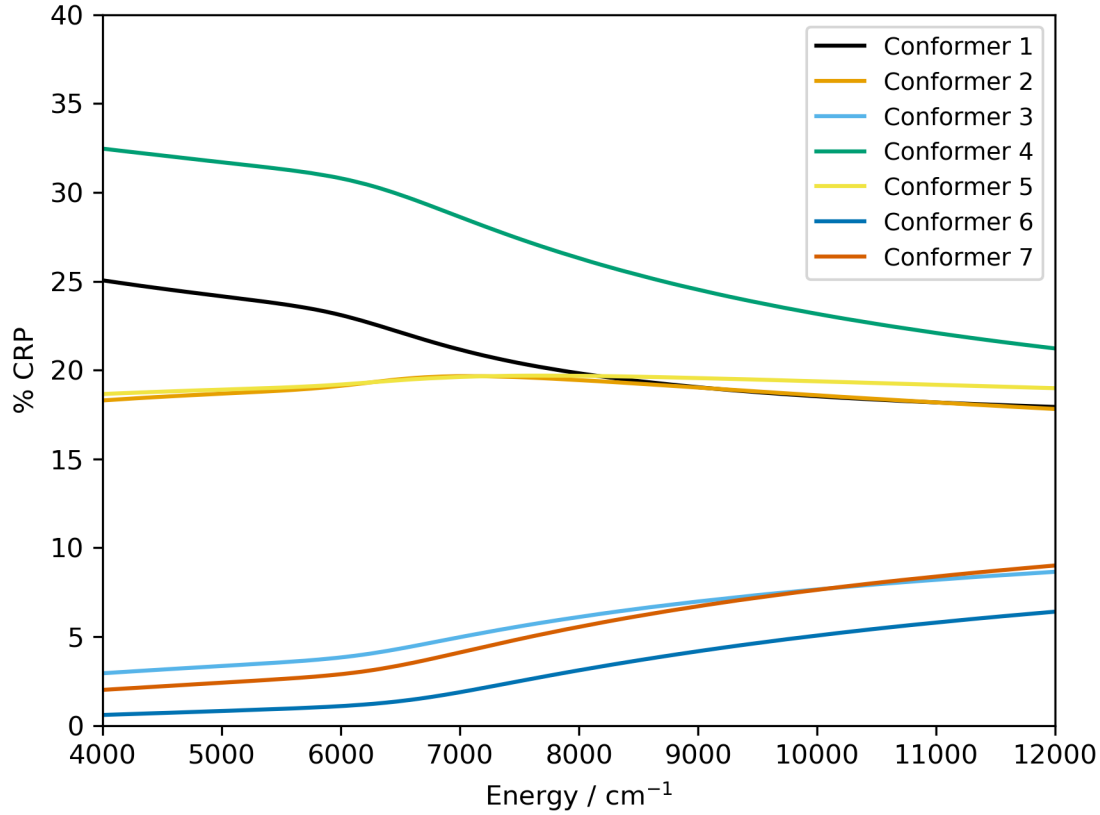

Figure 4.2: Conformer-specific contributions to the MS-SCTST CRP.

rates as a function of energy above the lowest energy reactant conformer using three methods: standard SCTST, considering only the lowest energy conformer for reactant and transition state, the MS-T(C) method, and the newly proposed multistructural SCTST (MS-SCTST). As we can see, near the barrier of $\sim$ 6000 cm^{-1}, SCTST yields higher estimates of the reaction rates for both the OH and CH channels than the other two methods, due to a neglect of the contribution of the various reactant conformers to the reactant partition function. This effect is largely compensated in the CH case, due to simultaneous neglect of higher energy transition state conformers; however, due to the cyclic nature of the OH transition state, there is only a single transition state conformer available, which is fully accounted for in SCTST. Standard SCTST thus leads to an unbalanced description of reactants and products in the OH reaction channel, yielding a significant overestimation of the microcanonical rate. Further insight into the behavior of these methods can be obtained by examining their behavior in the high energy limit. As expected,

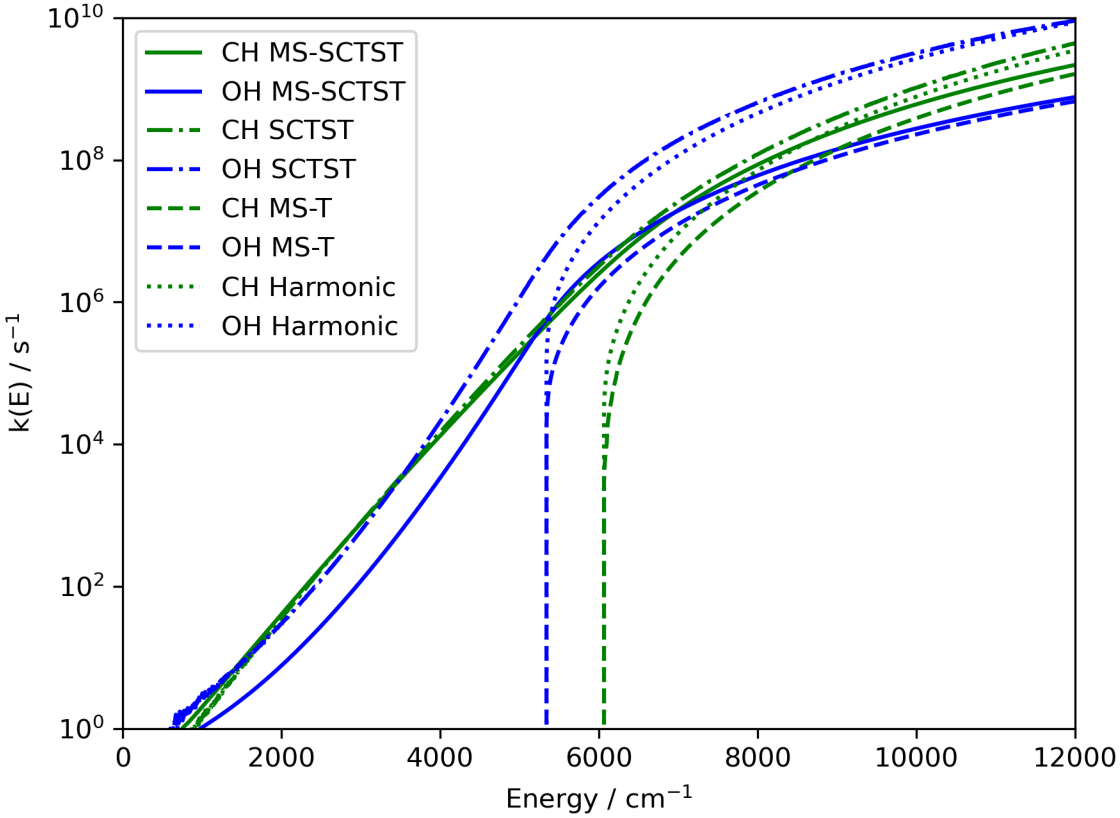

Figure 4.3: Microcanonical rates for MS-SCTST and other approximations.

MS-SCTST appears to approach MS-T(C), as tunneling and non-classical reflection play a decreasingly important role well above the reaction barrier. As such, the rate is controlled solely by the state counting, which is the same for both methods. Although it appears that the standard SCTST approaches the harmonic rate, there is a crossover around 13000 cm^{-1} (Figure 4.7). Figure 4.4 more clearly shows the effects of the consideration of both multiple conformers and tunneling. As the branching fraction is formally independent of the reactant DOS for all methods considered, we can attribute the resultant behavior of the various methods solely to the treatment of the transition state. The importance of considering multiple transition state conformers is highlighted by examination of the harmonic and standard SCTST cases, where the OH abstraction branching fraction is significantly overrepresented by only considering a single reactive CH abstraction conformer. Likewise, while both multiconformer methods show the same high-energy contour, the effect of tunneling on the branching fraction is to create a complex contour at energies

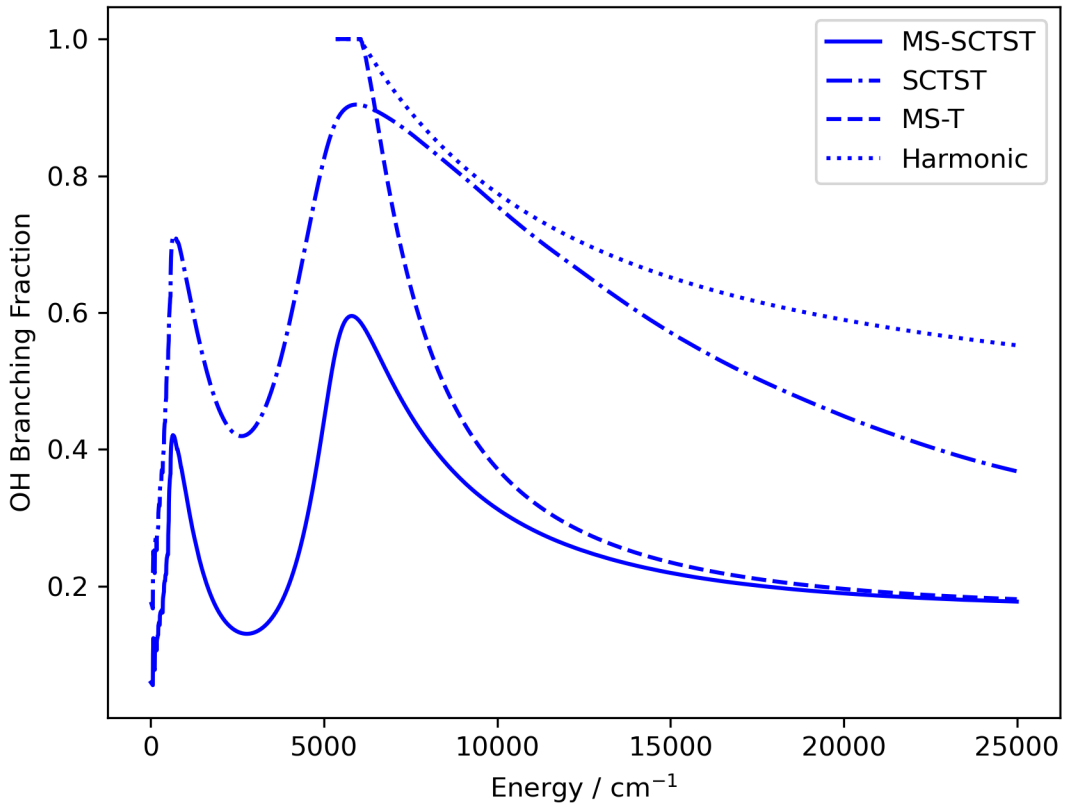

Figure 4.4: OH channel branching fraction as a function of energy.

below and near the classical barrier. As this contour exists for the standard and multistructural variants of SCTST, we attribute this effect solely to the differential tunneling capability of the lowest energy transition state conformers for each channel. This region has practical implications, as a highly simplified model of leaf alcohol ozonolysis based on equipartitioning of energy predicts the formation of a hot Criegee intermediate with approximately 5450 cm^{-1} of excess energy (see SI). This energy lies squarely within the crossover region where the newly proposed OH abstraction channel is favored. While under atmospheric conditions we expect a significant fraction of this reaction to proceed via hot decomposition, it is often easier to measure thermal reaction rates in the laboratory. To this end, we also present thermal decomposition reaction rates in Figure 4.5. Thermal rates for all methods are presented in Figure 4.8 and Table 4.3. At 300 K, we obtain a rate of 130 s^{-1} for the CH abstraction channel and 85 s^{-1} for the OH channel, leading to an estimated lifetime of 4.7 ms, which is readily accessible by common techniques in

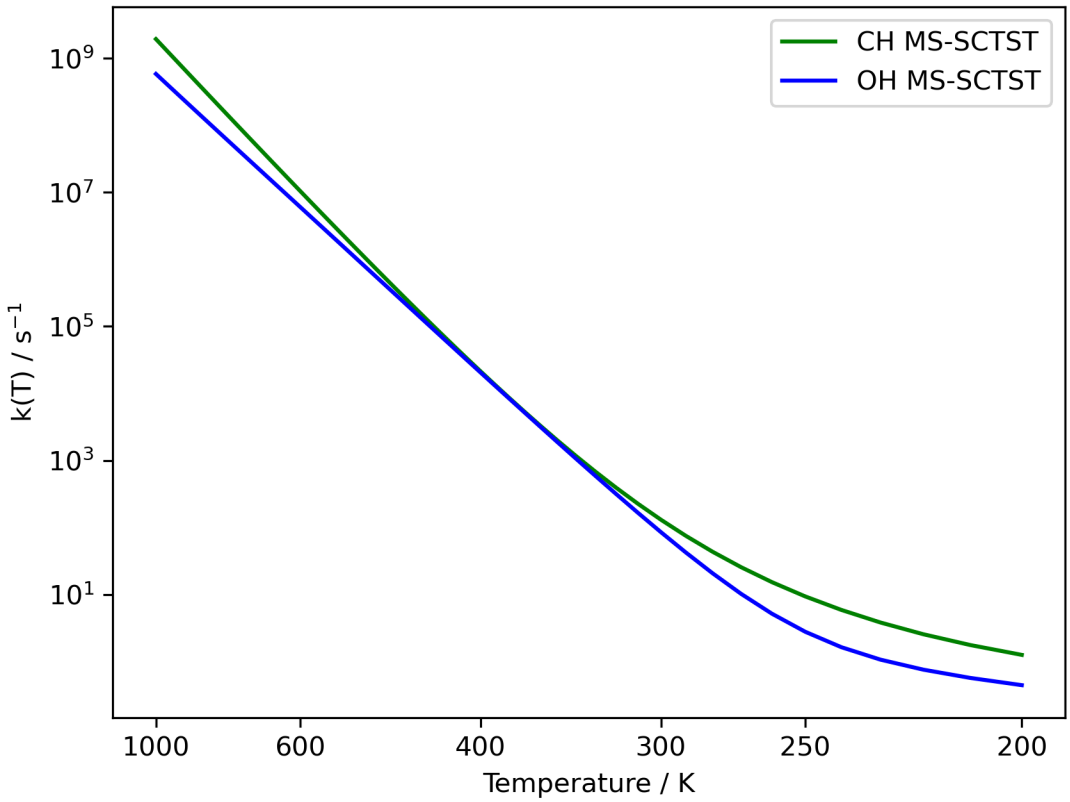

Figure 4.5: MS-SCTST rates for thermal decomposition of *syn*-3-hydroxypropanal oxide.

the field of gas phase kinetics and spectroscopy.

4.4 Conclusions

The decomposition pathways of the Criegee intermediates resulting from the ozonolysis of leaf alcohol have been investigated using quantum chemistry. A new reactive pathway resulting in the generation of formaldehyde was posited, and found to be relevant in the decomposition of both the nascent and thermalized Criegee species. A new method dubbed MS-SCTST was developed for treating tunneling, torsional anharmonicity, and multiconformer effects on equal footing. A balanced description of all of these effects was shown to be necessary for an accurate assessment of the predicted branching fraction.

4.5 Supporting Information

MS-SCTST

The uniformly valid barrier transmission probability $P(E)$ for semiclassical transition state theory is given by

$$P(E) = \left[1 + e^{2\theta(E)}\right]^{-1} \tag{4.6}$$

where $\theta(E)$ is the barrier penetration integral

$$\theta(E) = \frac{1}{\hbar} \int \left[V(q) - E\right]^{1/2} \mathrm{d}q. \tag{4.7}$$

Taking the action relationship from equation 3 of Miller et al.[35]

$$n_F + 1/2 = i\theta/\pi \tag{4.8}$$

combined with the VPT2 expansion for the energy gives a relatively simple expression for the barrier penetration integral as a function of the vibrational quantum numbers of the orthogonal modes $n^{\ddagger}$

$$\theta(n^{\ddagger}, E) = \frac{\pi \Delta E(n^{\ddagger}, E)}{\hbar \Omega_F(n^{\ddagger})} \frac{2}{1 + \left[1 + 4x_{FF}\Delta E(n^{\ddagger}, E)/\left(\hbar\Omega_F(n^{\ddagger})\right)^2\right]^{1/2}} \tag{4.9}$$

where $\Delta E(n^{\ddagger}, E)$, the energy *below* the effective barrier is given by

$$\Delta E(n^{\ddagger}, E) = \Delta V_f + G_0 + E_{vib,orth}(n^{\ddagger}) - E, \tag{4.10}$$

the energy in orthogonal TS modes $E_{vib,orth}$ by

$$E_{vib,orth}(n^{\ddagger}) = \sum_{j=1}^{F-1} \hbar\omega_j(n_j + 1/2) + \sum_{j=1}^{F-1}\sum_{k=j}^{F-1} x_{jk}(n_j + 1/2)(n_k + 1/2) \tag{4.11}$$

and the effective frequency of the reactive mode $\Omega_F(n^{\ddagger})$ is given by

$$\Omega_F(n^{\ddagger}) = \omega_F + \sum_{k=1}^{F-1} x_{kF}(n_k + 1/2). \tag{4.12}$$

The cumulative reaction probability $N(E)$ is given by the sum of the tunneling function over all values of the orthogonal vibrational quantum numbers.

$$N(E) = \sum_{\{n^{\ddagger}\}} P(n^{\ddagger}, E) = \sum_{\{n^{\ddagger}\}} \left[1 + e^{2\theta(n^{\ddagger}, E)}\right]^{-1} \tag{4.13}$$

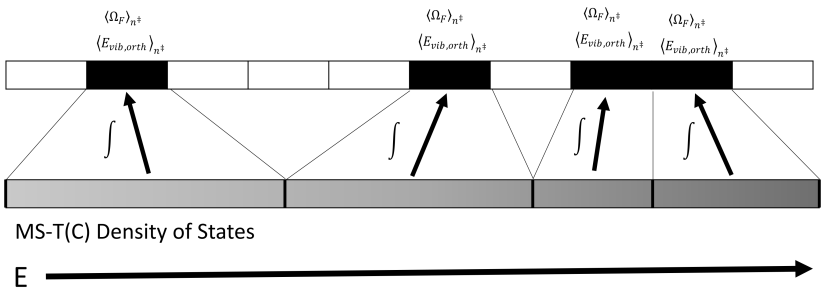

Figure 4.6: Assignment of MS-T(C) states to energy bins for the scaling of tunneling functions.

In the Multiwell implementation of the Wang-Landau adaptation of SCTST by Nguyen et al.[32], the energy is discretized into bins of width ΔE_{bin}. The average energy in orthogonal TS modes $\langle E_{vib,orth}\rangle_{n^\ddagger}$ and average effective frequency of the reactive mode $\langle \Omega_F \rangle_{n^\ddagger}$ for each energy bin is sampled by the Wang-Landau procedure. An average tunneling profile is determined for each bin based on its averaged values, and scaled by the number of VPT2 states in the bin to yield a total tunneling contribution of the quantum states in the bin.

$$P_{bin}(E) = P(E, \langle E_{vib,orth}\rangle_{n^\ddagger}, \langle \Omega_F \rangle_{n^\ddagger}) * \left(\rho_{Wang-Landau}(E) \times \Delta E_{bin}\right) \qquad (4.14)$$

Unique to Multiwell is the restriction $E \geq E_{vib,orth}$ for each $P_{bin}(E)$, which corresponds to the physical restriction that the energy in the imaginary mode F is positive.

The new MS-SCTST simply replaces the scaling factor in equation 4.14. The number of VPT2 states in each bin is replaced by the number of MS-T(C) states assigned to the bin. MS-T(C) states are assigned to the nearest energy bin which has VPT2 states (and thus an associated tunneling profile), as shown schematically in Figure 4.6. As VPT2 and SCTST count from the anharmonic zero of energy, and MS-T(C) counts from the harmonic zero of energy, we shift the MS-T(C) density of states such that the harmonic zero is equal to the anharmonic zero.

We make one additional approximation in this work compared to the full MS-SCTST method outlined above: we assume that the VPT2-derived tunneling profiles are approximately the same for the various conformers. In other words, the average tunneling profiles for each bin are only calculated for the lowest energy transition state conformer and subsequently used for other transition state conformers, replacing the barrier height with a conformer specific barrier height (obtained from the anharmonic barrier height of the lowest conformer + the difference in electronic

energy) and scaling by the conformer-specific MS-T(C) density of states. This approximation is justified by an approximate separability of the reactive region and the torsional region, but deserves further investigation.

Inverse Laplace Transform

Steepest Descents Approximation

In order to evaluate equation 4.2 from the main text, we use the method of second-order steepest descents as derived by Forst[36]. We briefly summarize here, and encourage the interested reader to consult the original text[36] for more details. The inverse Laplace transform for the density of states and sum of states is given by

$$I(E,k) = \frac{1}{2\pi i}\int_{c-i\infty}^{c+i\infty} \frac{Q(s)\exp(sE)\mathrm{d}s}{s^k} \tag{4.15}$$

where the density of states corresponds to $k = 0$ and the sum of states corresponds to $k = 1$. We define the function $\phi(s)$

$$\phi(s) = \ln Q(s) - k\ln(s) + sE \tag{4.16}$$

such that equation 4.15 becomes

$$I(E,k) = \frac{1}{2\pi}\int_{-\infty}^{\infty} \exp(\phi(x^* + iy))\mathrm{d}y \tag{4.17}$$

where x^* corresponds to the solution of

$$\phi'(x) = \frac{\partial \ln Q(x)}{\partial x} - \frac{k}{x} + E = 0 \tag{4.18}$$

along the real line. The second order steepest-descents approximation of this integral is given by

$$I_2(E,k) = \frac{Q(x^*)\exp(x^*E)}{(x^*)^k(2\pi\phi''(x^*))^{1/2}} \times \left(1 + \frac{1}{8}\frac{\phi^{(4)}(x^*)}{(\phi''(x^*))^2} - \frac{5}{24}\frac{(\phi^{(3)}(x^*))^2}{(\phi''(x^*))^3}\right) \tag{4.19}$$

and requires up through the fourth derivative of the natural logarithm of the partition function. The formulas for the derivatives beyond first order are new in this work, and are given in the following section.

Derivatives of the MS-T(C) Partition Function

The MS-T(C) partition function for a single conformer j is given by

$$Q_{con-vib,j}^{SS-T} = e^{-\beta U_j} Q_j^{HO} \prod_{\eta=1}^{t} f_{j,\eta} \tag{4.20}$$

where η indexes torsions and $f_{j,\eta}$ is given by

$$\prod_{\eta=1}^{t} f_{j,\eta} = (2\pi\beta)^{t/2} \frac{\prod_{m=1}^{F} \omega_{j,m}}{\prod_{\bar{m}=1}^{F-t} \overline{\omega}_{j,\bar{m}}} \frac{\sqrt{\det \mathbf{D}_j}}{\prod_{\tau=1}^{t} M_{j,\tau}} \prod_{\eta=1}^{t} e^{-\beta W_{j,\eta}^{(C)}/2} I_0(\beta W_{j,\eta}^{(C)}/2) \tag{4.21}$$

The derivatives are as follows:

$$\begin{aligned} \frac{-\partial \ln Q_{con-vib,j}^{SS-T}}{\partial \beta} &= \frac{1}{Q_{con-vib,j}^{SS-T}} \frac{-\partial Q_{con-vib,j}^{SS-T}}{\partial \beta} \\ &= U_j + \sum_{m=1}^{F} \frac{\hbar\omega_{j,m}}{2} \left(\frac{1 + e^{-\beta\hbar\omega_{j,m}}}{1 - e^{-\beta\hbar\omega_{j,m}}} \right) + \sum_{\eta=1}^{t} \left[\frac{W_{j,\eta}^{(C)}}{2} \left(1 - \frac{I_1(\beta W_{j,\eta}^{(C)}/2)}{I_0(\beta W_{j,\eta}^{(C)}/2)} \right) - \frac{1}{2\beta} \right] \end{aligned} \tag{4.22}$$

$$\begin{aligned} \frac{-\partial^2 \ln Q_{con-vib,j}^{SS-T}}{\partial \beta^2} &= -\sum_{m=1}^{F} \left[\frac{(\hbar\omega_{j,m})^2 e^{-\beta\hbar\omega_{j,m}}}{(e^{-\beta\hbar\omega_{j,m}} - 1)^2} \right] \\ &\quad + \sum_{\eta=1}^{t} \left[\frac{1}{2\beta^2} + \frac{W_{j,\eta}^2}{4} \left(\frac{I_1^2(\beta W_{j,\eta}^{(C)}/2)}{I_0^2(\beta W_{j,\eta}^{(C)}/2)} + \frac{2}{\beta W_{j,\eta}} \frac{I_1(\beta W_{j,\eta}^{(C)}/2)}{I_0(\beta W_{j,\eta}^{(C)}/2)} - \right) \right] \end{aligned} \tag{4.23}$$

Simplifying notation with $W_{j,\eta} = W_{j,\eta}^{(C)}$, $I_0 = I_0(\beta W_{j,\eta}/2)$, and $I_1 = I_1(\beta W_{j,\eta}/2)$:

$$\begin{aligned} \frac{-\partial^3 \ln Q_{con-vib,j}^{SS-T}}{\partial \beta^3} &= \sum_{m=1}^{F} \left[\frac{(\hbar\omega_{j,m})^3 e^{-\beta\hbar\omega_{j,m}} (1 + e^{-\beta\hbar\omega_{j,m}})}{(e^{-\beta hbar\omega_{j,m}} - 1)^3} \right] \\ &\quad + \sum_{\eta=1}^{t} \left[\frac{W_{j,\eta}((\beta^2 W_{j,\eta}^2 - 4) I_1 I_0^2 - \beta^2 W_{j,\eta}^2 I_1^3 + \beta W_{j,\eta} I_0^3 - 3\beta W_{j,\eta} I_1^2 I_0)}{4\beta^2 I_0^3} - \frac{1}{\beta^3} \right] \end{aligned} \tag{4.24}$$

$$\begin{aligned} \frac{-\partial^4 \ln Q_{con-vib,j}^{SS-T}}{\partial \beta^4} &= -\sum_{m=1}^{F} \left[\frac{(\hbar\omega_{j,m})^4 e^{-\beta\hbar\omega_{j,m}} (1 + 4e^{-\beta\hbar\omega_{j,m}} + e^{-2\beta\hbar\omega_{j,m}})}{(e^{-\beta\hbar\omega_{j,m}} - 1)^4} \right] \\ &\quad + \sum_{\eta=1}^{t} \left[\frac{3}{\beta^4} + \frac{W_{j,\eta}}{8\beta^3 I_0^4} \left(3\beta^3 W_{j,\eta}^3 I_1^4 + \beta W_{j,\eta} (\beta^2 W_{j,\eta}^2 - 6) I_0^4 - 8(\beta^2 W_{j,\eta}^2 - 3) I_1 I_0^3 \right. \right. \\ &\quad \left. \left. + 2\beta W_{j,\eta} (11 - 2\beta^2 W_{j,\eta}^2) I_1^2 I_0^2 + 12\beta^2 W_{j,\eta}^2 I_1^3 I_0 \right) \right] \end{aligned} \tag{4.25}$$

Conformer Coordinates

Reactant Conformers

```
12
Conformer 01
C   -1.637890    0.117001    0.036848
H   -2.160750    0.599840   -0.789404
H   -2.342798    0.028200    0.869086
C   -0.476311    1.020166    0.513252
H   -0.116263    0.659037    1.478394
H   -0.829114    2.046469    0.600655
C    0.672730    0.974276   -0.405115
H    0.892558    1.710898   -1.166931
O    1.541144    0.055178   -0.361078
O    1.361461   -0.958382    0.543322
O   -1.203376   -1.138940   -0.421902
H   -0.388636   -1.375948    0.055566

12
Conformer 02
C   -1.261267   -0.633051    0.246795
H   -1.881261   -1.131830    0.994786
H   -0.678699   -1.380937   -0.288460
C   -0.313540    0.331223    0.959465
H    0.278381   -0.239760    1.677814
H   -0.892939    1.101604    1.463308
C    0.621389    0.958830    0.010378
H    0.546879    1.968746   -0.365759
O    1.616200    0.330895   -0.467568
O    1.803974   -0.956220   -0.087121
O   -2.058549    0.148231   -0.640687
H   -2.544848   -0.443088   -1.218504

12
Conformer 03
C   -1.252365   -0.651825    0.184665
```

```
H   -1.824667   -1.231688    0.910739
H   -0.660782   -1.338662   -0.411593
C   -0.310194    0.301989    0.942511
H    0.281429   -0.291858    1.643684
H   -0.889951    1.052317    1.478239
C    0.629875    0.963119    0.024595
H    0.551671    1.978004   -0.337096
O    1.639770    0.352752   -0.447936
O    1.831686   -0.937159   -0.085944
O   -2.105071    0.042843   -0.714060
H   -2.792677    0.484700   -0.211081

12
Conformer 04
C   -1.235857   -0.106104   -0.495797
H   -0.751794   -1.041559   -0.754653
H   -1.386159    0.477139   -1.407442
C   -0.329275    0.670861    0.483726
H   -0.185325    0.035605    1.360184
H   -0.808662    1.606438    0.769740
C    0.995361    0.961157   -0.084052
H    1.327649    1.924566   -0.444400
O    1.893047    0.065724   -0.204075
O    1.605103   -1.187535    0.201447
O   -2.471243   -0.442405    0.107015
H   -2.992332    0.356059    0.218221

12
Conformer 05
C   -1.229569   -0.100207   -0.490695
H   -0.761234   -1.057335   -0.713172
H   -1.363649    0.459262   -1.420591
C   -0.328109    0.687214    0.465229
H   -0.192961    0.076969    1.361264
H   -0.811751    1.627463    0.721070
C    1.005029    0.953132   -0.096353
```

```
H    1.355899    1.912177   -0.450754
O    1.893845    0.047924   -0.198663
O    1.586623   -1.201826    0.206279
O   -2.471214   -0.262548    0.181647
H   -2.984445   -0.927761   -0.281007

12
Conformer 06
C    1.503440   -0.360596   -0.301907
H    1.374386   -0.550189   -1.373596
H    2.438791   -0.828154    0.001928
C    0.358161   -1.060699    0.482127
H    0.304176   -0.581834    1.464076
H    0.591882   -2.116466    0.604725
C   -0.970629   -0.969695   -0.146277
H   -1.497851   -1.816679   -0.566533
O   -1.647687    0.094838   -0.246088
O   -1.114801    1.260541    0.219693
O    1.605925    1.005944   -0.018141
H    0.695287    1.348676    0.022022

12
Conformer 07
C   -1.244677    0.044837    0.524468
H   -1.503397    0.764926    1.296995
H   -0.729970   -0.797500    0.983584
C   -0.309393    0.708282   -0.512493
H   -0.751307    1.636116   -0.866775
H   -0.184528    0.004706   -1.339415
C    1.028787    0.954648    0.038822
H    1.419571    1.912344    0.352955
O    1.869140    0.011655    0.201233
O    1.497895   -1.240345   -0.148175
O   -2.465782   -0.348694   -0.072034
H   -2.308694   -1.148125   -0.580313
```

```
12
Conformer 08
C   -1.717455    0.507929   -0.345528
H   -1.868988    0.272886   -1.397436
H   -2.230325    1.449766   -0.143030
C   -0.235313    0.653637   -0.042363
H   -0.050458    0.938259    1.000635
H    0.232455    1.462330   -0.615181
C    0.517060   -0.580425   -0.303212
H    0.086309   -1.511008   -0.644371
O    1.771980   -0.636113   -0.119825
O    2.383382    0.485306    0.327686
O   -2.309090   -0.568442    0.372129
H   -2.324928   -0.345096    1.306081

12
Conformer 09
C   -1.701974    0.532947   -0.331676
H   -1.827401    0.337156   -1.400707
H   -2.202808    1.474950   -0.100597
C   -0.232179    0.647824    0.009945
H   -0.085058    0.902799    1.064808
H    0.260424    1.458450   -0.535794
C    0.510394   -0.590617   -0.258974
H    0.067674   -1.527379   -0.565192
O    1.771474   -0.642468   -0.126327
O    2.400809    0.485136    0.280634
O   -2.234994   -0.536819    0.442851
H   -3.168593   -0.633684    0.244447

12
Conformer 10
C   -1.661894    0.477058    0.036388
H   -1.795370    1.172766   -0.790296
H   -1.758601    1.046772    0.965728
C   -0.288710   -0.175606   -0.039568
```

```
H   -0.184044   -0.781118   -0.946521
H   -0.119588   -0.890684    0.774744
C    0.815712    0.789904   -0.003473
H    0.714488    1.866766    0.010698
O    2.027965    0.406112    0.016665
O    2.257719   -0.922969   -0.002185
O   -2.708150   -0.468718   -0.092379
H   -2.667807   -1.078035    0.648759
```

Transition State Conformers

```
12
Conformer 1
C   -1.691322   -0.523454   -0.284148
H   -2.087831   -1.478903    0.066212
H   -2.097102   -0.352359   -1.280961
C   -0.181863   -0.586030   -0.304262
H    0.236442   -1.455745   -0.812427
H    0.737464   -0.858896    0.629905
C    0.518174    0.614373   -0.509071
H    0.124611    1.582885   -0.787301
O    1.740509    0.662472   -0.074402
O    2.075427   -0.580259    0.490030
O   -2.176854    0.557633    0.504045
H   -1.896170    0.414917    1.412072

12
Conformer 2
C   -1.668967    0.605423    0.189789
H   -1.997090    1.486664   -0.366685
H   -2.103761    0.666322    1.192876
C   -0.165204    0.600203    0.259231
H    0.260743    1.433899    0.817152
H    0.794431    0.878742   -0.625853
C    0.486748   -0.629085    0.438444
H    0.051687   -1.596866    0.642638
```

```
O     1.730043   -0.689782    0.066714
O     2.122442    0.568712   -0.421196
O    -2.087007   -0.594113   -0.456748
H    -3.045295   -0.606543   -0.495061

12
Conformer 3
C    -1.594794   -0.190966    0.561556
H    -1.628492    0.617534    1.299525
H    -1.871487   -1.106789    1.078247
C    -0.202391   -0.327203    0.000627
H    -0.149840   -0.937430   -0.902308
H     0.856030   -1.021386    0.379670
C     0.638318    0.798586    0.019106
H     0.391014    1.821044    0.277452
O     1.916929    0.582144   -0.023916
O     2.143493   -0.797918   -0.122447
O    -2.594068   -0.012007   -0.436924
H    -2.374854    0.766772   -0.954025

12
Conformer 4
C    -1.586565   -0.384223    0.488004
H    -1.618708    0.143629    1.445651
H    -1.914722   -1.410618    0.665452
C    -0.186106   -0.402176   -0.048624
H    -0.085122   -0.909130   -1.008815
H     0.927045   -1.059688    0.282391
C     0.577263    0.768462    0.075905
H     0.257242    1.753399    0.390921
O     1.867109    0.635865    0.036914
O     2.182428   -0.720622   -0.155966
O    -2.431210    0.258097   -0.468990
H    -3.339915    0.203317   -0.162972

12
```

Conformer 5

C	-1.595618	-0.518733	0.404891
H	-1.643700	-0.272093	1.462635
H	-2.000935	-1.522582	0.286377
C	-0.166771	-0.489784	-0.086881
H	0.019494	-1.038150	-1.006910
H	0.955646	-1.051752	0.317357
C	0.512805	0.734264	0.054595
H	0.112067	1.696991	0.353653
O	1.816988	0.678212	0.085012
O	2.208248	-0.648173	-0.154462
O	-2.438501	0.436039	-0.245946
H	-2.638951	0.104479	-1.125576

12

Conformer 6

C	1.628235	0.512173	0.046442
H	2.015318	1.071844	0.903712
H	1.652489	1.171574	-0.825901
C	0.222334	0.044849	0.306837
H	0.109453	-0.541511	1.219907
H	-0.507799	-0.926304	-0.233457
C	-0.853688	0.892728	0.019085
H	-0.842691	1.935557	-0.271011
O	-2.011667	0.330101	-0.161911
O	-1.872565	-1.056512	-0.003762
O	2.416527	-0.651680	-0.178517
H	3.333584	-0.384932	-0.273912

12

Conformer 7

C	1.662520	0.532508	0.060603
H	2.104369	1.010950	0.930586
H	1.737231	1.235054	-0.775295
C	0.232288	0.144477	0.308942
H	0.071467	-0.326812	1.281440

```
H    -0.457734    -0.912364    -0.117946
C    -0.863990     0.920532    -0.052651
H    -0.921082     1.940820    -0.401342
O    -2.004020     0.298469    -0.148601
O    -1.810868    -1.092649     0.032063
O     2.479699    -0.613429    -0.157203
H     1.962348    -1.271883    -0.628883
```

Additional Figures

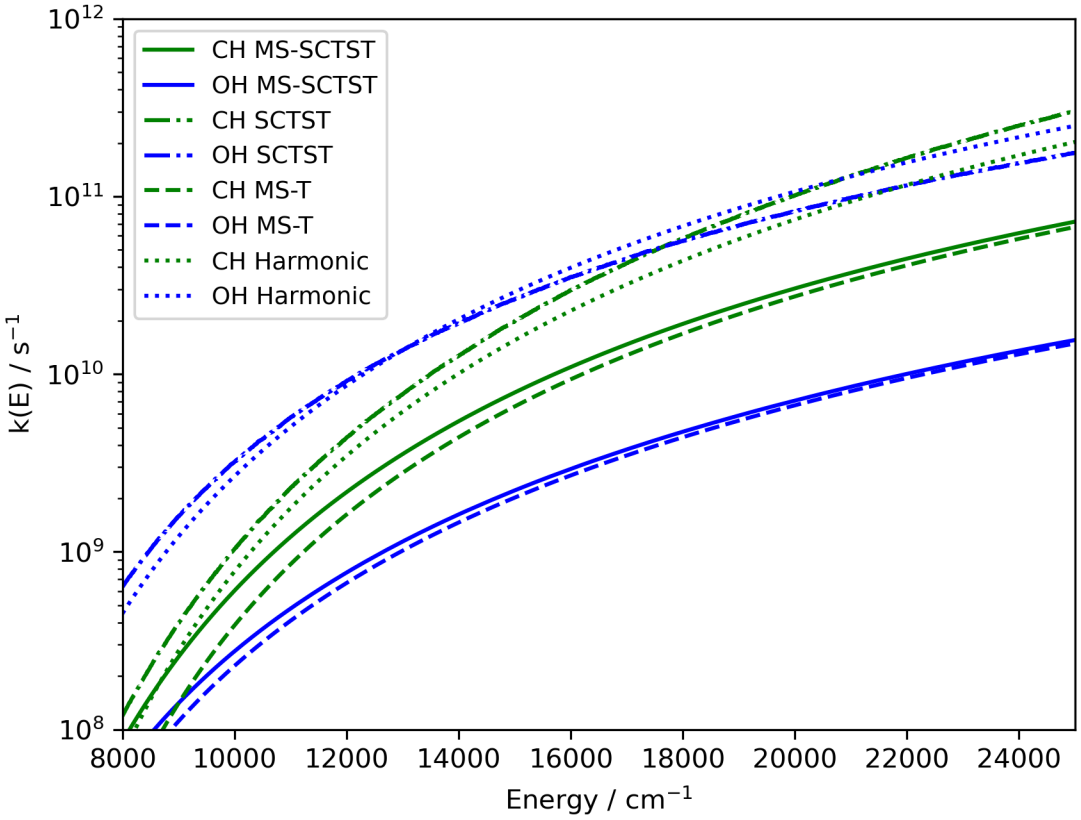

Figure 4.7: Microcanonical decomposition rates of *syn*-3-hydroxypropanal oxide from 8000 cm^{-1} to 25000 cm^{-1}.

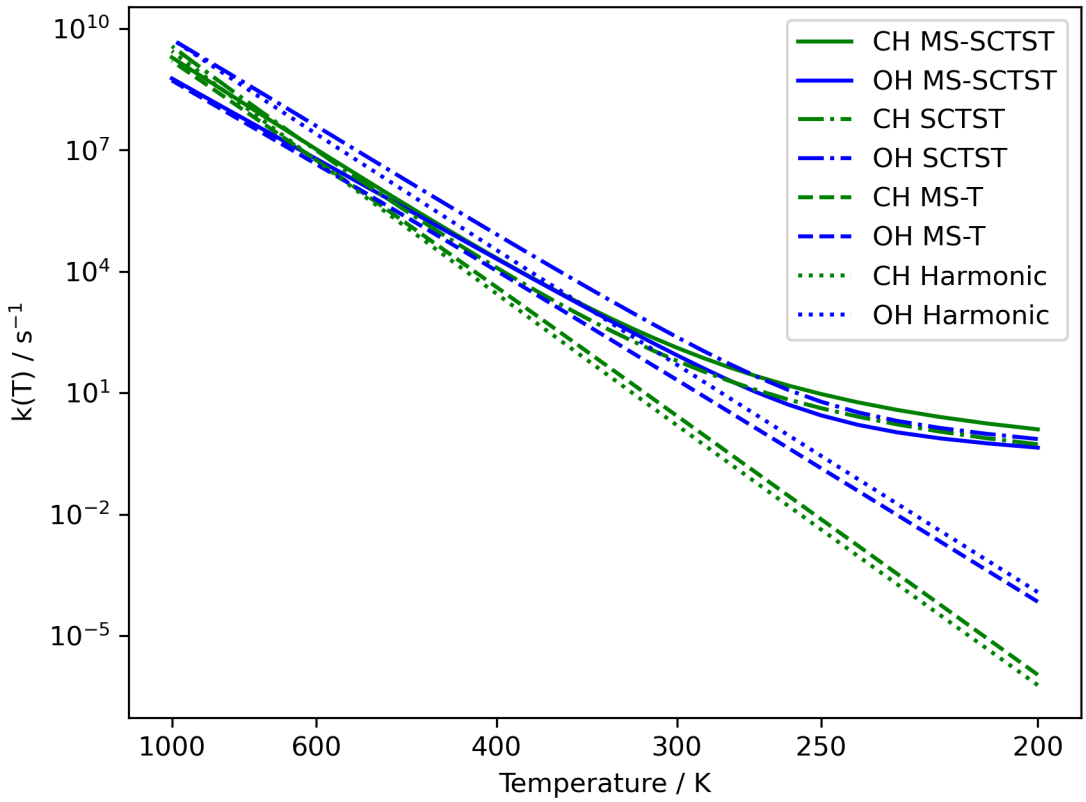

Figure 4.8: Thermal decomposition rates of *syn*-3-hydroxypropanal oxide from 200K to 1000K.

Tables

Table 4.3: Thermal decomposition rates of *syn*-3-hydroxypropanal oxide from 200K to 1000K.

Temperature (K)	CH MS-SCTST (s^{-1})	OH MS-SCTST (s^{-1})
200	1.25E+00	4.43E-01
210	1.76E+00	5.68E-01
220	2.55E+00	7.54E-01
230	3.81E+00	1.06E+00
240	5.87E+00	1.63E+00
250	9.34E+00	2.77E+00
260	1.52E+01	5.15E+00
270	2.55E+01	1.02E+01

T	CH MS-SCTST	OH MS-SCTST
280	4.34E+01	2.07E+01
290	7.49E+01	4.23E+01
300	1.30E+02	8.49E+01
310	2.27E+02	1.66E+02
320	3.94E+02	3.17E+02
330	6.80E+02	5.88E+02
340	1.16E+03	1.06E+03
350	1.96E+03	1.85E+03
360	3.26E+03	3.14E+03
370	5.34E+03	5.19E+03
380	8.61E+03	8.39E+03
390	1.37E+04	1.32E+04
400	2.13E+04	2.05E+04
410	3.28E+04	3.10E+04
420	4.96E+04	4.60E+04
430	7.38E+04	6.71E+04
440	1.08E+05	9.62E+04
450	1.57E+05	1.36E+05
460	2.24E+05	1.89E+05
470	3.15E+05	2.59E+05
480	4.39E+05	3.51E+05
490	6.03E+05	4.69E+05
500	8.20E+05	6.20E+05
510	1.10E+06	8.11E+05
520	1.47E+06	1.05E+06
530	1.93E+06	1.34E+06
540	2.52E+06	1.71E+06
550	3.26E+06	2.15E+06
560	4.18E+06	2.68E+06
570	5.32E+06	3.32E+06
580	6.72E+06	4.09E+06
590	8.41E+06	4.99E+06
600	1.05E+07	6.05E+06
610	1.29E+07	7.29E+06
620	1.59E+07	8.73E+06

T	CH MS-SCTST	OH MS-SCTST
630	1.93E+07	1.04E+07
640	2.34E+07	1.23E+07
650	2.83E+07	1.45E+07
660	3.39E+07	1.70E+07
670	4.04E+07	1.99E+07
680	4.79E+07	2.31E+07
690	5.66E+07	2.67E+07
700	6.66E+07	3.08E+07
710	7.79E+07	3.53E+07
720	9.08E+07	4.04E+07
730	1.05E+08	4.60E+07
740	1.22E+08	5.22E+07
750	1.40E+08	5.90E+07
760	1.61E+08	6.66E+07
770	1.84E+08	7.48E+07
780	2.10E+08	8.39E+07
790	2.38E+08	9.37E+07
800	2.70E+08	1.04E+08
810	3.05E+08	1.16E+08
820	3.43E+08	1.29E+08
830	3.85E+08	1.42E+08
840	4.31E+08	1.57E+08
850	4.82E+08	1.73E+08
860	5.37E+08	1.90E+08
870	5.96E+08	2.09E+08
880	6.61E+08	2.28E+08
890	7.31E+08	2.49E+08
900	8.07E+08	2.72E+08
910	8.89E+08	2.96E+08
920	9.77E+08	3.21E+08
930	1.07E+09	3.48E+08
940	1.17E+09	3.77E+08
950	1.28E+09	4.07E+08
960	1.40E+09	4.39E+08
970	1.52E+09	4.73E+08

T	CH MS-SCTST	OH MS-SCTST
980	1.65E+09	5.09E+08
990	1.79E+09	5.46E+08
1000	1.94E+09	5.86E+08

References

[1] Criegee, R. New York, 1951.

[2] Taatjes, C. A.; Meloni, G.; Selby, T. M.; Trevitt, A. J.; Osborn, D. L.; Percival, C. J.; Shallcross, D. E. Direct Observation of the Gas-Phase Criegee Intermediate (CH2OO). *Journal of the American Chemical Society* **2008**, *130*, 11883–11885.

[3] Taatjes, C. A. Criegee Intermediates: What Direct Production and Detection Can Teach Us About Reactions of Carbonyl Oxides. *Annual Review of Physical Chemistry* **2017**, *68*, 183–207, _eprint: https://doi.org/10.1146/annurev-physchem-052516-050739.

[4] Chao, W.; Hsieh, J.-T.; Chang, C.-H.; Lin, J. J.-M. Direct kinetic measurement of the reaction of the simplest Criegee intermediate with water vapor. *Science* **2015**, *347*, 751–754, Publisher: American Association for the Advancement of Science.

[5] Huang, H.-L.; Chao, W.; Lin, J. J.-M. Kinetics of a Criegee intermediate that would survive high humidity and may oxidize atmospheric SO2. *Proceedings of the National Academy of Sciences* **2015**, *112*, 10857–10862.

[6] Chhantyal-Pun, R.; Davey, A.; Shallcross, D. E.; Percival, C. J.; Orr-Ewing, A. J. A kinetic study of the CH2OO Criegee intermediate self-reaction, reaction with SO2 and unimolecular reaction using cavity ring-down spectroscopy. *Physical Chemistry Chemical Physics* **2015**, *17*, 3617–3626, Publisher: The Royal Society of Chemistry.

[7] Welz, O.; Eskola, A. J.; Sheps, L.; Rotavera, B.; Savee, J. D.; Scheer, A. M.; Osborn, D. L.; Lowe, D.; Murray Booth, A.; Xiao, P.; Anwar H. Khan, M.; Percival, C. J.; Shallcross, D. E.; Taatjes, C. A. Rate Coefficients of C1 and C2 Criegee Intermediate Reactions with Formic and Acetic Acid Near the Collision Limit: Direct Kinetics Measurements and Atmospheric Implications. *Angewandte Chemie International Edition* **2014**, *53*, 4547–4550, _eprint: https://onlinelibrary.wiley.com/doi/pdf/10.1002/anie.201400964.

[8] Osborn, D. L.; Taatjes, C. A. The physical chemistry of Criegee intermediates in the gas phase. *International Reviews in Physical Chemistry* **2015**, *34*, 309–360, Publisher: Taylor & Francis _eprint: https://doi.org/10.1080/0144235X.2015.1055676.

[9] Lee, Y.-P. Perspective: Spectroscopy and kinetics of small gaseous Criegee intermediates. *The Journal of Chemical Physics* **2015**, *143*, 020901.

[10] Taatjes, C. A.; Shallcross, D. E.; Percival, C. J. Research frontiers in the chemistry of Criegee intermediates and tropospheric ozonolysis. *Physical Chemistry Chemical Physics* **2014**, *16*, 1704–1718, Publisher: The Royal Society of Chemistry.

[11] Welz, O.; Savee, J. D.; Osborn, D. L.; Vasu, S. S.; Percival, C. J.; Shallcross, D. E.; Taatjes, C. A. Direct Kinetic Measurements of Criegee Intermediate (CH2OO) Formed by Reaction of CH2I with O2. *Science* **2012**, *335*, 204–207.

[12] Caravan, R. L. et al. Direct kinetic measurements and theoretical predictions of an isoprene-derived Criegee intermediate. *Proceedings of the National Academy of Sciences* **2020**, *117*, 9733–9740, Publisher: Proceedings of the National Academy of Sciences.

[13] Faiola, C.; Taipale, D. Impact of insect herbivory on plant stress volatile emissions from trees: A synthesis of quantitative measurements and recommendations for future research. *Atmospheric Environment: X* **2020**, *5*, 100060.

[14] Jiang, X.; Guenther, A.; Potosnak, M.; Geron, C.; Seco, R.; Karl, T.; Kim, S.; Gu, L.; Pallardy, S. Isoprene emission response to drought and the impact on global atmospheric chemistry. *Atmospheric Environment* **2018**, *183*, 69–83.

[15] Arey, J.; Winer, A. M.; Atkinson, R.; Aschmann, S. M.; Long, W. D.; Lynn Morrison, C. The emission of (Z)-3-hexen-1-ol, (Z)-3-hexenylacetate and other oxygenated hydrocarbons from agricultural plant species. *Atmospheric Environment. Part A. General Topics* **1991**, *25*, 1063–1075.

[16] Isidorov, V. A.; Zenkevich, I. G.; Ioffe, B. V. Volatile organic compounds in the atmosphere of forests. *Atmospheric Environment (1967)* **1985**, *19*, 1–8.

[17] Ohta, K. Emission of hexenol from higher plants. *GEOCHEMICAL JOURNAL* **1984**, *18*, 135–141.

[18] Winer, A. M.; Arey, J.; Atkinson, R.; Aschmann, S. M.; Long, W. D.; Morrison, C. L.; Olszyk, D. M. Emission rates of organics from vegetation in California's Central Valley. *Atmospheric Environment. Part A. General Topics* **1992**, *26*, 2647–2659.

[19] Grosjean, D.; Grosjean, E.; Williams, E. L. Atmospheric chemistry of unsaturated alcohols. *Environmental Science & Technology* **1993**, *27*, 2478–2485.

[20] Chen, Y.; Wang, J.; Zhao, S.; Tong, S.; Ge, M. An experimental kinetic study and products research of the reactions of O3 with a series of unsaturated alcohols. *Atmospheric Environment* **2016**, *145*, 455–467.

[21] Grimme, S. Semiempirical hybrid density functional with perturbative second-order correlation. *The Journal of Chemical Physics* **2006**, *124*, 034108, Publisher: American Institute of Physics.

[22] Grimme, S.; Ehrlich, S.; Goerigk, L. Effect of the damping function in dispersion corrected density functional theory. *Journal of Computational Chemistry* **2011**, *32*, 1456–1465, _eprint: https://onlinelibrary.wiley.com/doi/pdf/10.1002/jcc.21759.

[23] Weigend, F.; Ahlrichs, R. Balanced basis sets of split valence, triple zeta valence and quadruple zeta valence quality for H to Rn: Design and assessment of accuracy. *Physical Chemistry Chemical Physics* **2005**, *7*, 3297–3305, Publisher: The Royal Society of Chemistry.

[24] Frisch, M. J. et al. Gaussian '16 Revision B.01. 2016.

[25] Raghavachari, K.; Trucks, G. W.; Pople, J. A.; Head-Gordon, M. A fifth-order perturbation comparison of electron correlation theories. *Chemical Physics Letters* **1989**, *157*, 479–483.

[26] Klippenstein, S. J.; Harding, L. B.; Ruscic, B. Ab Initio Computations and Active Thermochemical Tables Hand in Hand: Heats of Formation of Core Combustion Species. *The Journal of Physical Chemistry A* **2017**, *121*, 6580–6602, Publisher: American Chemical Society.

[27] Valeev, E. F.; Daniel Crawford, T. Simple coupled-cluster singles and doubles method with perturbative inclusion of triples and explicitly correlated geminals: The CCSD(T)R12^{-} model. *The Journal of Chemical Physics* **2008**, *128*, 244113, Publisher: American Institute of Physics.

[28] Peterson, K. A.; Adler, T. B.; Werner, H.-J. Systematically convergent basis sets for explicitly correlated wavefunctions: The atoms H, He, B–Ne, and Al–Ar. *The Journal of Chemical Physics* **2008**, *128*, 084102, Publisher: American Institute of Physics.

[29] Yousaf, K. E.; Peterson, K. A. Optimized auxiliary basis sets for explicitly correlated methods. *The Journal of Chemical Physics* **2008**, *129*, 184108, Publisher: American Institute of Physics.

[30] Neese, F. Software update: the ORCA program system, version 4.0. *WIREs Computational Molecular Science* **2018**, *8*, e1327, _eprint: https://onlinelibrary.wiley.com/doi/pdf/10.1002/wcms.1327.

[31] Neese, F. Software update: The ORCA program system—Version 5.0. *WIREs Computational Molecular Science* **2022**, *12*, e1606, _eprint: https://onlinelibrary.wiley.com/doi/pdf/10.1002/wcms.1606.

[32] Nguyen, T. L.; Stanton, J. F.; Barker, J. R. A practical implementation of semi-classical transition state theory for polyatomics. *Chemical Physics Letters* **2010**, *499*, 9–15.

[33] Marcus, R. A. Unimolecular Dissociations and Free Radical Recombination Reactions. *The Journal of Chemical Physics* **1952**, *20*, 359–364.

[34] Marcus, R. A.; Rice, O. K. The Kinetics of the Recombination of Methyl Radicals and Iodine Atoms. *The Journal of Physical Chemistry* **1951**, *55*, 894–908, Publisher: American Chemical Society.

[35] Miller, W. H.; Hernandez, R.; Handy, N. C.; Jayatilaka, D.; Willetts, A. Ab initio calculation of anharmonic constants for a transition state, with application to semiclassical transition state tunneling probabilities. *Chemical Physics Letters* **1990**, *172*, 62–68.

[36] Forst, W. *Unimolecular reactions: a concise introduction*; Cambridge University Press: Cambridge, U.K. ; New York, 2003.

Chapter 5

AB INITIO CALCULATIONS OF THE H + HO_2 REACTION AND ITS KINETIC ISOTOPE EFFECT: IMPACT ON WATER LOSS FROM MARS

5.1 Introduction

Geological evidence, including hydrated minerals and fluvial features, indicate the presence of liquid water (~100–1500 global equivalent layers in meters) on Mars in the late Noachian;[1–8] however, current Mars is cold and dry. While a warmer early Mars is thought to be explained by a thick atmosphere rich in greenhouse gases, the fate of early Martian water is less certain. One mechanism for water loss is given by atmospheric escape. The D:H ratio of the present-day Martian atmosphere (5-10× standard mean ocean water)[9–11] is highly suggestive of such an escape mechanism, which favors the loss of lighter H over heavier D. The mechanism for this atmospheric escape is shown diagramatically in Figure 5.1.

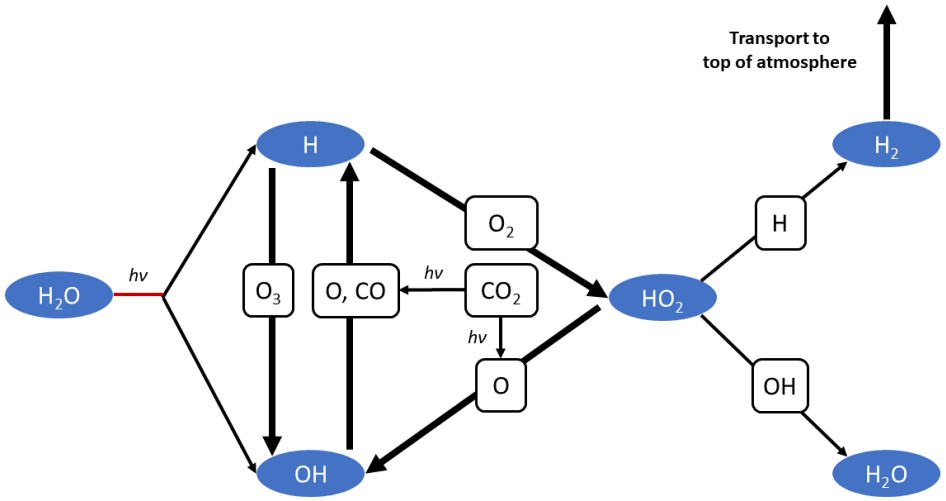

Figure 5.1: Chemical mechanism for water loss from Mars.

Water is photolyzed by incident ultraviolet radiation, producing H and OH, which enter the Martian HO_x cycle. While reaction with various oxygen-containing species allows interconversion between HO_x radicals, the key step for escape is given by the reaction of H and HO_2 to produce H_2. H_2 is relatively inert in the Martian atmosphere, and thus is able to diffuse to the top of the atmosphere and escape. Notably, while this reaction is the only reaction in the Martian atmosphere which produces H_2, the kinetic isotope effect (KIE) for this reaction is entirely unknown, even as it may be the key reaction which controls the D:H ratio of the Martian atmosphere. Furthermore, the temperature dependence of this reaction is uncertain.

Previous experimental studies[12–14] have shown that H + HO_2 has three product channels:

$$H + HO_2 \rightarrow H_2 + O_2 \quad \text{(R1)}$$

$$H + HO_2 \rightarrow OH + OH \quad \text{(R2)}$$

$$H + HO_2 \rightarrow H_2O + O(^1D) \quad \text{(R3)}$$

The main product channel for this reaction is R2, with a branching fraction of ~0.9, while R1 and R3 have branching fractions on the order of ~0.08 and ~0.02, respectively. R1 occurs on the triplet spin surface, while R2 and R3 occur on the singlet surface. The experimental study of these reactions is very difficult. Firstly, it is a radical-radical reaction, which requires that both species must be produced *in situ* and complicates determination of initial conditions. Furthermore, the products of R2 and R3 can react with the initial HO_2 reactants and common reactant precursors such as H_2O_2. Experimental measurement of these rates has been attempted several times, with varying levels of agreement. Uncertainties introduced by *post hoc* corrections for experimental considerations and secondary chemistry have prevented the determination of the reactions' temperature dependence. To the authors' knowledge, no attempt has been made to study the kinetic isotope effect in any of these reactions. When considering isotopically-substituted species, there can also be exchange reactions of the type:

$$H + DO_2 \rightarrow D + HO_2 \quad \text{(R4)}$$

$$D + HO_2 \rightarrow H + DO_2 \quad \text{(R5)}$$

Under realistic experimental conditions, there can also be exchange reactions in the secondary chemistry such as OD + H_2O → HOD + OH, further complicating analysis.

Given the experimental difficulties in measuring this reaction, in this work we leveraged the tools of quantum chemistry to calculate T- and isotope-dependent rate constants for R1–R5 for the first time. We also have incorporated these new rate constants into a 1D photochemical model of the Martian atmosphere[15,16] to assess the impact on isotope-dependent atmospheric water loss.

5.2 Theoretical Methods

Triplet Surface

Reactants, products, and transition states for the triplet surface were all optimized using frozen-core CCSD(T) and the NASA Ames ANO basis set[17] as implemented in the CFOUR package.[18] All open-shell species used unrestricted Hartree-Fock as the self-consistent field reference. The NASA Ames ANO basis set is a contracted quadruple-zeta basis set with a large number of primitives that has been shown to accurately reproduce harmonic vibrational frequencies.[19] Energies at these stationary points were refined using a modified HEAT-345Q scheme[20–23] neglecting spin-orbit effects and replacing the original zero point vibrational energy term with the zero-point vibrational energy from second-order vibrational perturbation theory (VPT2) calculations using the NASA Ames ANO basis set.[17] Thermal rates were calculated using semiclassical transition state theory (SCTST)[24] as implemented in the Multiwell software suite.[25] SCTST allows for the incorporation of multidimensional tunneling, corner-cutting effects, non-classical reflection, and anharmonicity within a single transition state theory framework.[26] In particular, anharmonic effects on the ZPVE and tunneling are expected to be important for describing the difference in rate upon deuteration, making SCTST especially appropriate.

Singlet Surface

Well Energies

Geometries and energies for all stationary points on the singlet surface were obtained at the frozen-core CCSD(T)/NASA Ames ANO level. Zero-point energy corrections were made in the harmonic approximation. One exception is made for the H_2O + $O(^1D)$ well, where the energy for H_2O + $O(^3P)$ is calculated as above and combined with the energy difference between $O(^1D)$ and $O(^3P)$ from the Active Thermochemical Tables (ATcT).[27–29]

VaReCoF

Harmonic oscillators are poor models for the transitional modes of loose transition states found in dissociation, especially as such modes more closely resemble their translational and rotational character in the dissociated limit. To this end, we employed variable reaction coordinate variational transition state theory (VRC-VTST)[30–32] to variationally minimize the sum of states (SOS) of the transitional modes (and thus reactive flux) in an (*E,J*)-resolved fashion, as implemented in

VaReCoF.[33,34] We obtained E-resolved sums-of-states for further master equation treatment using the "E,J model".[35] The fragment geometries and sampled energies were calculated using second order n-electron valence perturbation theory (NEVPT2)[36,37] with the def2-TZVPP basis set[38] as implemented in the ORCA package (version 4.2.1).[39,40] A custom shim was written for this work to allow for the interoperation of VaReCoF and ORCA using the existing Gaussian interface. A (2,2) active space was used for both the H + HO_2 association and OH + OH dissociation, while a (4,3) active space comprising the three *2p* orbitals of the O atom averaged over 5 states was used for the H_2O + O(^{1}D) dissociation channel. Additionally, while both the H + HO_2 and OH + OH channels used the fully internally contracted variant of NEVPT2, the H_2O + O(^{1}D) channel used a quasidegenerate form of NEVPT2 in the Van Vleck formalism,[37] which is only implemented in ORCA for the strongly-contracted variant of NEVPT2.

5.3 Results

Triplet surface

The results of the SCTST calculations are shown in Figure 5.2. The calculated rate at 300K of 4.8×10^{-12} agrees with the temperature-independent recommendation from the JPL Kinetic Data Evaluation[52] within the 95% confidence interval of $3.52 \times 10^{-12} - 1.35 \times 10^{-11}$; however, unlike the JPL recommendation, the current results suggest a significant temperature effect, predicting a 3.4× slower rate at 150K than at 300K. In addition to the temperature dependence, a significant isotope effect is observed. D + HO_2 is calculated to be 1.53× faster than the unsubstituted reaction at 300K, which increases to a factor of 3.43× faster at 150K. Conversely, H + DO_2 is 6.5× slower than the unsubstituted reaction at 300K, slowing precipitously with decreasing temperature to 32.7× slower at 150K. These predictions can be justified in terms of introductory physical chemistry concepts, as displayed in Figure 5.3. For all three reactions, the electronic energies and stationary point geometries are the same. The only difference between isotopically substituted species enters through the nuclear kinetic energy, *e.g.* the zero-point vibrational energy (ZPVE). In D+HO_2, D substitution has no effect on the reactant ZPVE, as the D atom has no vibrations. The minor difference observed comes purely from the diagonal Born-Oppenheimer correction, which while small in magnitude, is included for quantitative accuracy. In contrast, the ZPVE in the transition state is decreased by D substitution. This leads to a net decrease in barrier height and an overall faster reaction. For H + DO_2, both the reactant and transition state ZPVE are decreased by D substitution; however,

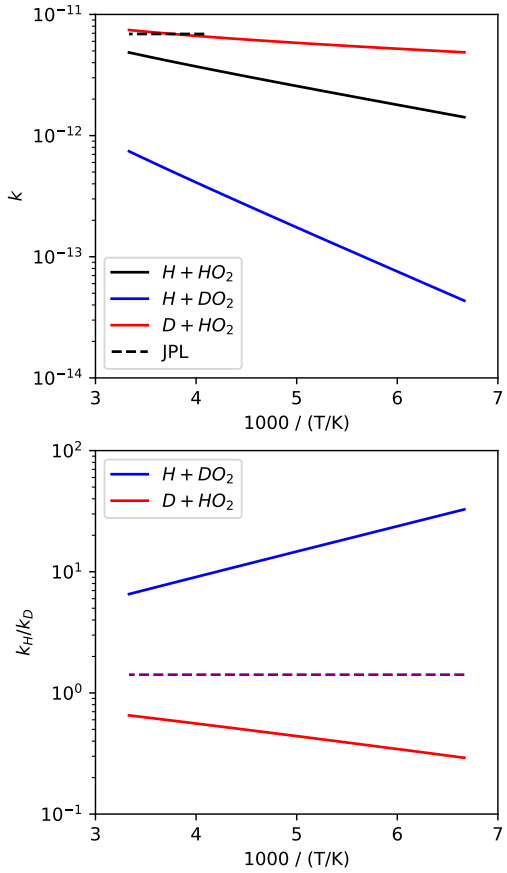

Figure 5.2: Isotope specific rates as a function of temperature for the H + HO_2 reaction on the triplet surface. (Top) The rate for the unsubstituted reaction on the triplet surface is plotted as black solid line, while the rates for the atomically substituted and molecularly substituted reactions are plotted as red and blue solid lines, respectively. The temperature-independent JPL recommendation is shown as the dashed black line for reference. (Bottom) Kinetic isotope effect for the atomically substituted (red) and molecularly substituted (blue) reactions. The purple dashed line shows the constant $\sqrt{2}$ KIE used in many previous models.

this effect is stronger in the reactant than the transition state, as the greatest isotopic contribution to the ZPVE, the D-O bond stretch, is not present in the transition state.

Singlet surface

The stationary points involved in the OH- and H_2O-producing reactive channels are shown in the potential energy diagram in Figure 5.4.

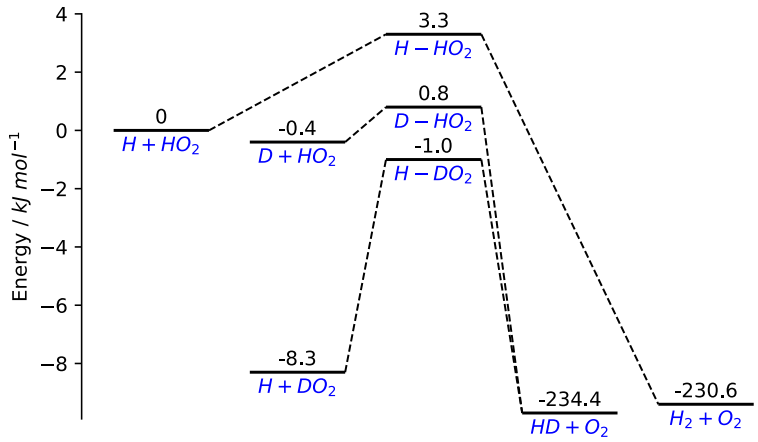

Figure 5.3: Potential energy diagram for various isotopologues of H + HO_2. Differences in the zero of energy for reactants stem from differences in zero-point vibrational energy and the diagonal Born-Oppenheimer correction.

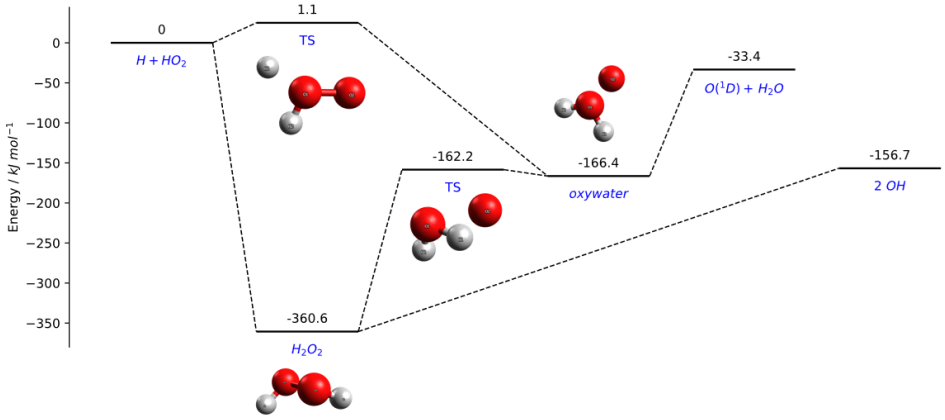

Figure 5.4: Potential energy diagram showing stationary points on the singlet surface in the H + HO_2 reaction.

OH channel

The VRC-VTST results for the singlet product channels are shown in Figure 5.5. The calculated rate at 300 K for the OH channel of 7.125×10^{-11} agrees very well with the temperature-independent JPL recommendation of 7.2×10^{-11}. The calculated rates for all isotopes are minimally dependent on temperature, as would be expected for a barrierless bimolecular reaction with no tight transition states

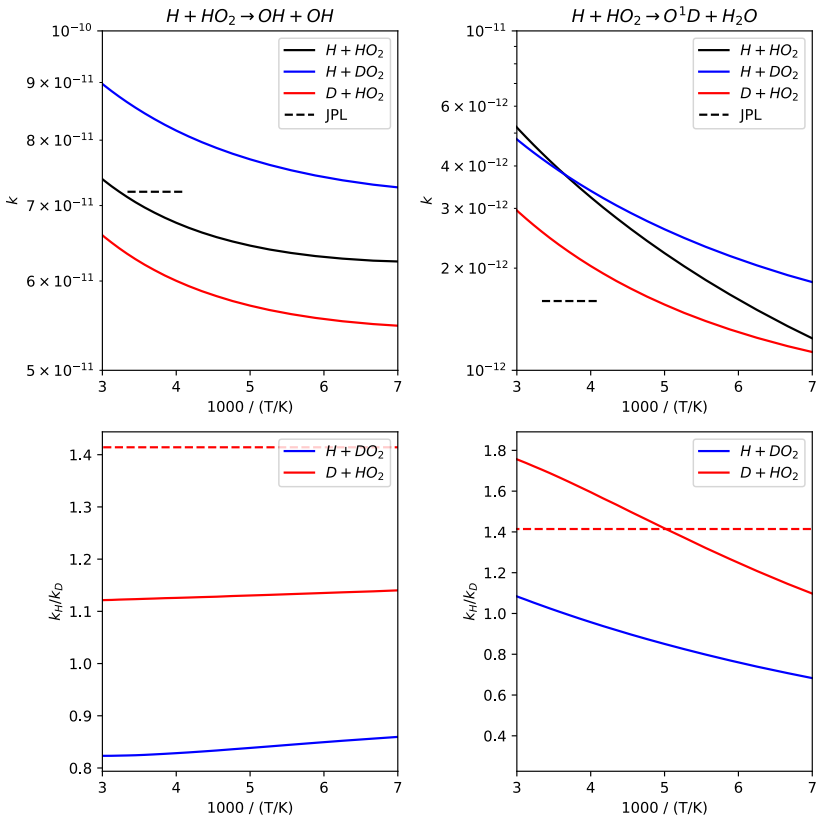

Figure 5.5: Isotope specific rates as a function of temperature for the H + HO_2 reaction on the singlet surface.

separating reactants and products.

H_2O channel

The H_2O-forming channel proceeds through the oxywater intermediate pictured in Figure 5.4. Oxywater can either be formed directly through a tight transition state or via isomerization from the H_2O_2 well; however, the reverse isomerization process (*i.e.* oxywater to H_2O_2) is much faster, generally representing a decrease in the total amount of H_2O formed. H_2O_2 and oxywater are both enantiomeric species that can easily interconvert handedness through internal motion, via O−O rotation for H_2O_2 and an umbrella-like inversion motion for oxywater. The isomerization transition state is most easily understood by inspection of HOOD. In the case of HOOD → oxywater, there are two distinct isomerization channels involving the cleavage of the OH and OD bonds. Each of these channels has two enantiomeric transition states, for a total of four transition states connecting the HOOD and oxywater wells.

Table 5.1: Fit of theoretical rates to Equation 5.1.

Reaction	A	B/K	n
$H + HO_2 \rightarrow H_2 + O_2$	1.216×10^{-11}	-275.987	0.438
$H + DO_2 \rightarrow HD + O_2$	8.413×10^{-12}	-728.650	0.574
$D + HO_2 \rightarrow HD + O_2$	7.636×10^{-12}	-8.308	0.566
$H + HO_2 \rightarrow OH + OH$	5.366×10^{-11}	84.812	0.593
$H + DO_2 \rightarrow OH + OD$	6.958×10^{-11}	65.146	0.556
$D + HO_2 \rightarrow OH + OD$	4.859×10^{-11}	79.814	0.589
$H + HO_2 \rightarrow H_2O + O(^1D)$	4.893×10^{-12}	-33.169	1.545
$H + DO_2 \rightarrow HOD + O(^1D)$	3.470×10^{-12}	58.265	1.427
$D + HO_2 \rightarrow HOD + O(^1D)$	1.590×10^{-12}	143.570	3.538
$H + DO_2 \rightarrow D + HO_2$	2.661×10^{-15}	3.528	-106.702
$D + HO_2 \rightarrow H + DO_2$	1.445×10^{-15}	3.538	-106.700

Care must be taken in correct counting of the appropriate number of reaction paths, as naïve application of rotationally-distinguishable structures paired with rotational symmetry numbers yields isomerization fluxes that are too small by a factor of 2 for HOOH.

Mars Modeling

The isotope- and T-dependent rates were fit to an empirical expression given by Equation 5.1 for use in KINETICS, a 1-D photochemical model of the Martian atmosphere.[15,16] The fitted parameters are reproduced in Table 5.1.

$$k(T) = A \times (T/300K)^n \times e^{B/T} \tag{5.1}$$

KINETICS was also updated for this work to incorporate existing literature KIEs, which served as the base model against which changes in the rates for $H + HO_2$ were evaluated. Initial modeling suggests a ~30% increase in the amount of atomic D at the top of the atmosphere compared to a model without the new T- and isotope-dependent rates of this work. Further modeling will help to assess the overall impact of these new rates.

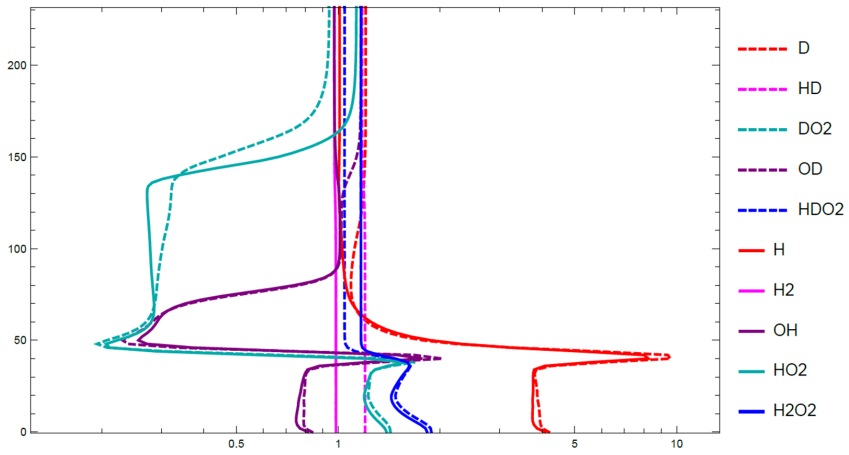

Figure 5.6: Initial results from the new rates of this work. The ratio of new model concentration divided by old model concentration is given on the x axis, and the altitude is given on the y axis. An ~30% increase in atomic D is observed at the top of the atmosphere.

References

[1] Baker, V. R. Geomorphological Evidence for Water on Mars. *Elements* **2006**, *2*, 139–143.

[2] Bibring, J.-P. et al. Global Mineralogical and Aqueous Mars History Derived from OMEGA/Mars Express Data. *Science* **2006**, *312*, 400–404.

[3] Carr, M. H. Oceans on Mars: An assessment of the observational evidence and possible fate. *Journal of Geophysical Research* **2003**, *108*, 5042.

[4] Di Achille, G.; Hynek, B. M. Ancient ocean on Mars supported by global distribution of deltas and valleys. *Nature Geoscience* **2010**, *3*, 459–463.

[5] Grotzinger, J. P. et al. Deposition, exhumation, and paleoclimate of an ancient lake deposit, Gale crater, Mars. *Science* **2015**, *350*, aac7575–aac7575.

[6] McEwen, A. S. et al. The High Resolution Imaging Science Experiment (HiRISE) during MRO's Primary Science Phase (PSP). *Icarus* **2010**, *205*, 2–37.

[7] Orofino, V.; Alemanno, G.; Di Achille, G.; Mancarella, F. Estimate of the water flow duration in large Martian fluvial systems. *Planetary and Space Science* **2018**, *163*, 83–96.

[8] Ramirez, R. M.; Craddock, R. A. The geological and climatological case for a warmer and wetter early Mars. *Nature Geoscience* **2018**, *11*, 230–237.

[9] Donahue, T. M. Evolution of water reservoirs on Mars from D/H ratios in the atmosphere and crust. *Nature* **1995**, *374*, 432–434, number: 6521 publisher: Nature Publishing Group.

[10] Villanueva, G. L.; Mumma, M. J.; Novak, R. E.; Kaufl, H. U.; Hartogh, P.; Encrenaz, T.; Tokunaga, A.; Khayat, A.; Smith, M. D. Strong water isotopic anomalies in the martian atmosphere: Probing current and ancient reservoirs. *Science* **2015**, *348*, 218–221.

[11] Webster, C. R.; Mahaffy, P. R.; Flesch, G. J.; Niles, P. B.; Jones, J. H.; Leshin, L. A.; Atreya, S. K.; Stern, J. C.; Christensen, L. E.; Owen, T.; Franz, H.; Pepin, R. O.; Steele, A.; Team, t. M. S. Isotope Ratios of H, C, and O in CO2 and H2O of the Martian Atmosphere. *Science* **2013**, *341*, 260–263, publisher: American Association for the Advancement of Science section: Report PMID: 23869013.

[12] Keyser, L. F. Absolute rate constant and branching fractions for the atomic hydrogen + hydroperoxyl radical reaction from 245 to 300 K. *The Journal of Physical Chemistry* **1986**, *90*, 2994–3003.

[13] Sridharan, U. C.; Qiu, L. X.; Kaufman, F. Kinetics and product channels of the reactions of perhydroxyl with oxygen and hydrogen atoms at 296 K. *The Journal of Physical Chemistry* **1982**, *86*, 4569–4574.

[14] Thrush, B. A.; Wilkinson, J. P. T. The rate of the reaction between H and HO2. *Chemical Physics Letters* **1981**, *84*, 17–19.

[15] Allen, M.; Yung, Y. L.; Waters, J. W. Vertical transport and photochemistry in the terrestrial mesosphere and lower thermosphere (50–120 km). *Journal of Geophysical Research: Space Physics* **1981**, *86*, 3617–3627.

[16] Nair, H.; Allen, M.; Anbar, A. D.; Yung, Y. L.; Clancy, R. T. A Photochemical Model of the Martian Atmosphere. *Icarus* **1994**, *111*, 124–150.

[17] Almlöf, J.; Taylor, P. R. General contraction of Gaussian basis sets. I. Atomic natural orbitals for first- and second-row atoms. *The Journal of Chemical Physics* **1987**, *86*, 4070–4077.

[18] Matthews, D. A.; Cheng, L.; Harding, M. E.; Lipparini, F.; Stopkowicz, S.; Jagau, T.-C.; Szalay, P. G.; Gauss, J.; Stanton, J. F. Coupled-cluster techniques for computational chemistry: The CFOUR program package. *The Journal of Chemical Physics* **2020**, *152*, 214108, Publisher: American Institute of Physics.

[19] McCaslin, L.; Stanton, J. Calculation of fundamental frequencies for small polyatomic molecules: a comparison between correlation consistent and atomic natural orbital basis sets. *Molecular Physics* **2013**, *111*, 1492–1496.

[20] Tajti, A.; Szalay, P. G. Analytic evaluation of the nonadiabatic coupling vector between excited states using equation-of-motion coupled-cluster theory. *The Journal of Chemical Physics* **2009**, *131*, 124104, Publisher: American Institute of Physics.

[21] Bomble, Y. J.; Vázquez, J.; Kállay, M.; Michauk, C.; Szalay, P. G.; Császár, A. G.; Gauss, J.; Stanton, J. F. High-accuracy extrapolated ab initio thermochemistry. II. Minor improvements to the protocol and a vital simplification. *The Journal of Chemical Physics* **2006**, *125*, 064108, Publisher: American Institute of Physics.

[22] Harding, M. E.; Vázquez, J.; Ruscic, B.; Wilson, A. K.; Gauss, J.; Stanton, J. F. High-accuracy extrapolated ab initio thermochemistry. III. Additional improvements and overview. *The Journal of Chemical Physics* **2008**, *128*, 114111, Publisher: American Institute of Physics.

[23] Thorpe, J. H.; Lopez, C. A.; Nguyen, T. L.; Baraban, J. H.; Bross, D. H.; Ruscic, B.; Stanton, J. F. High-accuracy extrapolated ab initio thermochemistry. IV. A modified recipe for computational efficiency. *The Journal of Chemical Physics* **2019**, *150*, 224102.

[24] Miller, W. H.; Hernandez, R.; Handy, N. C.; Jayatilaka, D.; Willetts, A. Ab initio calculation of anharmonic constants for a transition state, with application to semiclassical transition state tunneling probabilities. *Chemical Physics Letters* **1990**, *172*, 62–68.

[25] Nguyen, T. L.; Stanton, J. F.; Barker, J. R. A practical implementation of semiclassical transition state theory for polyatomics. *Chemical Physics Letters* **2010**, *499*, 9–15.

[26] Shan, X.; Burd, T. A. H.; Clary, D. C. New Developments in Semiclassical Transition-State Theory. *The Journal of Physical Chemistry A* **2019**, acs.jpca.9b01987.

[27] Ruscic, B.; Pinzon, R. E.; Morton, M. L.; von Laszevski, G.; Bittner, S. J.; Nijsure, S. G.; Amin, K. A.; Minkoff, M.; Wagner, A. F. Introduction to Active Thermochemical Tables: Several "Key" Enthalpies of Formation Revisited. *The Journal of Physical Chemistry A* **2004**, *108*, 9979–9997, Publisher: American Chemical Society.

[28] Ruscic, B.; Pinzon, R. E.; Laszewski, G. v.; Kodeboyina, D.; Burcat, A.; Leahy, D.; Montoy, D.; Wagner, A. F. Active Thermochemical Tables: thermochemistry for the 21st century. *Journal of Physics: Conference Series* **2005**, *16*, 561.

[29] Ruscic, B.; Bross, D. H. Active Thermochemical Tables. 2020; `ATcT.anl.gov`.

[30] Klippenstein, S. J. Variational optimizations in the Rice–Ramsperger–Kassel–Marcus theory calculations for unimolecular dissociations with no reverse barrier. *The Journal of Chemical Physics* **1992**, *96*, 367–371.

[31] Georgievskii, Y.; Klippenstein, S. J. Variable reaction coordinate transition state theory: Analytic results and application to the C2H3+H→C2H4 reaction. *The Journal of Chemical Physics* **2003**, *118*, 5442–5455.

[32] Georgievskii, Y.; Klippenstein, S. J. Transition State Theory for Multichannel Addition Reactions: Multifaceted Dividing Surfaces. *The Journal of Physical Chemistry A* **2003**, *107*, 9776–9781, Publisher: American Chemical Society.

[33] Georgievskii, Y.; Harding, L. B.; Klippenstein VaReCoF. 2016.

[34] Harding, L. B.; Georgievskii, Y.; Klippenstein, S. J. Predictive Theory for Hydrogen Atom-Hydrocarbon Radical Association Kinetics. *The Journal of Physical Chemistry A* **2005**, *109*, 4646–4656, Publisher: American Chemical Society.

[35] A. Miller, J.; J. Klippenstein, S. The H+C 2 H 2 (+M)?C 2 H 3 (+M) and H+C 2 H 2 (+M)?C 2 H 5 (+M) reactions: Electronic structure, variational transition-state theory, and solutions to a two-dimensional master equation. *Physical Chemistry Chemical Physics* **2004**, *6*, 1192–1202, Publisher: Royal Society of Chemistry.

[36] Angeli, C.; Cimiraglia, R.; Evangelisti, S.; Leininger, T.; Malrieu, J.-P. Introduction of n-electron valence states for multireference perturbation theory. *The Journal of Chemical Physics* **2001**, *114*, 10252–10264.

[37] Lang, L.; Sivalingam, K.; Neese, F. The combination of multipartitioning of the Hamiltonian with canonical Van Vleck perturbation theory leads to a Hermitian variant of quasidegenerate N-electron valence perturbation theory. *The Journal of Chemical Physics* **2020**, *152*, 014109.

[38] Weigend, F.; Ahlrichs, R. Balanced basis sets of split valence, triple zeta valence and quadruple zeta valence quality for H to Rn: Design and assessment of accuracy. *Physical Chemistry Chemical Physics* **2005**, *7*, 3297–3305, Publisher: The Royal Society of Chemistry.

[39] Neese, F. Software update: the ORCA program system, version 4.0. *WIREs Computational Molecular Science* **2018**, *8*, e1327, _eprint: https://onlinelibrary.wiley.com/doi/pdf/10.1002/wcms.1327.

[40] Neese, F. Software update: The ORCA program system—Version 5.0. *WIREs Computational Molecular Science* **2022**, *12*, e1606, _eprint: https://onlinelibrary.wiley.com/doi/pdf/10.1002/wcms.1606.

Chapter 6

PHOTOELECTRON-PHOTOION COINCIDENCE SPECTROSCOPY OF THE CLO RADICAL

6.1 Introduction

The ClO radical plays a central role in the catalytic destruction of ozone. The catalytic cycle is given by:[1]

$$\mathrm{Cl} + \mathrm{O_3} \rightarrow \mathrm{ClO} + \mathrm{O_2} \quad \text{(R1)}$$

$$\mathrm{ClO} + \mathrm{ClO} + \mathrm{M} \rightarrow \mathrm{ClOOCl} + \mathrm{M} \quad \text{(R2)}$$

$$\mathrm{ClOOCl} \xrightarrow{h\nu} \mathrm{ClOO} + \mathrm{Cl} \quad \text{(R3a)}$$

$$\mathrm{ClOO} \rightarrow \mathrm{Cl} + \mathrm{O_2} \quad \text{(R4)}$$

$$\text{Net reaction} : 2\mathrm{O_3} \rightarrow 3\mathrm{O_2}$$

Key to this process is the photolysis of ClOOCl; however, the photolysis cross section is highly uncertain longwave of 310 nm,[2] due to interference from species such as Cl_2. Furthermore, there remains the question of the branching fraction between photolysis products. Competing with R3a, there is also the possibility of breaking the peroxide bond:[2]

$$\mathrm{ClOOCl} \xrightarrow{h\nu} \mathrm{ClO} + \mathrm{ClO} \quad \text{(R3b)}$$

The product of the photolysis cross section and the quantum yield can be directly measured, interference-free using multiplexed photoionization mass spectrometry (MPIMS);[3,4] however, such experiments require *photoionization* cross sections to determine even relative species concentrations from raw ion count signals. Previous work in our group[5] has moved closer to this goal by measuring the photoionization cross sections of ClO and ClOOCl at the Advanced Light Source (ALS) with the MPIMS apparatus.

Measurement of photoionization cross sections is notoriously difficult, and previous measurements for OH with MPIMS at the ALS[6] and DELICIOUS III (a double-imaging photoelectron-photoion coincidence spectrometer) at the SOLEIL synchrotron in France[7] yielded results that differed by a factor of 1.8× (2.6σ using the errors from Dodson *et al.*) at 13.436 eV, with the SOLEIL result being the larger of the two. Such a discrepancy motivates an additional measurement of the ClO and ClOOCl photoionization cross sections using DELICIOUS III. This work focuses only on the ClO radical, as DELICIOUS III is not well equipped to measure ClOOCl in its current configuration.

ClO is also of interest from the standpoint of fundamental chemical physics. Our initial measurements at the ALS revealed significant structure in the photoionization

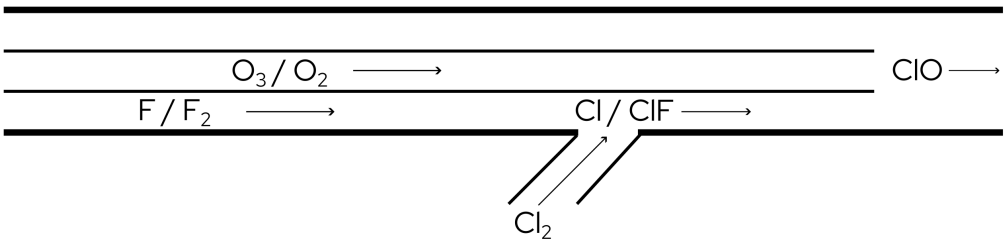

Figure 6.1: Diagram of the radical source.

spectrum, indicative of autoionization resonances. These autoionization resonances arise from the coupling of Rydberg states lying above the adiabatic ionization threshold (analogous to excited vibrational and electronic states of the cation) to the ionization continuum. Neutral ClO has two thermally accessible spin-orbit states, and the ClO^+ cation is isoelectronic to O_2 with two analogous low-lying singlet states, leading to a richness of possibilities for autoionization resonances.

6.2 Experimental

The details of DELICIOUS III have been described in detail elsewhere,[8] but a brief description of the spectrometer and radical source interface used in this work is given below.

Radical Source

ClO was produced using a moveable injector mechanism comprising two concentric flow tubes, as outlined in Figure 6.1. The inner tube contained a flow of ~7-8% O_3 in O_2 generated by an ozonizer. O_3 concentrations were monitored upstream with a Hg pen-ray lamp at 254 nm. F atoms from a microwave discharge flowed in the outer tube, mixing with a flow of Cl_2 40 mm upstream of the end of the outer tube. The fast reaction of F with Cl_2 yielded atomic Cl for later reaction with O_3 to yield ClO. While it was assumed that F reacted to completion with Cl_2, experimental results suggest that this may not be the case (*vide infra*). On some experimental trials, CH_3Br was introduced as an additional reference species for comparison to the previous work at the ALS which used CH_3Br as the reference species for determination of the ClO cross section.

Determination of Cross Section

The chemical mechanism to produce ClO is as follows:

$$\mathrm{F_2} \xrightarrow{MW} \mathrm{F + F} \tag{R5}$$

$$\mathrm{F + Cl_2} \rightarrow \mathrm{ClF + Cl} \tag{R6}$$

$$\mathrm{Cl + O_3} \rightarrow \mathrm{ClO + O_2} \tag{R7}$$

Assuming R6 and R7 go to completion, the produced ClO and the lost O_3 are equal:

$$\Delta[\mathrm{ClO}] = -\Delta[\mathrm{O_3}] \tag{6.1}$$

The equation observed ion counts to concentration of a species A is given by

$$S_\mathrm{A}(E,t) = \Lambda(t) \times m_\mathrm{A}^\beta \times \sigma_\mathrm{A}(E) \times [\mathrm{A}], \tag{6.2}$$

where $\Lambda(t)$ is a time-dependent instrumental constant capturing factors such as the instantaneous photon flux, m_A is the mass of A, β is the mass discrimination factor for the conditions (typically between 0.5 and 3.0), and $\sigma_\mathrm{A}(E)$ is the energy-dependent photoionization cross section of A. Taking the ratio of the change in the signals with the microwave discharge on and off yields

$$\begin{aligned} \frac{\Delta S_\mathrm{ClO}(E)}{\Delta S_{\mathrm{O_3}}(E)} &= \left(\frac{m_\mathrm{ClO}}{m_{\mathrm{O_3}}}\right)^\beta \times \frac{\sigma_\mathrm{ClO}(E)}{\sigma_{\mathrm{O_3}}(E)} \times \frac{\Delta[\mathrm{ClO}]}{\Delta[\mathrm{O_3}]} \\ &\approx -\frac{\sigma_\mathrm{ClO}(E)}{\sigma_{\mathrm{O_3}}(E)}, \end{aligned} \tag{6.3}$$

where the time dependence disappears exactly, and the mass-dependent term is close to one for the masses considered (~51/53 and ~48). As the photoionization cross section for O_3 is known,[9] we can use the ratio of the changes in signal with the microwave discharge on and off to determine the photoionization cross section of ClO.

DELICIOUS III

The gas source is skimmed to produce a molecular beam, which is ionized by tunable VUV light coming from the synchrotron. The resulting electron-ion pair are pulled in opposite directions via ion optics. The electron is focused using a standard velocity map imaging (VMI) apparatus, which allows for the determination of the electron's kinetic energy and angular distribution on a position-sensitive detector. The cation is also measured by a modified VMI apparatus, which allows for the

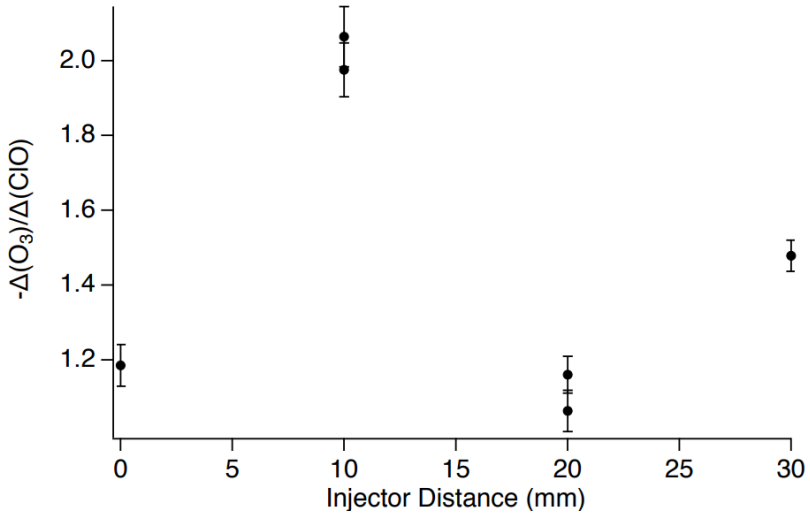

Figure 6.2: Ratio of signal differences as a function of injector distance

simultaneous determination of the ion kinetic energy and mass to charge ratio. The resulting data is a set of electron-cation event pairs corresponding to individual ionization events, which allow for the unambiguous partitioning of energy between the electron and the cation. Subsequent filtering of the data allows for powerful analyses, such as only those electrons associated with a certain mass, or only ions corresponding to electrons with a given kinetic energy range.

6.3 Results

Cross Section

The ratio of the changes in signal were measured as a function of the distance between the end of the injector and the expansion region at 13.0 eV, as shown in Figure 6.2. While the ratio of the signal differences seemed to be reproducible when resetting the injector to the same distance, there seemed to be no simple trend of the ratio of the signal differences with injector distance. This is inconsistent with what would be expected for incomplete reaction of F with Cl_2, where we would expect a steadily increasing $\Delta O_3/\Delta ClO$ with increasing injector distance (decreased F + Cl_2 reaction time) due to O_3 depletion from F + O_3. The reproducibility does, however, indicate that there may be more complex secondary chemistry that is not captured by the above mechanism. If we treat the error as unstructured and take a simple average, we get a $\Delta O_3/\Delta ClO$ of ~1.5, which combined with an O_3 cross section of 10.04 Mb at 13.0 eV,[9] yields a estimate of the ClO cross section of 6.7 ± 2.0 Mb.

The energy dependence of the cross section was determined by scaling the spectrum

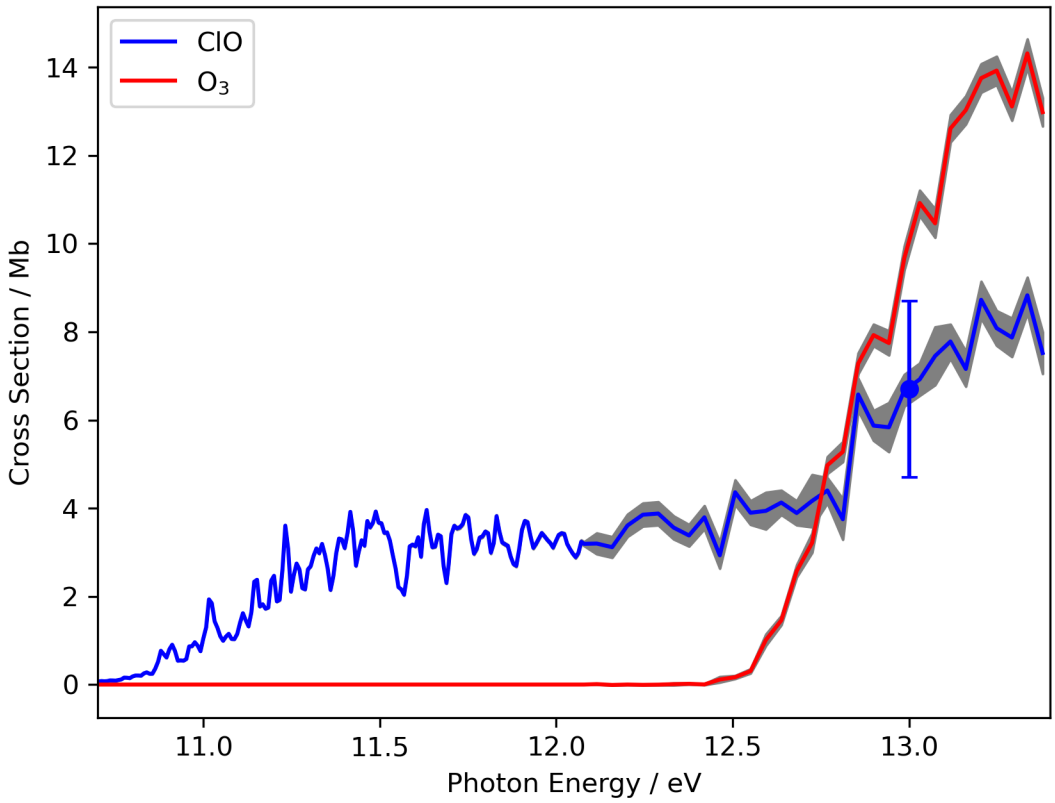

Figure 6.3: Absolute photoionization cross section of ClO measured at SOLEIL. (*Blue*) Cross section of ClO. (*Red*) Cross section of O_3. Grey shading for both lines indicates random error from ion counting. The spectrum was scaled to the absolute cross section measurement at 13.0 eV (*blue point*) with a value of 6.7 ± 2.0 Mb.

to match at 13.0 eV, which is plotted in Figure 6.3. The results are a combination of two scans, scaled to match over a small region near 12.2 eV. The higher energy scan above ~12.2 eV was taken in coarser steps with significantly less averaging, leading to a higher random error from ion counting, as evidenced by the wider error shading. Systematic errors from the single point cross section dominate over the estimated random error from the scan.

The newly measured spectrum is compared to the previous spectrum measured at the ALS in Figure 6.4. The position and relative intensity of the observed features agree well, with differences likely attributable to differences in resolution and step size. Unfortunately, there is still a discrepancy in the absolute value of the photoionization cross section, with the ALS values being ~8× larger than the

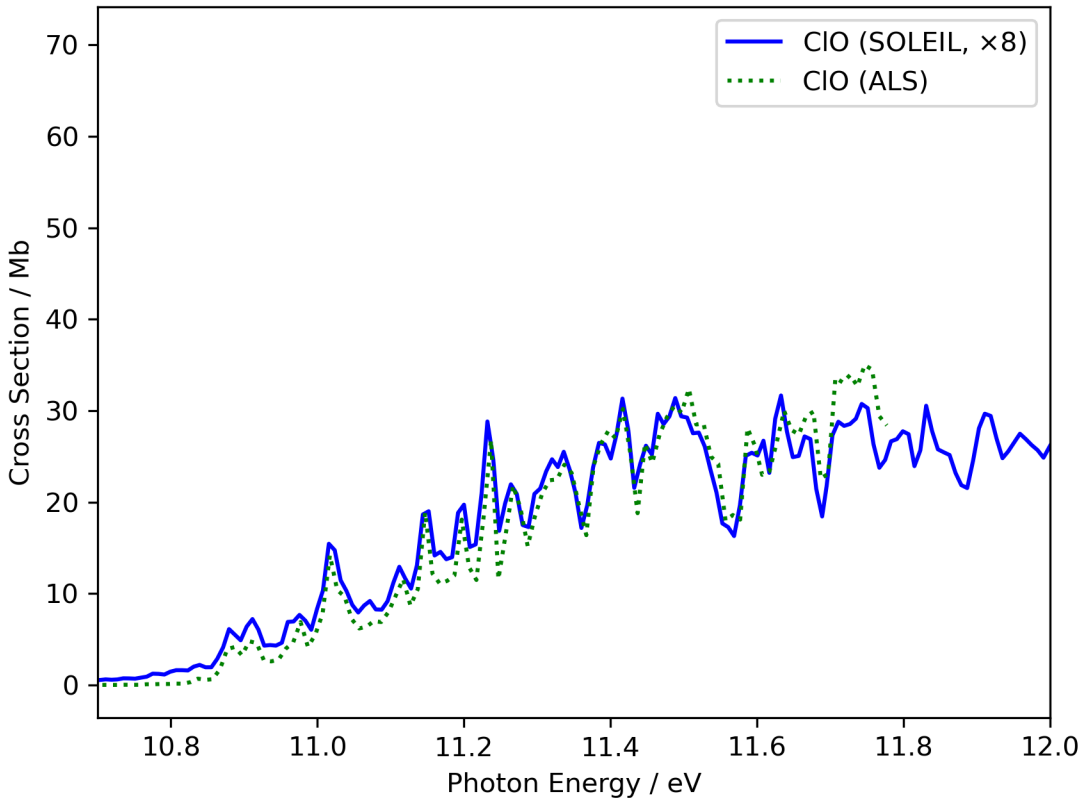

Figure 6.4: Comparison to previous data measured at ALS. (*Blue, solid*) The cross section measured at SOLEIL, scaled by a factor of 8. (*Green, dotted*) The cross section measured at the ALS.

SOLEIL values. Examining Equation 6.3, it becomes clear that an increased ΔS_{O_3} due to the reaction of F + O_3 leads to an underestimation of σ_{ClO}, consistent with the smaller cross section measured at SOLEIL. A factor of 8 does seem extreme, however, considering the range of measured signal difference ratios in Figure 6.2. This may indicate either complex secondary chemistry, which would seem unlikely given the simplicity of the reaction system, or some systematic error that is currently uncharacterized.

Slow Photoelectron Spectrum

The slow photoelectron spectrum (SPES) is shown in Figure 6.5. The first major peak is located at 10.879 eV, corresponding to the adiabatic ionization energy. This is in good agreement with previously published photoionization measurements yielding

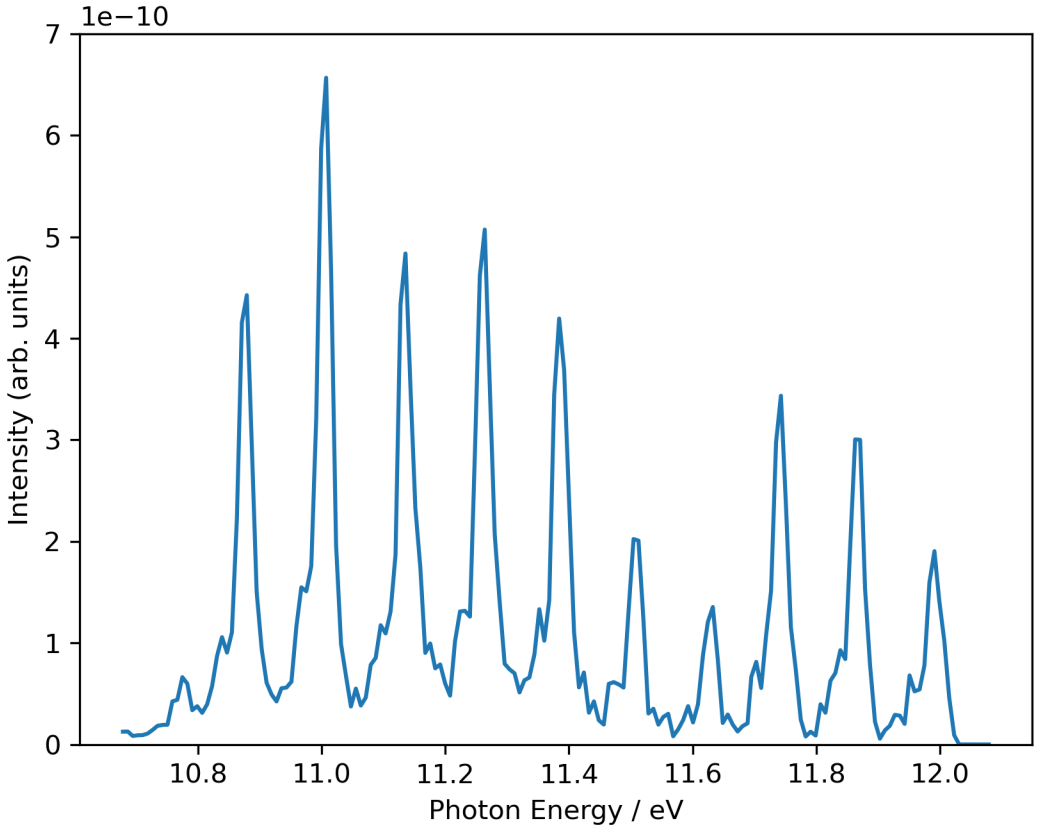

Figure 6.5: Slow photoelectron spectrum of ClO.

10.885 ± 0.016. The features to the left of every major peak are assigned to spin-orbit hot bands. The first such feature appears at 10.839 eV, corresponding to a spacing of 324 cm^{-1}, in good agreement with the known spin-orbit splitting of 313 cm^{-1}.[10] The small peak at 10.879 eV is assigned to a vibrational hot band, corresponding to a ground state vibrational frequency of 841 cm^{-1}, in good agreement with matrix IR studies yielding 854 cm^{-1}.[11] The increase in intensity at 11.743 eV contrary to what might be expected for a Franck-Condon progression might be indicative of a new final electronic state (either the $^1\Delta$ or the $^1\Sigma$ states), but a simple analysis of the SPES is not enough to distinguish this. Future analyses using the photoelectron angular momentum would likely be able to make a positive assignment.

References

[1] Seinfeld, J. H.; Pandis, S. N. *Atmospheric chemistry and physics: from air pollution to climate change*, 2nd ed.; J. Wiley: Hoboken, N.J, 2006; OCLC: ocm62493628.

[2] Burkholder, J. B.; Sander, S. P.; Abbatt, J. P. D.; Barker, J. R.; Cappa, C.; Crounse, J. D.; Dibble, T. S.; Huie, R. E.; Kolb, C. E.; Kurylo, M. J.; Orkin, V. L.; Percival, C. J.; Wilmouth, D. M.; Wine, P. H. Chemical Kinetics and Photochemical Data for Use in Atmospheric Studies, Evaluation No. 19. 2020; `http://jpldataeval.jpl.nasa.gov`.

[3] Osborn, D. L.; Zou, P.; Johnsen, H.; Hayden, C. C.; Taatjes, C. A.; Knyazev, V. D.; North, S. W.; Peterka, D. S.; Ahmed, M.; Leone, S. R. The multiplexed chemical kinetic photoionization mass spectrometer: A new approach to isomer-resolved chemical kinetics. *Review of Scientific Instruments* **2008**, *79*, 104103.

[4] Taatjes, C. A.; Hansen, N.; Osborn, D. L.; Kohse-Höinghaus, K.; Cool, T. A.; Westmoreland, P. R. "Imaging" combustion chemistry via multiplexed synchrotron-photoionization mass spectrometry. *Physical Chemistry Chemical Physics* **2008**, *10*, 20–34.

[5] Smarte, M. D. Kinetic and Spectroscopic Studies of Atmospheric Intermediates. Ph.D. thesis, California Institute of Technology, Pasadena, California, USA, 2019.

[6] Dodson, L. G.; Savee, J. D.; Gozem, S.; Shen, L.; Krylov, A. I.; Taatjes, C. A.; Osborn, D. L.; Okumura, M. Vacuum ultraviolet photoionization cross section of the hydroxyl radical. *The Journal of Chemical Physics* **2018**, *148*, 184302.

[7] Harper, O. J.; Hassenfratz, M.; Loison, J.-C.; Garcia, G. A.; de Oliveira, N.; Hrodmarsson, H.; Pratt, S. T.; Boyé-Péronne, S.; Gans, B. Quantifying the photoionization cross section of the hydroxyl radical. *The Journal of Chemical Physics* **2019**, *150*, 141103.

[8] Garcia, G. A.; Cunha de Miranda, B. K.; Tia, M.; Daly, S.; Nahon, L. DELICIOUS III: A multipurpose double imaging particle coincidence spectrometer for gas phase vacuum ultraviolet photodynamics studies. *Review of Scientific Instruments* **2013**, *84*, 053112.

[9] Berkowitz, J. Absolute partial photoionization cross sections of ozone. *International Journal of Mass Spectrometry* **2008**, *271*, 8–14.

[10] Basco, N.; Morse, R. D. The vacuum ultraviolet absorption spectrum of ClO. *Journal of Molecular Spectroscopy* **1973**, *45*, 35–45.

[11] Coxon, J. A.; Ramsay, D. A. The A2Πi–X2Πi band system of ClO: Reinvestigation of the absorption spectrum. *Canadian Journal of Physics* **1976**, *54*, 1034–1042, Publisher: NRC Research Press.